Summer 2020

Cosmic Metal Evolution During the First ∼1 Billion Years After the Big Bang Using Damped/Sub-Damped Lyman-Alpha Absorbers

Suraj Poudel

Cosmic Metal Evolution During the First ∼1 Billion Years After the Big Bang Using Damped/Sub-damped Lyman-alpha Absorbers

by

Suraj Poudel

Bachelor of Science
Tribhuvan University, 2007

Master of Science
Tribhuvan University, 2010

Submitted in Partial Fulfillment of the Requirements

for the Degree of Doctor of Philosophy in

Physics

College of Arts and Sciences

University of South Carolina

2020

Accepted by:

Varsha P. Kulkarni, Major Professor

Steven Rodney, Committee Member

Fred Myhrer, Committee Member

Subrahmanyam Bulusu, Committee Member

Cheryl L. Addy, Vice Provost and Dean of the Graduate School

Dedication

This work is dedicated to my grandmother (Hajurama) who always showered me with unconditional love throughout her life. Also, I dedicate this work to my parents (Buwa and Aama). Finally, I can not remain without dedicating this dissertation to my respected teacher and Master's degree thesis advisor, Prof. Dr. Udayraj Khanal, who has always been the source of motivation for doing physics.

Acknowledgments

First of all, I would like to express my gratitude to my advisor, Dr. Varsha P. Kulkarni, for her constant motivation and guidance. This work would not be possible without her help and support. I would also like to thank the members of my dissertation committee, Dr. Steven Rodney, Dr. Fred Myhrer, and Dr. Subrahmanyam Bulusu for their time, interest, and suggestions. I would also like to express my gratitudes to my collaborators, Dr. Céline Péroux, Dr. Brenda Frye, Dr. Debopam Som, Dr. Hadi Rahmani, Dr. Samuel Quiret, Frances H. Cashman, and Sean Morrison. I am grateful to my parents for their patient understanding and persistent support. I am also thankful to National Science Foundation (NSF) and National Aeronautics and Space Administration (NASA) for providing support to this work. I thank Dr. Ryan Cooke for providing his MCMC code for calculating progenitor star parameters from relative element abundances, and Dr. Xiaohui Fan for making his MagE data for one quasar (J0306+1853) available after publication. Finally, I would like to express my gratitude to the staff at the Las Campanas Observatory for helping with the observations.

Abstract

Metal abundance measurements throughout the cosmic ages track the history of galaxy formation and evolution. Measuring abundances during the first ∼1 billion years is especially important, as they are influenced by the nucleosynthetic signatures from the early stars. Evolution of metallicity of Damped/sub-Damped Lyman-alpha Absorbers (DLAs/sub-DLAs) detected in the spectra of quasars is a powerful tracer of the cosmic star formation history. A sudden drop in DLA metallicity at z>4.7 was reported in some recent studies. However, these studies were primarily based on refractory elements such as Fe and Si. We present ten new abundance measurements of the elements O, C and Si at $z > 4.5$, increasing the existing sample of weakly depleted elements in gas-rich galaxies significantly at z∼5. These measurements are based on spectra of quasars with DLAs/sub-DLAs obtained with the MIKE and MagE spectrographs on Magellan Telescope, the X-Shooter spectrograph on the Very Large Telescope, and the ESI on the Keck Telescope. We combine these new measurements with those drawn from the literature to estimate the $N_{H\,I}$-weighted binned mean metallicity of -1.51 ± 0.18 dex at $\langle z \rangle$ =4.8. This metallicity value is in excellent agreement with the prediction from lower redshift DLAs, suggesting that the metallicity evolution is smooth at $z \sim 5$, rather than showing a sudden decline at $z > 4.5$. Furthermore, the metallicity evolution trends for the DLAs and sub-DLAs are similar within our uncertainties. We also determine the extent of dust depletion using a combination of both the volatile element O and the refractory elements Si and/or Fe. Some of the absorbers show evidence of depletion of elements on dust grains. The relative abundances of these absorbers along with other z∼5 absorbers

from the literature show some peculiarities, e.g. low [C/O] in several absorbers and high [Si/O] in some absorbers. Additionally, using [C/O] and [Si/O] to constrain the nucleosynthesis models, we estimate that the probability distributions of the progenitor star masses for three relatively metal-poor DLAs are centered around 12 $M_{\odot}$ to 17 $M_{\odot}$. Furthermore, the $z \sim 5$ absorbers show a different metallicity-velocity dispersion relation than lower redshift DLAs, suggesting that they may be tracing a different population of galaxies. Finally, we comment on the implications of our studies for galaxy evolution, the need for further expanding the samples of $z \gtrsim 5$ absorbers, and the promise offered by the next generation of large telescopes.

Table of Contents

List of Tables

List of Figures

Chapter 1

Introduction

Understanding the nature of cosmic chemical evolution during the first $\sim$ 1 billion years after the big bang is crucial to unfold the mystery behind how the present day large structures got into existence from the featureless dark ages. Especially important is the role of the early stars (metal-free population III stars and metal-poor population II stars) in the formation of subsequent enriched galaxies with heavy elements. While the big bang nucleosynthesis had produced only few isotopes of hydrogen, helium, and a very small amount of lithium, other elements were later created by stellar nucleosynthesis in evolving and exploding stars. Despite the lack of observational evidences of early stars and galaxies, several theoretical ideas have been developed over the decades. However, severals questions about the nature and roles of these early stars in the formation and evolution of galaxies are still not clear. The most common questions are: the epoch at which the very first stars and galaxies started to form, their initial mass function (IMF), chemical and morphological evolution, star formation rates, their lifetimes, feedbacks, and their role in the reionization of the Universe. As the universe is predominantly hydrogen, the role played by gas in the galaxy formation and evolution is very important. Since the continuous cycle of star formation makes the use of interstellar gas, the study of chemical properties of the interstellar medium (ISM) is very important to understand the galaxy formation and evolution. This chapter summarizes the chemical make up of the ISM, physics behind the interaction of radiation with the interstellar medium, and the observables that are needed to quantify various spectroscopic measurements.

1.1 Structure of the Interstellar Medium

The space between the stars containing gas and dust, out of which a new star gets born, is called ISM. The dynamics of ISM involves gas turbulent motions, galactic magnetic fields, shock waves, supernovae explosions, stellar winds, constant streams of high energy particles such as cosmic rays, and the cosmic microwave background (CMB) photons. Though the main contribution to the chemical makeup of ISM is neutral hydrogen, there also exists dust, molecules, ions, and free electrons. Therefore, ISM is an enormous and very complex environment. To decipher the physics of ISM, solving the equations of magnetohydrodynamics is required that involves understanding of quantum mechanics, thermodynamics, and electrodynamics. Furthermore, to study the production and destruction of dust grains and complex molecules, one need to have a detailed understanding of chemistry.

1.1.1 Gas

The interstellar medium makes up between 10 to 15 percent of the visible mass of the Milky Way. About 99 percent of the material is gas. ISM can be divided into different gas-phase constituents that are in approximate pressure equilibrium. These are described as ionized or neutral, referring to the dominant state of dominant element (see Table. 1.1). Cold neutral medium: Despite occupying a smaller volume fraction, the cold, neutral gas dominates the most of the mass in the universe in the form of clouds. It has a temperature of $\sim$ 100 K and the particle number density of $\sim$ 50 cm^{-3}. This is usually found in the plane of the Milky Way. Warm neutral medium: This phase comprises $\sim$ 50 percent of the volume of the Milky Way and is located mainly in the disc. It has a temperature of $\sim$ 6000 K and the particle number density of $\sim$ 1 cm^{-3}. It is maintained by X-rays and cosmic rays. Warm ionized medium: This phase has varying densities from $\sim$ 0.1 cm^{-3} in diffuse gas to $\sim 10^4$ cm^{-3} in H II regions. This is mainly found in disc and halo of Milky Way and is maintained

by photoionization. Hot ISM: This is extremely hot and diffuse phase of ISM and typically found in halo of Milky Way. It has a temperature of $\sim 10^6$ K and the particle number density of $\sim 10^{-3}$ cm^{-3}. Molecular Clouds: Molecular clouds are colder (temperature of the order of ~ 30 K) and denser regions (density of the order of 10^6 cm^{-3}) in which hydrogen is mostly in molecular form. Besides hydrogen , other molecules are also found and are typically detected in microwave emission. These clouds have large optical depths in the visible and large clouds have mass up to $\sim 10^6 M_\odot$. They are highly dusty with high level of extinction at optical and are considered as the initial phases of star formation.

1.1.2 Dust

The dust is made of thin, highly flattened flakes or needles of graphite (carbonaceous dust) and rock-like minerals (silicate dust) coated with water ice. The size of dust grain is comparable to the wavelength of blue light. Although the dust makes up only about 1 percent of ISM, it has a much greater effect on the formation of molecules and ultimately the stars. The evidence of the existence of dust can be speculated from interstellar absorption, reddening, reflection nebulae, and depletion of elements from gas phase into dust grains etc. Since dust obscures the visible light, we can see out only about few thousands light years in the plane of the Galaxy.

1.1.3 Heating and cooling of ISM

Generally speaking, two types of heating mechanisms are dominant in the diffuse ISM, namely, cloud-cloud collisions and absorption of photons by gas or dust. However, in the molecular clouds, cosmic rays are also a significant heating source. The principle source of heating in the gas phase of ISM is due to the ejection of an electron from a parent atom, ion, or molecule which carries away some part of the photon energy that goes into heating the gas. For a photon of energy, hν, the energy goes into

heating would be hν−IP, where IP is the ionization potential of the parent species. In ionized gas (H II regions), photoionization of hydrogen is the dominant source of heating due to its omnipresence. However, in the regions of ISM where hydrogen is almost neutral, there must be tiny fraction of photons with energies $\geq$ 13.6 eV. As a result only species like neutral carbon with IP <13.6 eV can be photo-ionized in those regions. In fact, the primary heating mechanism in neutral ISM is photo-ejection of electrons from interstellar dust grains.

Besides heating, ISM also goes through cooling process that involves conversion of thermal motion to radiation which then escape from the system. In the cold neutral medium, the electron densities are low and the radiation is mainly due to the collisional excitation of neutral hydrogen atoms in the ground state. As the kinetic temperatures are low, the transitions in the diffuse ISM is by fine-structure interactions which are low energy transitions and emitted photons are typically in the far-IR.

1.1.4 Production of heavier elements

The big bang nucleosynthesis was able to synthesize baryonic matter mostly only in the form of hydrogen and helium. Elements heavier than hydrogen and helium were later synthesized by stars of various masses during different stages of their evolution. Capture of protons and neutrons on light nuclei tend to produce proton- or neutron-rich nuclei respectively. Three basic mechanisms for the production of metals are summarized below.

Fusion reactions in stellar cores

Fusion reactions in the cores of stars are responsible for the formation of lighter elements up to the Fe peak nuclei. As fusion of heavier nuclei need more energy relative to the fusion of lighter nuclei, the elements that can be synthesized in the

stellar core depends on the mass of the stars. For example, during the lifetime of our sun, it will only produce He and C. Solar mass stars don't have enough stellar core temperatures to synthesize higher nuclei than C. Stars with $\sim$10 $M_\odot$ are massive enough to fuse Fe peak elements. As Fe peak nuclei have the highest binding energy per nucleon, the fusion process cannot synthesize nuclei with higher atomic number than the Fe peak nuclei.

S-process

S-process is a process in which new elements grow by capturing neutrons followed by radioactive β decay. It is called s-process or slow process as the rate of neutron capture by the atomic nuclei is slower comparative to the rate of radioactive β decay. It occurs at relatively low neutron density, low neutron flux, and temperature in the order of 10^8 K and requires pre-existing heavy isotopes as seed nuclei. As the neutrons are not affected by the coulomb potential, s-process can produce higher atomic number nuclei up to bismuth which has mass number of 209. An example of s-process is a conversion of ^{109}Ag to ^{122}Sb through multiple neutron captures until it reaches unstable isotope and then beta decays to a stable one. Asymptotic giant branch stars are the home to s-process. The rate of building higher mass number isotopes is however dependent of the ability of a star to produce neutrons and its initial iron abundance.

R-process

Elements heavier than Fe are produced during supernova explosions primarily by rapid capture of neutrons by nuclei and is called as r-process. It occurs mainly in the core collapse supernova. It needs relatively high neutron density (n$> 10^{20}$ cm^{-3}), high neutron flux, and temperature in the order of 10^9 K. The neutron capture rate is higher than the rate of β decay. This process produces almost half of the isotopes

heavier than iron and creates elements even heavier than ^{209} Bi, the heaviest element produced by s-process.

1.1.5 Injection of heavy elements into the ISM

Stellar winds and supernova explosions are two main mechanisms that are responsible for enriching the ISM with heavier elements. Stellar winds developed due to the thermal pulsations during the end of the lives of intermediate mass stars ($\lesssim 10$ $M_\odot$) form the planetary nebulae which eventually diffuse into the ISM. As the progenitors of the planetary nebula are of intermediate mass, these stellar winds enrich the ISM mainly with lighter elements such as He, C, N, and O. Heavier elements are injected into the ISM by supernova explosions. Moreover, different supernova explosions enrich the ISM with different distribution of heavier elements. Type I supernova which have no hydrogen lines in their spectra can be further divided into Type Ia, Type 1b, and Type 1c based on different absorption lines in their spectra. Type 1a supernova are caused by the accretion of material from red giant onto a white dwarf and enrich the ISM mainly with Fe-peak elements such as Cr, Mn, Fe, Co, and zn. Type II along with Types 1b, 1c are also called core collapse supernova and caused by gravitational collapse of massive stars at the end of their lives. Type II supernova enrich the ISM with α-elements such as C, O, Mg, Si, S, Ca, Ar along with the Fe-peak elements.

1.2 Formation of spectral lines

When a beam of radiation traverses through stellar interior, stellar atmosphere, or ISM, energy can be either added through emission or subtracted through absorption. This process is called radiative transfer and is contributed by various physical processes.

1.2.1 Emissivity

The energy generated per unit volume (dV), per unit time (dt), per unit frequency (dν), per unit solid angle (dω) can be written as

$$j_\nu = \frac{dE_\nu}{dV dt d\nu d\omega}[Jm^{-3}s^{-1}Hz^{-1}sr^{-1}]$$

and is called emissivity. The change in specific intensity along the line of sight can then be written in terms of emissivity as

$$dI_\nu^+ = +j_\nu(s)ds$$

where ds is the line element along the line of sight. The phenomenon of decreasing intensity is called extinction and is contributed by either absorption or scattering. While the absorption causes the destruction of the photons, scattering also diminishes the number of photons along the line of sight. The amount of intensity removed from a beam by extinction thus depends on the initial intensity of the beam, number density of absorbing particles, and effective cross-section per particle (σ_ν).

$$dI_\nu^- = -\sigma_\nu n I_\nu ds$$

The quantity $\sigma_\nu n$ is called opacity or attenuation coefficient (α_ν) which signifies the efficiency with which the material absorbs and scatters light contributing to diminish the intensity.

$$\sigma_\nu n = \alpha_\nu$$

1.2.2 Optical depth and column density

The cumulative effect of the opacity integrated along the line of sight over a distance is quantified by the optical depth (τ_ν),

$$\tau_\nu = \int \alpha_\nu ds = \int n(s)\sigma_\nu ds$$

The physical processes which contribute to opacity are either line or continuum processes namely bound-bound absorption, bound-free absorption, free-free absorption, and scattering. A medium is called optically thick at a particular wavelength, λ, if $\tau_\lambda >> 1$.

It is not feasible to measure the true density, $n(s)$ of the absorbing material, however, one can determine the column density given by

$$N = \int n(s) ds$$

which is the number of absorbing particles cm^{-2} along the line of sight. Finally, one can write column density in terms of optical depth and absorption coefficient as

$$\tau_\nu = N\sigma_\nu$$

1.2.3 Equation of radiative transfer

The added and the subtracted intensity can now be combined into a single differential equation called as the radiative transfer equation, the solution of which gives the beam intensity along the path.

$$\frac{dI_\nu}{ds} = j_\nu - \alpha_\nu I_\nu$$

Furthermore, one can define the source function as

$$S_\nu = \frac{j_\nu}{\alpha_\nu}$$

Then, the radiative transfer equation can be further simplified into

$$\frac{dI_\nu}{d\tau_\nu} = S_\nu - I_\nu$$

Assuming a constant source function along the beam, the solution to above differential equation can be written as

$$I_\nu(\tau_\nu) = I_\nu(0)e^{-\tau_\nu} + S_\nu(1 - e^{-\tau_\nu})$$

For pure absorption, the source term goes to zero and the equation reduces to

$$I_\nu(\tau_\nu) = I_\nu(0)e^{-\tau_\nu}$$

and the optical depth can be simplified into

$$\tau_\nu = -ln\frac{I}{I_0}$$

1.3 Line broadening processes

Generally, the bound-bound atomic transitions are the reason for the absorption features observed in the spectra of background quasars and these transitions are supposed to be very sharp and well defined. However, the width of spectral lines are affected by various factors such as temperature, turbulence, and bulk motion in the gas resulting into more complex and broadened line profiles. These processes can be divided into three types: microscopic, macroscopic, and instrumental processes. While the microscopic processes arise on the scale comparable to the photon mean free path, the macroscopic processes operate on length scales greater than the photon mean free path. Instrumental broadening is also played at macroscopic level, however, it is not of any astrophysical origin. The three major line broadening mechanisms are quantum (natural or Lorentz) broadening, thermal (Doppler) broadening, and microturbulent broadening.

1.3.1 Natural line broadening

Uncertainty principle tells that any atomic energy level does not have a well defined energy E_i, but rather a superposition of all the possible states around E_i. When an atom absorbs a photon, it goes to higher energy state which is unstable. If the atom stays in the excited state for a short time (dt), the corresponding uncertainty in the energy (dE) is given by the uncertainty relation, $dE\ dt \gtrsim \frac{h}{2\pi}$. As a result, the absorption of photons does not occur at a unique frequency or wavelength, but

over a range centered at some particular value. If we treat the atomic transition as a classical damped oscillator, then the absorption cross section (σ_ν) that describes the profile of a spectral line centered at a frequency ν_0 is given by

$$\sigma_\nu = \frac{\pi e^2}{m_e c}\phi_\nu$$

where ϕ_ν is a function of frequency and is related to the damping constant of the oscillator (γ) by

$$\phi_\nu = \frac{\gamma/4\pi^2}{(\nu-\nu_0)^2 + (\gamma/4\pi)^2}$$

The above equation represents a line profile with full width at half maximum (FWHM) of $\frac{\gamma}{2\pi}$ and the classical damping constant is given as

$$\gamma = \frac{2e^2}{3m_e c^3}\nu_0^2$$

However, for real absorption lines, we need to consider the quantum harmonic oscillator and replace the classical damping constant, γ by the quantum damping constant Γ, which is the sum of all the transitional probabilities for both the lower and higher energy levels.

$$\Gamma = \Gamma_i + \Gamma_j$$

where,

$$\Gamma_{i,j} = \sum_{l<i,j} A_{i,jl}$$

and the $A_{i,jl}$ are the Einstein coefficients which give the probability of transition from any of the states i and j to the lower state, l. Finally, we can incorporate the transitional probabilities into a parameter called oscillator strength, f and write the absorption cross section as

$$\sigma_\nu = \frac{8\pi e^4}{3m_e^2 c^4} f[\frac{\nu^4}{(\nu^2-\nu_0^2)^2 + (\Gamma/2\pi)^2\nu^2}]$$

As the absorption is pronounced near the resonance frequency, ν_0,

$$(\nu^2-\nu_0^2)^2 = (\nu+\nu_0)^2(\nu-\nu_0)^2 \simeq (2\nu_0)^2(\nu-\nu_0)^2$$

and the absorption cross-section can be expressed as a constant (σ_0) times a frequency dependent function, ϕ_ν, i.e;

$$\sigma_\nu = \sigma_0 \phi_\nu$$

After applying the normalization condition $\int_0^\infty \phi_\nu d\nu = 1$ to get the normalization constant, we obtain the normalized absorption cross-section,

$$\phi_\nu = \frac{\Gamma/4\pi^2}{(\nu - \nu_0)^2 + [\Gamma/4\pi]^2}$$

which is the final Lorentzian profile with the quantum mechanical damping constant, Γ and full width at half maximum, FWHM= $\frac{\Gamma}{2\pi}$.

1.3.2 Thermal line broadening

In astrophysical environments like ISM, gas particles follow a Maxwellian velocity distribution at a given kinetic temperature, T. The line-of-sight component of the velocity distribution is a gaussian function

$$f(v)dv = \sqrt{\frac{m}{2\pi KT}} \exp(-\frac{mv^2}{2KT})dv$$

where the thermal or doppler width is given as $b = \Delta v_{th} = \sqrt{\frac{2KT}{m}}$ in velocity units and $\Delta\nu_{th} = \frac{\nu_0}{c}\sqrt{\frac{2KT}{m}}$ in frequency units. The final absorption profile is given as

$$\phi_\nu = \frac{1}{\sqrt{\pi}} \frac{1}{\Delta\nu_{th}} \exp(-\frac{(\nu - \nu_0)^2}{\Delta\nu_{th}^2})$$

and satisfies the following normalization condition.

$$\int_0^\infty \phi_\nu d\nu = 1$$

Although not well defined physically, turbulent also plays a role in line broadening process. It might include motions within the interstellar cloud (especially in star forming regions or in convective stellar photospheres) and can be taken as a line-of-sight gaussian velocity distribution for the sake of convenience which also appears

consistent with observation. In stellar physics, this usually operates on length scale shorter than the photon mean free path which is called microturbulance. The total doppler broadening is then obtained by simply adding thermal and turbulent widths in quadrature,

$$b_{eff}^2 = b_{turb}^2 + b_{th}^2$$

The peak value at $\nu = \nu_0$, is given by

$$\phi_0 = \frac{1}{\sqrt{\pi}} \frac{1}{\Delta\nu_{th}} = \frac{1}{\sqrt{\pi}} \frac{c}{\nu_0} \frac{1}{b} = \frac{1}{\sqrt{\pi}} \frac{c}{\nu_0} \sqrt{\frac{m}{2KT}}$$

At half maximum,

$$\phi_\nu(1/2) = \frac{1}{2}\phi_0$$

$$(\nu_{1/2} - \nu_0)^2 = \nu_0^2 \frac{2KT}{mc^2} ln2$$

$$FWHM = \Delta\nu_{1/2} = 2\frac{\nu_0}{c}\sqrt{[\frac{2KT}{m} ln2]} = 2\sqrt{ln2}\Delta\nu_{th} = 1.665\Delta\nu_{th}$$

1.3.3 Voigt profile

The combination of thermal broadening with the natural or lorentzian broadening is called the Voigt profile. As the thermal and natural broadenings are two independent processes, the Voigt profile does not have any simple analytic form but is the result of convolution of Lorentz profile with a Doppler profile:

$$\phi_\nu(Voigt) = \phi_\nu(Natural) \bigotimes \phi_\nu(Doppler)$$

The final functional form for the Voigt profile is,

$$\phi_\nu = \frac{\Gamma/4\pi^2}{(\nu - \nu_0)^2 + [\Gamma/4\pi]^2} \frac{1}{\sqrt{\pi}} \frac{1}{\Delta\nu_{th}} \exp\left(-\frac{(\nu - \nu_0)^2}{\Delta\nu_{th}^2}\right)$$

Since the Lorentz profile falls off slower than Doppler profile, core remains roughly Gaussian, while the wings look like a Lorentz profile. Fitting of Voigt profiles is useful for the observations of absorption towards background sources like quasars to measure the temperatures and column densities of the gas along the line of sight.

1.4 The equivalent width and the curve of growth

A fundamental observable of importance is the equivalent width, W_λ which is measured in wavelength units and is defined as the area under a normalized absorption profile. The diffuse interstellar clouds have low temperatures and the lines are too narrow (as the thermal broadening is small) to be resolved by typical spectrographs. The intrinsic spectral-line profiles are thus difficult to study, however, one can still measure the line-strength in terms of equivalent width. If I_c is the continuum intensity and I_λ is the intensity through the line profile, then equivalent width can be expressed as

$$W_\lambda = \int_0^\infty \frac{I_c - I_\lambda}{I_c} d\lambda = \int_0^\infty (1 - e^{-\tau_\lambda}) d\lambda$$

In practice, the upper integration limit is actually truncated at the edges of the line.

1.4.1 Optical depth to column density

More importantly, we are interested in the column densities of different species. One can estimate the column density along the line of sight by knowing the optical depth,

$$\tau_\nu = \int_0^D \sigma_\nu n_i(s) ds$$

where, D is the distance over which the absorption occurs. The absorption cross-section for a line transition from levels i to levels j is,

$$\sigma_\nu(ij) = \frac{c^2}{8\pi\nu^2} \frac{g_j}{g_i} A_{ji} \phi_\nu(s) = \sigma_0 \phi_\nu$$

where g_i and g_j are statistical weights for lower and upper levels, A_{ji} is Einstein coefficient which gives the transition probability, and ϕ_ν(s) is the normalized profile function. A_{ji} and the oscillator strength f_{ij} are related by

$$A_{ji} = \frac{8\pi^2 e^2 \nu^2}{m_e c^3} \frac{g_i}{g_j} f_{ij}$$

and the optical depth (τ_ν) takes the form,

$$\tau_\nu = \frac{\pi e^2}{m_e c} f_{ij} \int_0^D \phi_\nu(s) n_i(s) ds = \frac{\pi e^2}{m_e c} f_{ij} N_i$$

The last term arises for an absorption profile independent of s.

1.4.2 Curve of Growth (COG)

The plot of strength of a line in terms of equivalent width, W_λ vs. a function of column density of the atomic species is called the curve of growth. 1. Linear part of COG: We know from previous section, the equivalent width can be expressed in terms of optical depth.

$$W_\lambda = \lambda_0^2/c \int_0^\infty (1 - \exp(-\tau_\nu) d\nu$$

For weak lines, $\tau_\nu << 1$,

$$W_\lambda \simeq \lambda_0^2/c \int_0^\infty \tau_\nu d\nu$$

$$\frac{W_\lambda}{\lambda_0} = \frac{\lambda_0 \pi e^2}{m_e c^2} N_i f_{ij} \int \phi_\nu d\nu = \frac{\pi e^2}{m_e c^2} N_i \lambda_0 f_{ij}$$

A plot of $\log(W_\lambda/\lambda_0)$ vs. $\log(N_i f_{ij} \lambda_0)$ is a straight line and are linearly dependent, regardless of the shape of the line profile (see Fig. 1.2). However, these lines are sometimes too weak to have reliable measurement. 2. Flat part of COG: As the line strength keep increasing, the line centre or the Doppler core saturates when all the available photons are removed from the absorption profile. Then the increase in column density will hardly causes any changes in the equivalent width. This line is said to be saturated. However, with further increase in column density, the damping wings become more important and the line strength again increases. For an intrinsically broader spectral line with high kinetic temperature (T), the line profile spreads out over a larger velocity range, and more and more column density is needed for saturation. Therefore, one can easily assume that the strongly broadened lines saturate only at higher column density (N) values.

$$\tau_\nu = \frac{\pi e^2}{m_e c} f_{ij} N_i$$

For a thermally broadened line, the line profile at the peak frequency is,

$$\phi_0 = \frac{1}{\sqrt{\pi}} \frac{c}{\nu_0} \frac{1}{b} = \frac{1}{\sqrt{\pi}} \frac{\lambda_0}{b}$$

Then the optical depth at the line centre is

$$\tau_0 = \frac{\sqrt{\pi}e^2}{m_e c}\frac{N_i f_{ij}\lambda_0}{b}$$

For a given N, the larger the b value, the smaller is the optical depth at the line centre (τ_0) and the degree of saturation is small as well. Finally, the numerical integration of

$$W_\lambda = \lambda_0^2/c \int_0^\infty (1 - \exp(-\tau_\nu)d\nu$$

can be shown as,

$$W_\lambda = C.\sqrt{ln\tau_0}$$

where C is some constant. Thus, the dependence of W_λ on τ_0 or N is very small and the region is called flat part of COG. 3. Square root part of the COG: While the gaussian core of very strong lines saturates, the Lorentzian damping wings become more important as the optical depth increases. This is called square-root part of COG and can be shown as

$$\frac{W_\lambda}{\lambda_0} \propto \sqrt{N_i}$$

This region of COG is independent of b, showing that the gaussian turbulence is not capable of saturating the profile. These damping wings are not important in most of the lines in the diffuse ISM, except for the Lyman-alpha resonance line at 1216 Å (see Fig. 1.3).

Table 1.1 Different phases of ISM based on temperatures and particle number densities

Phases of ISM	Particle number density (cm^{-3})	Temperature Kelvin (K)
Cold Neutral Medium	$\sim$50	$\sim$100
Warm Neutral Medium	$\sim$1	$\sim$6000
Warm Ionized Medium	$\sim$0.1 to $\sim10^4$	$\sim10^4$
Hot ISM	$\sim$0.001	$\sim10^6$
Molecular Clouds	$\sim10^6$	$\sim$30

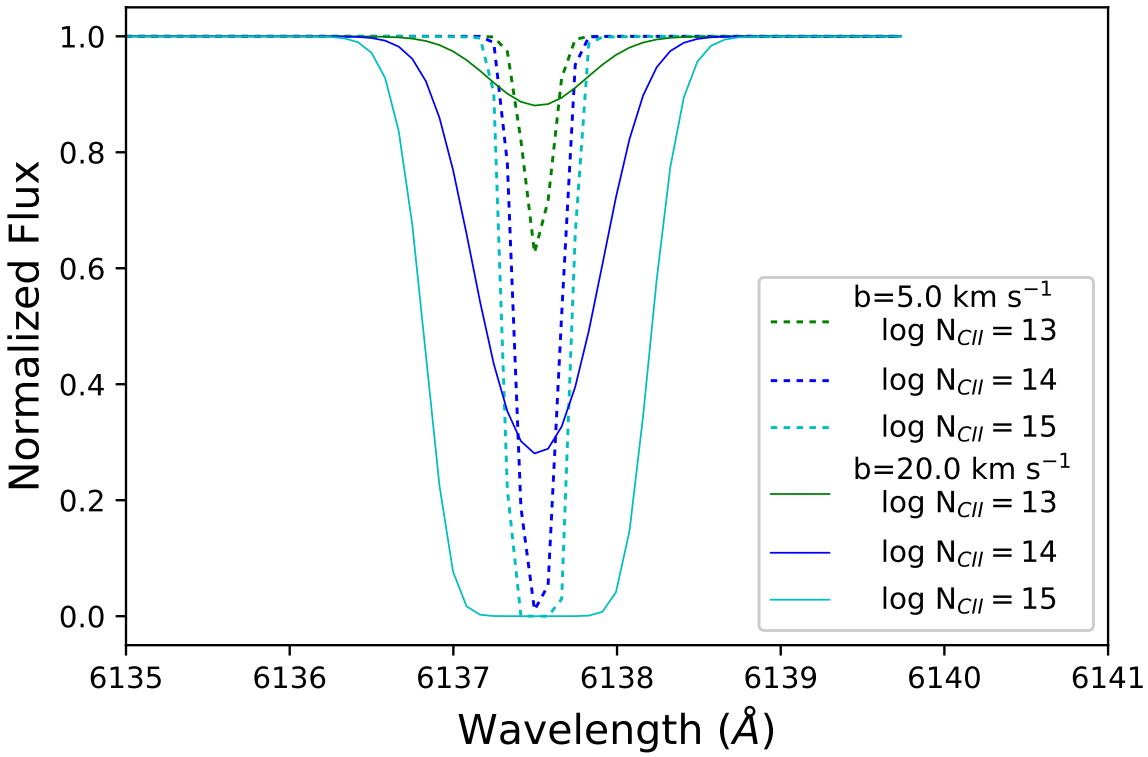

Figure 1.1 Theoretical Voigt profiles for the C II 1334 transition for different b-parameters. The Voigt profiles with dotted lines and solid lines are for b=5, and 20 km s^{-1}, respectively and column densities of log N_{CII} =13.00, 14.00, and 15.00 cm^{-2} each.

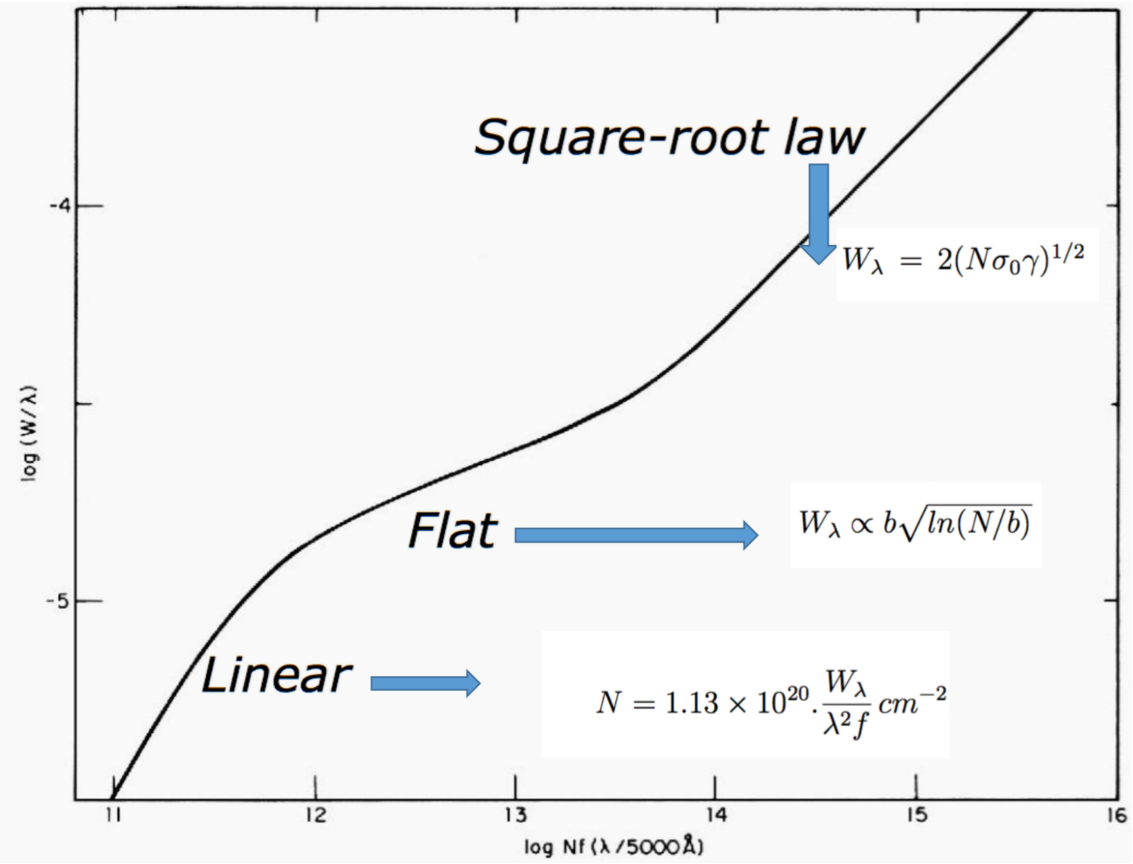

Figure 1.2 Figure showing linear, flat, and square root parts of curve of growth (COG).

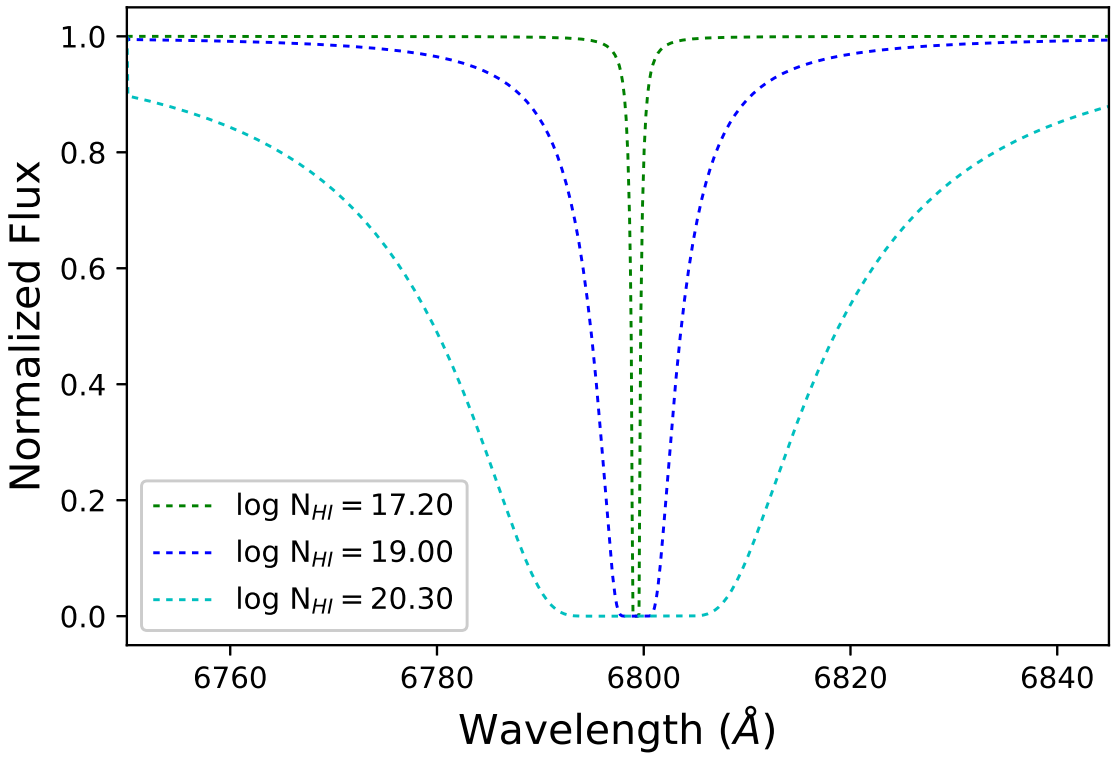

Figure 1.3 Theoretical Voigt profiles for the H I Lyman-alpha transition with b=10 km s^{-1} and column densities of log N_{HI} =17.20, 19.20, and 20.30. The Lorentzian profile dominates the Voigt profile with rising NHI. The damping wings start to become prominent for log N_{HI} >19.00.

Chapter 2

Quasar absorption line systems

Quasars are quasi-stellar objects with extra-galactic origins. Quasars are the farthest known sources and the most distant quasar discovered so far is at z=7.1 (Momjian et al., 2014). They have very high intrinsic luminosities of the order of $\sim 10^{46}$ ergs s^{-1} making them more luminous than a typical galaxy. They are believed to be powered by super-massive black holes at the centre of the galaxy. The spectral energy distributions (SED) of quasars are different from the stellar SED in the sense that they emit an abundance of high energy UV photons which is responsible for their intrinsic blue colors. As the blue intrinsic colors of high redshift quasars get shifted to visual wavelengths due to the Hubble expansion, they are best suited to observe from the ground based observatories.

Photons from a distant quasar traverse through the intergalactic medium, circum-galactic medium, and ISM get absorbed by the intervening gas of various densities and temperatures. Then the absorption features are imprinted in the spectrum of the quasar (see Fig. 2.1). Since hydrogen is the most abundant element in the universe, the majority of these absorption features are due to the hydrogen. The Lyman series lines of neutral hydrogen are the dominant transitions responsible for the absorption. Lyman-alpha which corresponds to a transition from n=1 to n=2 in the ground state of neutral hydrogen (at a rest wavelength of 1215.67 Å) is the strongest among the Lyman series lines and dominate the entire absorption features in a quasar spectrum. The presence of hydrogen Lyman-alpha in the spectra of background quasars was first realized immediately after Schmidt (1965) detected a number of quasars at sig-

nificant redshift (e.g. Gunn & Peterson 1965, Bahcall & Salpeter 1965). A number of large scale surveys later discovered more than 200,000 quasars turning the study of quasar absorption lines into modern paradigm. The majority of them were from Sloan Digital Sky Survey (York et al. 2000).

2.1 Lyman-alpha forest

The forest of hundreds of sharp and weak absorption lines with log N_{HI} <17.2 blueward to the Lyman-alpha emission peak from the quasar is called Lyman-alpha forest. Since each of these lines is redshifted by a different amount depending on the distances of corresponding gas clouds with respect to us, they appear spread out into a forest. The incidence rate of these absorbers in any given quasar sightline is much higher than that of the intervening galaxies suggesting that they may be separate from galaxies and show weak clustering properties. In fact, these absorbers are associated with intergalactic gas clouds which consist of highly ionized hot gas with temperature in the order of $\sim 4 \times 10^4$ K. These clouds contain majority of the baryonic matter in the universe (Petitjean et al. 1993). Moreover, the evolution of number of forest lines N with redshift z can be approximated by a power-law in (1+z),

$$\frac{dN}{dz} \propto (1+z)^{\gamma}$$

In the redshift range z$\sim$ 0 to $\sim$ 1.5, the number of forest lines do not seem to be evolved (0<$\gamma < \frac{1}{2}$). However, there is a sharp increase in the forest lines beyond z$\sim$1.5 (Kim et al. 2005) and by z$\sim$4, γ evolve up to a value of $\sim$ 5. Moreover, the uniformity of the the forest lines along sight lines in random directions may imply the large scale uniformity and isotropy of the universe.

2.2 Lyman limit systems

When the H I column densities are larger than N$\sim 10^{17}$ cm^{-2}, the gas clouds start showing discontinuity due to the continuous absorption beyond the the Lyman limit. Lyman limit corresponds to the rest frame wavelength of 912 Å, which is associated with the ionization potential of neutral hydrogen (13.6 eV). Thus gas clouds with column densities in the range of 10 ^{17} to 10^{19} cm^{-2} are classified as Lyman limit systems (LLS) and act as self shielding against ionizing radiation. So the ionization of LLS due to radiation from outside is less severe than the Lyman-alpha forests. In fact, at a column density of $10^{17.2}$ cm^{-2}, a gas cloud reaches a optical depth of $\tau = 1.0$ (optically thick) at rest frame wavelength of 912 Å making a meaningful transition between highly ionized Lyman forest systems and moderately ionized LLS.

2.3 Damped Lyman-alpha systems

With further increase in column density beyond 10^{19} cm^{-2}, the gas in the clouds become so optically thick that it is almost completely self-shielded and mostly neutral. Furthermore, the clouds with N$> 10^{19}$ exhibit damping wings as the Lorentzian component of the Voigt profile, which arises due to the finite lifetime of Lyman-alpha transition, becomes dominant. These systems are further classified into two sub groups: sub-DLAs with neutral hydrogen column densities in the range of 10^{19} to $10^{20.3}$ and DLAs with N$> 10^{20.3}$. Unlike LLS, the DLAs and sub-DLAs are mostly neutral and unaffected by the ionization and thus their observed metallicities represent true chemical enrichment in the gas.

DLAs dominate the neutral mass gas density in the Universe. Moreover, DLAs contain sufficient neutral gas mass to contribute a significant fraction of visible stellar mass in typical galaxies at z$\sim$ 3.0 to 4.5 (e.g. Storrie-Lombardi & Wolfe 2000). It is thus customary to consider damped Lyman-alpha systems as an important neutral gas

reservoirs for star formation at high redshifts (e.g. Nagamine, Springel, & Hernquist 2004a). The mass per unit comoving volume of neutral gas in damped Lyman alpha systems at redshift z per unit critical density, ρ_{crit} can be expressed in terms of column density distribution finction, $f(N, X)$

$$\Omega_g = \frac{H_0}{c}\frac{\mu m_H}{\rho_{crit}}\int_{N_{min}}^{N_{max}} dN N f(N, X) = \frac{H_0}{c}\frac{\mu m_H}{\rho_{crit}}\frac{\sum_{i=1}^{n} N_i}{\Delta X}$$

where μ is the mean molecular weight which includes the contribution of He to the neutral gas content and other symbols have their usual meanings. The column density distribution function $f(N, X)$ at a particular redshift z is defined as the number of absorbers in a given column density range (N, N+Δ N) with a total absorption distance ΔX. The Column Density Distribution Function (CDDF) at $< z >$=2.8 for Lyman-alpha lines in quasar spectra is shown in Fig. 2.2. The Lyman-alpha forest, LLS, sub-DLA, and DLA data are from Petitjean et al. (1993). The solid green line represents a single power law with index $\alpha = -1.49$ which provides a reasonable fit to the data over ~ 8 orders of magnitude. In the above expression, the integral sign is replaced with summation in the discrete limit. This relation was first derived by Wolfe (1986) and Lanzetta, Wolfe, & Turnshek (1995) and showed that damped Lyman-alpha systems dominate the neutral gas contents of the Universe at $1.6 < z < 5.0$. In fact, the damped Lyman-alpha systems offer most precise metallicity measurements independent of electron temperature. These systems can thus complement the abundance measurements in Lyman-break galaxies (LBGs) or UV selected star forming galaxies (e.g. Shapley et al. 2004, Erb et al. 2006).

2.4 Metallicity evolution and dust depletion in DLAs

From a number of previous observations, DLA metallicity is observed to decrease gradually from redshift $z = 0$ to $z = 4$ with a rate of about 0.2 dex per redshift (e.g. Kulkarni & Fall 2002, Prochaska et al. 2003a, Kulkarni et al. 2005, Kulkarni et al.

2007, Rafelski et al. 2012, Jorgenson et al. 2013, Som et al. 2013, Som et al. 2015, Quiret et al. 2016). However, the DLA metallicity evolution at high redshift is still unclear, primarily due to inadequate sample having robust measurements of dust-free metallicity. Some previous studies (e.g. Rafelski et al. 2012, Rafelski et al. 2014) reported a sudden decline of DLA metallicity at $z > 4.7$, suggesting a sudden change in the chemical enrichment process. However, such a sudden drop would be expected to be associated with a sudden change in the chemical enrichment process, which is not observed. Indeed, the observed star formation history of galaxies based on UV and IR observations, shows no sudden change at $4 \lesssim z \lesssim 8$ (Madau & Dickinson 2014). Recent studies (e.g. Morrison et al. 2016, De Cia 2018) have shown that the sudden drop reported at $z > 4.7$ can be explained in terms of dust depletion, which cannot be ignored even at $z \sim 5$. As observed in the Milky Way (MW) Interstellar Medium (ISM), elements with a higher condensation temperature (e.g, Si, Fe etc) are subject to more depletion into dust grains than elements with a relatively lower condensation temperature (S, O, Zn etc). Even in DLAs the depletion is more severe for refractory elements like Si, Fe, than for volatile elements O, S (De Cia et al. 2016).

Evolution of metallicity as a function of redshift is a powerful tracer of the cosmic star formation history. It is therefore important to determine the metallicity evolution of DLAs/sub-DLAs accurately. Given the potentially interesting implications of a sudden drop in metallicity at z$\sim$5 and the conflict such a drop would produce with existing chemical evolution models, it is especially important to check with a larger sample whether or not such a sudden drop in metallicity actually exists. With this goal, we have been expanding measurements of S and/or O in other DLAs at $z \geq 4.5$. Here we present results of VLT, Keck, and Magellan observations of 10 absorbers in this redshift range. Inclusion of these new measurements increases the current high-z sample of volatile elements significantly, and thus offers a better understanding of DLA metallicity evolution at $z \sim 5$. This work is already published in Poudel et al.

(2018) and Poudel et al. (2019). Therefore, the work published in these papers is presented as part of this dissertation (Chapter 3 to Chapter 6).

2.5 Metal-poor DLAs as probes of early nucleosynthesis

Metal abundance measurements throughout the cosmic ages track the history of galaxy formation and evolution from the initial pristine stars and galaxies to the present day metal-rich galaxies. At $z \sim 5$, the cosmic stellar mass density is expected to have doubled every 300 Myr (e.g. Gonzalez et al. 2011). As a result, due to the finite age of the universe, metals observed in absorption at this epoch are only a few hundred million years old and are produced either by core-collapse supernovae of the massive metal-poor stars or by pair-instability supernovae. Therefore, the first 1 billion years of the cosmic metal evolution are influenced by the nucleosynthetic signatures from the early stars, and measuring abundances during the $z \sim 5$ epoch can constrain the nature of the pristine Population III stars and the metal-poor Population II stars. The initial mass function of Population III stars is still a subject of debate, some studies suggest masses as high as 100 $M_{\odot}$ (e.g. Bromm et al. 1999, Nakamura & Umemura 2001, Abel et al. 2002), where other studies suggest somewhat smaller values. For example, fragmentation due to turbulence can result in smaller Population III IMF (Initial Mass Function) (Clark et al. 2011), and multiple smaller Population III stars can be formed in a given minihalo (e.g. Stacy & Bromm 2013, Hirano et al. 2014, Stacy et al. 2016). Measurements of relative abundances such as [C/O] in chemically young systems can put a strong constraint on the mass of the progenitor Population III stars (e.g. Cooke et al. 2017).

Recent surveys have found several putative second generation stars in the Milky Way having chemical fingerprints of the elements that were made during the life of the Population III stars (e.g. Frebel & Norris 2015). A wide varieties of chemical abundance patterns are uncovered by these surveys. For example, many carbon-

enhanced metal-poor stars (CEMP) are found which are enhanced with light elements relative to heavy elements (e.g. Beers & Christlieb 2005). Moreover, a star with apparently no iron was reported in Keller et al. (2014). The abundance patters of these metal-poor stars are even reproduced by Population III stellar nucleosynthesis models (e.g. Heger & Woosley 2010, Cooke & Madau 2014, Tominaga, Iwamoto, & Nomoto 2014).

The most metal-poor DLAs may complement the metal-poor stars as they are believed to be distant protogalaxies at the early stage of cosmic chemical evolution (e.g. Erni et al. 2006, Cooke et al. 2011) and the metal-poor stars may have been condensed out of a metal-poor DLA itself. Moreover recent hydrodynamical simulations suggest that metal-poor DLAs may have been enriched by just a few supernova explosions (e.g. Bland-Hawthorn, Sutherland & Karlsson 2011). In fact, several studies have been carried out to identify the chemical fingerprints of first stars in the most metal-poor DLAs (e.g. Erni et al. 2006, Pettini et al. 2008, Penprase et al. 2010, Cooke et al. 2011, Cooke et al. 2017). In this dissertation, we have selected three relatively metal-poor z$\sim$5 DLAs to compare with the nucleosynthesis models of massive metal-free stars from Heger & Woosley (2010).

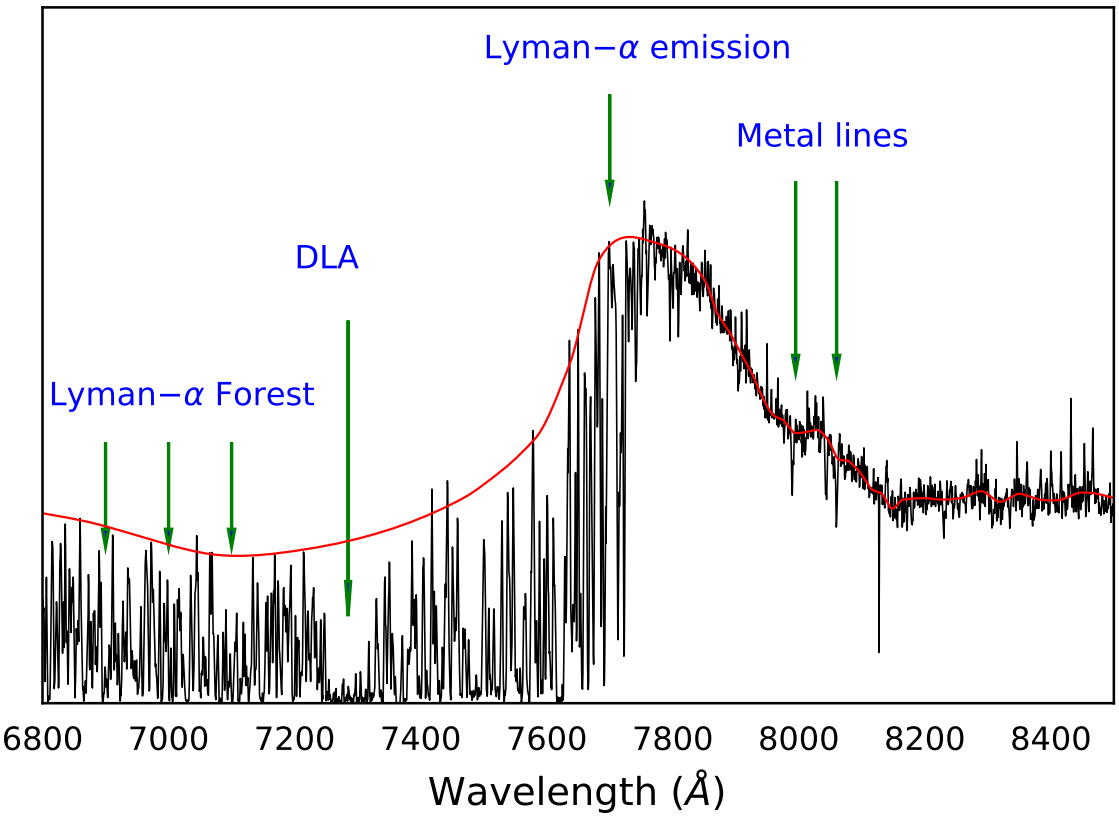

Figure 2.1 A typical spectrum for a quasar at $z \sim 5$ from our sample showing different absorption and emission features from intervening galaxies and the quasar itself. The red solid line shows the quasar continuum level (what the spectrum would look like if it was unaffected by absorption).

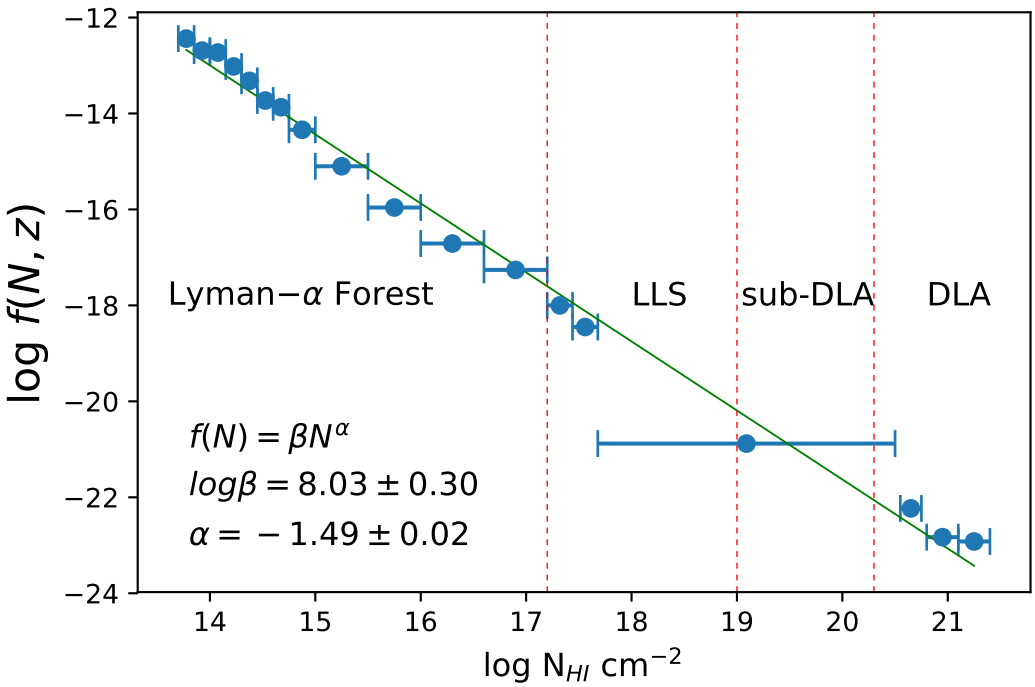

Figure 2.2 The Column Density Distribution Function (CDDF) at $< z >$=2.8 for Lyman-alpha lines in quasar spectra. The Lyman-alpha forest, LLS, sub-DLA, and DLA data are from Petitjean et al. (1993). The solid green line represents a single power law with index $\alpha = -1.49$ which provides a reasonable fit to the data over $\sim$ 8 orders of magnitude.

Chapter 3

Observations and data reductions

This chapter discusses the characteristics of the individual spectrographs used for our observations, lists the properties of the quasar sightlines, introduces the data reduction methods and pipelines, and explains the technique for abundance measurements.

3.1 ESI observations and data reductions

Echellette Spectrograph and Imager (ESI) is a visible-wavelength imager and single-slit spectrograph on the Keck II telescope. It can reach up to the resolving power of 13,000 with cross-dispersed spectroscopy mode along a 20 arcsec slit and a resolution of 1000-6000 in low-dispersion spectroscopy mode with 8 arcmin slit.

The ESI data for J0231-0728 that included two exposures of 1800 s each, were downloaded from the Keck Observatory Archive (KOA), and consisted of observations as a part of program C70E (PI S. Djorgovski). The details of the sight line and the absorber are given in Table 3.1. The data were reduced and 2-D spectra were extracted using ESIRedux, an IDL-based reduction package written by J. X. Prochaska. Individual spectra were normalized by fitting a cubic spline polynomial, typically of an order between 2 to 7, using the CONTINUUM task in IRAF[1] and were combined thereafter.

[1]IRAF is distributed by the National Optical Astronomy Observatory, which is operated by the Association of Universities for Research in Astronomy, Inc., under cooperative agreement with the National Science Foundation.

3.2 MagE observations and data reductions

The Magellan Echellette (MagE) spectrograph, a moderate-resolution optical echellette mounted on Magellan II telescope has a wavelength coverage of approximately 3100-10,000Å. The observation of quasar sightline to J0306+1853 was taken on 2014 January with 5400 s (three exposures of 1800 s each) of integration time. The details of the sightline and absorber are given in Table 3.1. MagE optical spectrum which provides a spectral resolution of 4100 was taken with 1" slit. The data were reduced using a custom-built pipeline and flux-calibrated using techniques described in Becker et al. (2015). Individual spectra were continuum normalized by fitting a cubic spline polynomial, typically of an order between 1 to 6 using IRAF.

3.3 X-shooter observations and data reductions

X-shooter is a medium resolution spectrograph mounted on Very Large Telescope (VLT) which consists of three spectroscopic arms, each with optimized optics, dispersive elements, and detectors. The UVB, VIS, and NIR arms have wavelength coverage 300-559.5 nm, 559.5-1024 nm, and 1024-2480 nm respectively.

Two exposures each of 1800 s for the sightlines J0824+1302 and J1233+0622 were taken on 2014 December 15 as a part of the program 094.A-0793(A) (PI. S. Quiret). The details of the sight lines and absorbers are given in Table 3.1. The X-Shooter Common Pipeline Library (Goldoni 2006) release 6.5.1[2] was used to reduce the science raw images and to produce the final 2-D spectra. All of our science data were taken in the nodding mode, so a standard procedure of data reduction was used as follows. An initial guess was first computed for the wavelength solution and the position of the centre and the edges of the orders. Then the accurate position of the centre of each order was traced, and this step was followed by generating the

[2]http://www.eso.org/sci/facilities/paranal/instruments/xshooter/

master flat frame out of five individual lamp flat exposures. Next a 2-D wavelength solution was found, and it was modified by applying a flexure correction to correct for the shifts that can be of the order of the size of a pixel. Finally, having generated the required calibration tables, each pair of science frames was reduced to obtain the flat-fielded, wavelength-calibrated and sky-subtracted 2-D spectrum. The 1-D flux of the quasar was extracted using a spectral point spread function (SPSF) subtraction as described in Rahmani (2016). In summary, the quasar's PSF was modeled using a Moffat function whose FHWM and centre were smooth functions of wavelength. The light profile was then integrated at each wavelength to obtain the quasar's flux. Finally, Individual spectra were first continuum normalized by fitting a cubic spline polynomial typically of an order between 1 to 6 using CONTINUUM task in IRAF.

3.4 MIKE observations and data reductions

Magellan Inamori Kyocera Echelle (MIKE) is a double echelle spectrograph on the Magellan Clay telescope at Las Campanas observatory in Chile. The first optical element in the spectrograph reflects and transmits light into blue and red arms of the spectrograph respectively. The spectrograph has full wavelength coverage from about 3350-5000 Å in blue ccd and 4900-9500 Å in red ccd in its standard configuration. Though the dichroic and gratings are permanent elements of the spectrograph, one can still choose different grating angles to select a different set of orders to go down to 3200 Å on the blue side and up to 10,000 Å on the red side.

Two of the quasars J1557+1018 and J1253+1046 probing three absorbers were observed in April 2017 (PI: Frye, 2017A). Observations were carried out with a 1" slit, and reached a spectral resolution of ∼22,000 with the red arm and ∼28,000 with the blue arm, giving a combined wavelength coverage of 3500 to 9400 Å. The details of the sight lines and absorbers are given in Table 3.1. The MIKE data were reduced using the MIKE pipeline reduction code written in IDL and developed by

S. Burles, J. X. Prochaska and R. Bernstein. The reduction package performs all the necessary steps for bias subtraction, flat fielding and sky-subtraction. Before and after each science exposure, comparison exposures using the Th-Ar lamp were taken for wavelength calibration purposes. After the calibration and the heliocentric velocity corrections, the pipeline extracts each individual echelle order from all the exposures. Multiple exposures were first continuum normalized by fitting a cubic spline polynomial and combined to facilitate the rejection of cosmic rays.

3.5 Voigt profile fitting and abundance measurements

This section discusses the line fitting and the abundance measurements.

3.5.1 Voigt profile fitting

We used the Voigt profile fitting program, VPFIT[3] v. 10.0 for the determination of column densities of metal lines and neutral hydrogen. VPFIT minimizes the χ^2 residual between the data and theoretical Voigt profiles convolved with the instrumental line spread profile through multiple iterations. VPFIT makes it possible to perform simultaneous multi-component Voigt profile fitting of multiple lines of multiple ions, while allowing the Doppler b parameters and redshifts of the corresponding components to be tied together. The rest-frame wavelengths and oscillator strengths used for the Voigt profile fitting were taken from Morton (2004) and Cashman et al. (2017). While the line blending can be an issue with lower resolution spectrographs, four out of the ten absorbers in our sample have a relatively higher resolution of 13.7 km s^{-1} which can resolve the blending of metal lines. For many of the systems we were also able to use multiple lines to minimize the error caused by possible saturation effects (e.g. Penprase et al. 2010). The fitted column densities and associated uncertainties determined with VPFIT were confirmed by comparing the calculated and observed

[3]https://www.ast.cam.ac.uk/rfc/vpfit.html

line profiles (in the core as well as the wings) and verifying that the profiles agreed within the noise level present. Another potential issue with high-redshift systems is the severe blending of metal lines with hydrogen lines in the dense Lyman forest. However, all of the lines used for the column density determinations were outside the Lyman-alpha forest and were not affected by the forest lines.

Another challenge affecting high-redshift systems is the continuum normalization blueward of the Lyman-alpha emission. This is partly due to severe blending with the Lyman-alpha forest and partly because of the relatively low signal-to-noise ratio for the faint quasars. The typical resolution of 13 - 55 km s^{-1} used for most of our absorbers, was adequate to resolve the forest for determining the neutral hydrogen column density. For each sightline, we selected the entire available spectrum blueward of the Lyman-alpha emission for the continuum normalization. In most cases, the spectra had covered at least the first three Lyman-series lines. Regions of the spectra unaffected by any absorptions were then selected through which the continuum would pass. Then Spline polynomial typically of the order of 5 was fitted to the continuum using the CONTINUUM task of IRAF. Moreover, we estimate the average uncertainty contributed to the H I column densities due to error in continuum placement by changing the continuum up and down by 1 σ uncertainties, renormalizing the continuum at those levels, and refitting the Voigt profiles. The errors in H I column densities resulted by changing the continuum placement were typically of the order of 0.1 dex or lower. For most of the systems, the H I column densities were measured by fitting Voigt profiles to the Lyman-alpha lines to estimate the column density taking the core and the wings of the profiles into consideration. In some cases, we were also able to use both the Lyman-beta and the Lyman-alpha lines to estimate the H I column densities. For example, while the Lyman-alpha lines for the absorbers at z=4.589, 4.600 along the sightline to the quasar J1253+1046 were blended to each other, we were able to make a joint fit of Lyman-alpha and Lyman-beta lines of these

two systems together, resulting into better constraints to estimate the H I column densities for both the absorbers. However, in most of our systems, the other Lyman-series lines beyond Lyman-alpha were not useful partly due to the severe blending of these weaker lines with the dense Lyman forest at these high redshifts and partly due to high noise level. To estimate the uncertainties in the H I column densities, we examined the range of values for which the fitted profiles are consistent with the observed data within the noise level.

3.5.2 Abundance measurements

The abundances of each element X were calculated using the relation,

$$[X/H] = log(N_X/N_{H\,I}) - log(X/H)_\odot$$

where N_X is the column density of element X, $N_{H\,I}$ is the neutral hydrogen column density and log $(X/H)_\odot$ is the solar abundance of the element X. The solar abundances were adopted from Asplund et al. (2009).

We have not made ionization corrections to any of the abundances since observations of higher ionization lines are not available to place constraints on the ionization parameter. In any case, the ionization corrections are expected to be negligible for DLAs and $\lesssim 0.2$ dex for sub-DLAs (e.g. Dessauges-Zavadsky et al. 2003, Meiring et al. 2009, Cooke et al. 2011, Som et al. 2015).

To summarize, we applied following sequence of steps to estimate the abundances.

1. Observations and data reduction
2. Extraction of 1-dimensional spectra
3. Continuum fitting
4. Velocity plots for metal lines
5. Identify the redshift of the absorbers from the metal lines

6. Voigt profile fitting for metal lines and H I lines

7. Estimation of the abundances

Table 3.1 Summary of targets and observations

QSO	m_i	z_{em}	z_{abs}	log $N_{H\,I}$	Instrument	Exposure Time (s)
J0231-0728	19.48	5.423	5.335	20.10	ESI	3,600
RA:02:31:37.65						
Dec:-07:28:54.5						
J0306+1853	17.96	5.363	4.987	20.60	MagE	5,400
RA:03:06:42.51						
Dec:+18:53:15.8						
J0824+1302	19.95	5.212	4.809	20.10	X-Shooter	7,200
RA:08:24:54.01			4.829	20.80		
Dec:+13:02:16.8						
J1233+0622	20.09	5.311	4.859	20.75	X-Shooter	3,600
RA:12:33:33.47			5.050	20.10		
Dec:+06:22:34.3						
J1253+1046	19.40	4.925	4.589	19.75	MIKE	8,100
RA:12:53:53.35			4.600	20.35		
Dec:+10:46:03.1			4.793	19.65		
J1557+1018	19.98	4.765	4.627	20.75	MIKE	13,500
RA:15:57:00.17						
Dec:+10:18:41.8						

Chapter 4

Results of individual absorbers

Here we discuss the estimation of H I and metal column densities for individual absorbers using Voigt profile fitting. Moreover, we also present the estimation of velocity widths of key metal lines to study the gas-kinematics of the absorbers.

4.1 Absorber at $z = 5.335$ toward J0231-0728

Voigt profile fitting to the Lyman$-\alpha$ line for this absorber gave a column density log $N_{H\,I} = 20.10 \pm 0.15$ and is shown in Fig. 4.1. While the wings for this Lyman$-\alpha$ line are severely blended, we were able to constrain the fit by checking the data and the fitted profiles at multiple locations near the core (near 7690, 7710 Å) and at multiple points in the continuum unaffected by blending (near 7645, 7750, 7765 Å), so that the flux difference between the observed data and the fitted profile is consistent with the 2σ error in the normallized flux. We also note that in this particular case, the right wing of the line was more useful for constraining the continuum fit. The results from Voigt profile fitting for the metal lines are summarized in Table 4.1 and the relative abundances are summarized in Table 4.2. Total element abundances for O, C and Si were calculated using O I λ1302, C II λ1334 and Si II λ1260 respectively. The metallicity for this system based on the measurement of O is -2.24 ± 0.16 dex. The Voigt profile fitting for the metal lines of this absorber is shown in Fig. 4.2. Fig. 4.3 shows the optical depth and the absorption fraction as a function of radial velocity for the fitted profile O I λ1302 which shows a velocity dispersion of 172 km s^{-1}.

4.2 Absorber at $z = 4.987$ toward J0306+1853

This absorber was initially reported in Wang et al. (2015). We reanalyzed this system by doing Voigt profile fitting for O I λ1302, Si II λ1304, and C II λ1334. Fig. 4.4 and Fig. 4.5 show the Voigt profile fits for the estimation of hydrogen and metal column densities, respectively. This system is observed to be a metal-poor DLA with $\log N_{H\,I} = 20.60 \pm 0.15$ and [O/H]$= -2.69 \pm 0.17$. While our estimate of $N_{H\,I}$ is consistent with the estimate $\log N_{H\,I} = 20.50^{+0.10}_{-0.12}$ of Wang et al. (2015), our estimation for metal column densities are different as Wang et al. 2015 had used the apparent optical method. Since the Si II λ1526 line was blended significantly, we used Voigt profile fitting only for the Si II λ1304 line and got a lower Si II column density $\log N_{Si\,II} = 14.22$. Fig. 4.6 shows the optical depth and the absorption fraction as a function of radial velocity for the fitted profile O I λ1302 which shows a velocity dispersion of 328 km s^{-1}.

4.3 Absorber at $z = 4.809$ toward J0824+1302

Voigt profile fits to the Lyman-α and Lyman-β lines for this absorber are shown in Fig. 4.7. We estimated an H I column density of $\log N_{H\,I} = 20.10 \pm 0.15$. The Voigt fitting for metal lines is shown in Fig. 4.8 and the results are summarized in Table 4.5. The metallicity for this system based on the measurement of O is -2.51 ± 0.16 dex. The relative abundances are summarized in Table 4.6. Fig. 4.9 shows the C II absorption in this absorber is spread over a velocity width of 69 km s^{-1}. Moreover, the overall enhancement of Si with respect to C and O makes this absorber very peculiar suggesting the effect of an unusual nucleosynthetic history.

4.4 Absorber at $z = 4.829$ toward J0824+1302

Fig. 4.10 shows the Voigt profile fits to the Lyman-β and Lyman-γ lines for this absorber which gave an H I column density of $\log N_{H\,I} = 20.80 \pm 0.15$. The metal lines fitting are shown in Fig. 4.11. The results from Voigt profile fitting for these metal lines are summarized in Table 4.7 and the relative abundances are summarized in Table 4.8. As the O I λ1302 alone is saturated, we use both O I λ972 and O I λ1302 to constrain the O I column density. Despite O I λ972 for this absorber falls in the Lyman-α forest, it is less saturated than O I λ1302. We use both the cores and the wings of the lines to estimate that $\log N_{O\,I}$ cannot be much lower than 15.29 or much higher than 15.59. So, we adopt $\log N_{O\,I} = 15.44 \pm 0.15$. The metallicity for this system based on the measurement of O is -2.05 ± 0.21 dex. The gas in this absorber is spread over a velocity width of 74 km s^{-1} as shown in Fig. 4.12.

4.5 Absorber at $z = 4.859$ toward J1233+0622

The Voigt profile fits for the Lyman-alpha is shown in Fig. 4.13, probing a DLA at $z = 4.859$ with $\log N_{H\,I} = 20.75 \pm 0.15$. The Voigt profile fits for the metal lines are shown in Fig. 4.14. The results from Voigt profile fitting and the relative abundances are summarized in Table 4.9 and Table 4.10, respectively. The C II λ1334, Fe II λ2600, and Si II λ1527 lines are detected for this system. However, the high- and low-velocity components for the O I λ1302 line are blended with telluric absorption. However, we are able to estimate the lower limit of the O I λ1302 column density by overfitting the profile for the central main component, fixing the redshift and Doppler b parameter determined in C II λ1334. Taking only this central component (excluding the other components that are heavily blended with telluric absorption features), we place a lower limit on [O/H] > -2.14. For C II λ1334, we have analyzed the effect of changing the column density for the strongest component in steps of 0.1 dex. The difference

between the profile and the data becomes large, considering the 1σ uncertainty in the normalized flux, if the C II column density is increased by > 0.1dex compared to the adopted value of 14.42. This is consistent with the uncertainty of 0.07 dex obtained from VPFIT (see Fig. 4.15). Fig. 4.16 shows that this absorber is spread over a large radial velocity range with several components detected with X-Shooter resolution.

4.6 Absorber at $z = 5.050$ toward J1233+0622

The Voigt profile fits for the Lyman-alpha is shown in Fig. 4.17, probing a sub-DLA at $z = 5.050$ with $\log N_{H\,I} = 20.10 \pm 0.15$ along the same quasar sight line to J1233+0622. The Voigt profile fits for the metal lines are shown in Fig. 4.18. The results from Voigt profile fitting and the relative abundances are summarized in Table 4.11 and Table 4.12, respectively.

Furthermore, we have analyzed the effect of changing the column density for the strongest component both in O I λ1302 and C II λ1334 in steps of 0.1 dex. The difference between the data and the profile becomes large, considering the 1 σ uncertainty in the normalized flux, if the column density is increased by >0.1 dex for O I and >0.2 dex for C II compared to the adopted column density values (see Fig. 4.19 and Fig. 4.20). Thus the uncertainties in the column densities are consistent with the values obtained from VPFIT (0.12 dex for O I and 0.16 dex for C II). As Si II λ1527 is saturated, we used Si II λ1304 to estimate the abundance for silicon. While oxygen and carbon are detected in multiple components, the absence of some corresponding components in silicon might suggest spatial variation in the dust depletion. This is also a metal-rich absorber which shows multiple components spread over a large radial velocity range with [O/H] of -1.60 ± 0.18. Fig. 4.21 shows the optical depth and the absorption fraction as a function of radial velocity for the fitted profile Si II λ1304 which shows a velocity dispersion of 114 km s^{-1}.

4.7 Absorber at $z = 4.589$ toward J1253+1046

The sight line to quasar J1253+1046 probes a sub-DLA at a redshift $z = 4.589$. Although the Lyman-alpha for this absorber is heavily blended with a nearby absorber, we were able to make a joint fit of Lyman-alpha and Lyman-beta for both the absorbers at z=4.589 and z=4.600 and estimate $\log N_{H\,I} = 19.75 \pm 0.15$ for this absorber. The Voigt profile fits for the Lyman-beta and Lyman-alpha are shown in Fig. 4.22 and Fig. 4.23, respectively. The Voigt fits for the metal lines are shown in Fig. 4.24. The results from Voigt profile fitting and the relative abundances are summarized in Table 4.13 and Table 4.14, respectively. O I λ1302 is saturated, but based the O I column density for the strongest component cannot be higher by > 0.2 dex than the adopted value due to the effect in the line wings (see Fig. 4.25). Also, the difference between the data and the profile for C II λ1334 becomes large if the column density is increased by >0.2 dex compared to the adopted value, which is consistent with the uncertainty of 0.22 dex obtained from VPFIT (see Fig. 4.26). The [O/H] value of -1.38 ± 0.17 for this absorber suggests this as a metal-rich sub-DLA. Besides the main component, oxygen is the only element showing multiple components, one at -40 km s^{-1} and another at 43 km s^{-1}. Oxygen seems to be enhanced over silicon suggesting possible depletion into dust grains. Finally, Fig. 4.27 shows the optical depth and the absorption fraction as a function of radial velocity for the fitted profile Si II λ1527 which shows a velocity dispersion of 25 km s^{-1}.

4.8 Absorber at $z = 4.600$ toward J1253+1046

The quasar sight line to J1253+1046 also shows a DLA absorber at $z = 4.600$. The column density estimation after making a joint fit of Lyman-alpha and Lyman-beta of the two nearby absorbers together gives $\log N_{H\,I} = 20.35 \pm 0.15$. O I λ1302, C II λ1334, Si II λ1304, Si II λ1527, and Fe II λ1608 are detected in this absorber and

the corresponding Voigt profile fits are shown in Fig. 4.28. The results from Voigt profile fitting and the relative abundances are summarized in Table 4.15 and Table 4.16, respectively. This is a metal-rich DLA, [O/H] has a lower limit of -1.46. Since C II λ1334 is also saturated, we adopted a lower limit. This absorber also shows spatial variation in the relative abundances as two extra components are detected in O I λ1302 but not in silicon and carbon. Finally, Fig. 4.29 shows the optical depth and the absorption fraction as a function of radial velocity for the fitted profile Si II λ1304 which shows a velocity dispersion of 88 km s^{-1}.

4.9 Absorber at $z = 4.793$ toward J1253+1046

This is the second sub-DLA detected along the same sight line to J1253+1046 with $\log N_{HI} = 19.65 \pm 0.10$. Besides O I λ1302.2, C II λ1334.5, Si II λ1304.4, Si II λ1260.4, Si II λ1527, this absorber also shows detection of S II $\lambda\lambda$1254,1260. The corresponding Voigt profile fits for the Lyman-alpha and metal lines are shown in Fig. 4.30 and Fig. 4.31. The results from Voigt profile fitting and the relative abundances are summarized in Table 4.17 and Table 4.18, respectively. Since O I λ1302 is saturated, the abundance based on Voigt profile fitting has a lower limit of -1.63. However, the difference between the data and the profile for C II λ1334 becomes large if the C II column density is increased by >0.2 dex compared to the adopted value, which is consistent with the uncertainty of 0.17 dex obtained from VPFIT (see Fig. 4.32). Moreover, the sulphur abundance is significantly higher with a value of [S/H] $= -0.59 \pm 0.20$. In fact, such a high metallicity is quite rare in DLAs even at z < 2. Also, Si shows a much smaller abundance than S, suggesting strong dust depletion. To date, this absorber has the highest metallicity among $z > 4.5$ sub-DLAs or DLAs. Finally, Fig. 4.33 shows the optical depth and the absorption fraction as a function of radial velocity for the fitted profile S II λ1260 which shows a velocity dispersion of 21 km s^{-1}.

4.10 Absorber at $z = 4.627$ toward J1557+1018

The sight line to J1557+1018 shows a DLA at $z = 4.627$ that was estimated by Noterdaeme et al. 2012 to have $\log N_{H\,I} = 21.30$ based on its SDSS spectrum. Based on our higher resolution MIKE spectrum, we get a value of $\log N_{H\,I} = 20.75 \pm 0.15$. The Voigt profile fits for the Lyman-alpha and metal lines are shown in Fig. 4.34 and Fig. 4.35. The results from Voigt profile fitting and the relative abundances are summarized in Table 4.19 and Table 4.20, respectively. However, we note that the S/N at the position of the Lyman-alpha line is low. Higher S/N data would be useful to obtain a more definitive determination of $N_{H\,I}$ in this absorber. All the accessible absorption lines in this absorber are saturated. Thus we can estimate only lower limits on the metal column densities and the corresponding element abundances. For example, based on O I λ1302, we estimate [O/H] $\geq$ -1.47. This DLA is thus remarkably metal-rich for its high redshift. Finally, Fig. 4.36 shows the optical depth and the absorption fraction as a function of radial velocity for the fitted profile Si II λ1304 which shows a velocity dispersion of 209 km s^{-1}.

Table 4.1 Results of Voigt profile fitting for different elements in the $z = 5.335$ absorber toward J0231-0728

z	b_{eff} (km s^{-1})	$\log N_{O\,I}$	$\log N_{C\,II}$	$\log N_{Si\,II}$
5.33218	10.20		13.36 ± 0.17	
5.33286	18.37		13.40 ± 0.11	12.65 ± 0.03
5.33385	12.71	13.24 ± 0.31		
5.33505	13.53	14.41 ± 0.05	13.54 ± 0.10	12.91 ± 0.06
5.33636	72.73	13.89 ± 0.15	13.83 ± 0.07	13.08 ± 0.05
Total log N		14.55 ± 0.05	14.18 ± 0.05	13.39 ± 0.03

Table 4.2 Abundances of different elements in the $z = 5.335$ absorber toward J0231-0728

Element	[X/H]	[X/O]
O	-2.24 ± 0.16	
C	-2.35 ± 0.16	-0.11 ± 0.07
Si	-2.22 ± 0.15	0.02 ± 0.06

Table 4.3 Results of Voigt profile fitting for different elements in the absorber at z=4.987 toward J0306+1853.

z	b_{eff} (km s^{-1})	log $N_{O\,I}$	log $N_{C\,II}$	log $N_{Si\,II}$
4.98241	5.23 ± 7.14	...	13.40 ± 0.18	...
4.98436	4.54 ± 2.09	13.86 ± 0.12	...	13.68 ± 0.09
4.98661	8.54 ± 1.63	14.28 ± 0.16	14.13 ± 0.15	13.90 ± 0.07
4.98808	4.53 ± 7.14	...	13.88 ± 0.28	...
4.99010	7.44 ± 3.41	14.14 ± 0.06	...	13.58 ± 0.07
Total log N	...	14.60 ± 0.08	14.37 ± 0.13	14.22 ± 0.05
AOD log N	...	14.48 ± 0.03	14.12 ± 0.04	14.05 ± 0.04

Table 4.4 Abundances of different elements in the $z = 4.987$ absorber toward J0306+1853

Element	[X/H]	[X/O]
O	-2.69 ± 0.17	
C	-2.66 ± 0.19	0.03 ± 0.15
Si	-1.89 ± 0.16	0.79 ± 0.09

Table 4.5 Results of Voigt profile fitting for different elements in the $z = 4.809$ absorber towards J0824+1302

z	log $N_{O\,I}$	log $N_{C\,II}$	log $N_{Si\,II}$	log $N_{Fe\,II}$
4.80082	13.22 ± 0.28			
4.80253	13.01 ± 0.29	13.13 ± 0.19		
4.80900				13.12 ± 0.17
4.80922	14.18 ± 0.06	13.62 ± 0.10		
4.81030	13.13 ± 0.29	12.68 ± 0.32		
Total log N	14.28 ± 0.06	13.77 ± 0.09	13.30 ± 0.14	13.12 ± 0.17

Table 4.6 Abundances of different elements in the $z = 4.809$ absorber toward J0824+1302

Element	[X/H]	[X/O]
O	-2.51 ± 0.16	
C	-2.75 ± 0.17	-0.24 ± 0.10
Si	-2.31 ± 0.20	0.20 ± 0.15
Fe	-2.48 ± 0.23	0.03 ± 0.18

Table 4.7 Results of Voigt profile fitting for different elements in the $z = 4.829$ absorber towards J0824+1302

z	log $N_{O\,I}$	log $N_{C\,II}$	log $N_{Si\,II}$	log $N_{Fe\,II}$
4.82802				
4.82908	15.44 ± 0.15	14.88 ± 0.12		
4.82891				13.82 ± 0.13
Total log N	15.44 ± 0.15	14.88 ± 0.12	14.22 ± 0.08	13.82 ± 0.13

Table 4.8 Abundances of different elements in the $z = 4.829$ absorber toward J0824+1302

Element	[X/H]	[X/O]
O	-2.05 ± 0.21	
C	-2.35 ± 0.19	-0.30 ± 0.19
Si	-2.09 ± 0.17	-0.04 ± 0.17
Fe	-2.48 ± 0.20	-0.43 ± 0.20

Table 4.9 Results of Voigt profile fitting for different elements in the absorber at z=4.859 toward J1233+0622.

z	b_{eff} (km s^{-1})	log $N_{O\,I}$	log $N_{C\,II}$	log $N_{Si\,II}$	log $N_{Fe\,II}$
4.85300	10.46	...	13.09 ± 0.21	13.61 ± 0.21	...
4.85388	10.46	...	13.19 ± 0.18	...	13.13 ± 0.20
4.85511	12.23	...	...	13.48 ± 0.23	...
4.85644	8.25	...	...	13.68 ± 0.24	...
4.85691	8.71	...	13.61 ± 0.10	...	13.44 ± 0.16
4.85795	18.12	> 15.30	14.42 ± 0.07	13.82 ± 0.19	...
4.85908	7.53	...	14.01 ± 0.14	...	...
4.85996	8.46	...	...	13.59 ± 0.24	...
4.86019	8.46	...	13.89 ± 0.11	...	...
4.86605	8.25	...	13.63 ± 0.11	...	...
Total log N	...	> 15.30	14.74 ± 0.05	14.35 ± 0.10	13.61 ± 0.13
AOD log N	...	...	14.65 ± 0.02	14.44 ± 1.16	13.68 ± 0.12

Table 4.10 Abundances of different elements in the $z = 4.859$ absorber toward J1233+0622

Element	[X/H]	[X/O]
O	> -2.14	
C	-2.44 ± 0.15	< -0.30
Si	-1.91 ± 0.18	< 0.23
Fe	-2.64 ± 0.20	< -0.50

Table 4.11 Results of Voigt profile fitting for different elements in the absorber at z=5.050 toward J1233+0622.

z	log $N_{O\,I}$	log $N_{C\,II}$	log $N_{Si\,II}$	log $N_{Fe\,II}$
5.04754	13.88 ± 0.18	13.89 ± 0.19	...	...
5.04912	13.79 ± 0.28	14.05 ± 0.14	...	...
5.05024	15.11 ± 0.12	14.75 ± 0.16	14.19 ± 0.11	14.07 ± 0.09
5.05188	13.88 ± 0.19	13.84 ± 0.19	13.69 ± 0.17	...
5.05290	13.76 ± 0.20	13.49 ± 0.23	...	...
Total log N	15.19 ± 0.10	14.93 ± 0.11	14.31 ± 0.09	14.07 ± 0.09
AOD log N	15.11 ± 0.41	14.80 ± 0.05	14.27 ± 0.05	14.14 ± 0.05

Table 4.12 Abundances of different elements in the $z = 5.050$ absorber toward J1233+0622

Element	[X/H]	[X/O]
O	-1.60 ± 0.18	
C	-1.60 ± 0.19	0.00 ± 0.20
Si	-1.30 ± 0.18	0.30 ± 0.20
Fe	-1.53 ± 0.17	0.07 ± 0.14

Table 4.13 Results of Voigt profile fitting for different elements in the absorber at z=4.589 toward J1253+1046.

z	log $N_{O\,I}$	log $N_{C\,II}$	log $N_{Si\,II}$	log $N_{Fe\,II}$
4.58859	13.84 ± 0.08	...	...	13.98 ± 0.14
4.58916	...	...	...	13.89 ± 0.17
4.58948	14.94 ± 0.10	14.34 ± 0.22	13.67 ± 0.09	...
4.59014	13.86 ± 0.07	...	...	...
Total log N	15.00 ± 0.08	14.34 ± 0.22	13.67 ± 0.09	14.24 ± 0.11
AOD log N	14.78 ± 0.27	14.29 ± 0.38	13.88 ± 0.04	14.28 ± 0.06

Table 4.14 Abundances of different elements in the $z = 4.589$ absorber toward J1253+1046

Element	[X/H]	[X/O]
O	-1.43 ± 0.17	
C	-1.84 ± 0.27	-0.41 ± 0.24
Si	-1.59 ± 0.17	-0.16 ± 0.12
Fe	-1.01 ± 0.18	0.42 ± 0.14

Table 4.15 Results of Voigt profile fitting for different elements in the absorber at z=4.600 toward J1253+1046.

z	log $N_{O\,I}$	log $N_{C\,II}$	log $N_{Si\,II}$	log $N_{Fe\,II}$
4.59845	14.32 ± 0.12	...	...	...
4.59940	...	...	...	14.06 ± 0.29
4.60003	15.53 ± 0.08	14.78 ± 0.20	14.57 ± 0.05	...
4.60194	14.32 ± 0.09	...	...	...
Total log N	> 15.58	> 14.78	14.57 ± 0.05	14.06 ± 0.29
AOD log N	15.31 ± 0.06	14.78 ± 0.45	14.56 ± 0.01	14.26 ± 0.05

Table 4.16 Abundances of different elements in the $z = 4.600$ absorber toward J1253+1046

Element	[X/H]	[X/O]
O	> -1.46	...
C	> -2.0	...
Si	-1.29 ± 0.16	< 0.17
Fe	-1.79 ± 0.33	< -0.33

Table 4.17 Results of Voigt profile fitting for different elements in the absorber at z=4.793 toward J1253+1046.

z	log $N_{O\,I}$	log $N_{C\,II}$	log $N_{Si\,II}$	log $N_{Fe\,II}$	log $N_{S\,II}$
4.79347	> 14.71	14.21 ± 0.17	14.15 ± 0.18	...	14.18 ± 0.17
AOD log N	14.56 ± 0.12	14.22 ± 0.07	14.08 ± 0.07	...	14.25 ± 0.04

Table 4.18 Abundances of different elements in the $z = 4.793$ absorber toward J1253+1046

Element	[X/H]	[X/O]
O	> -1.63	
C	-1.87 ± 0.20	< -0.24
Si	-1.01 ± 0.21	< 0.62
S	-0.59 ± 0.20	...

Table 4.19 Results of Voigt profile fitting for different elements in the absorber at z=4.627 toward J1557+1018.

z	b_{eff} (km s^{-1})	log $N_{O\,I}$	log $N_{C\,II}$	log $N_{Si\,II}$
4.62512	10.76	14.54 ± 0.11	14.38 ± 0.15	13.65 ± 0.06
4.62694	35.53	15.64 ± 0.09	15.52 ± 0.11	15.00 ± 0.04
4.62885	38.41	15.55 ± 0.19	15.10 ± 0.21	14.74 ± 0.04
4.63018	14.29	15.01 ± 0.19	14.53 ± 0.19	14.35 ± 0.09
Total log N	...	> 15.97	> 15.71	> 15.26
AOD log N	...	15.64 ± 0.62	15.23 ± 0.11	15.26 ± 0.84

Table 4.20 Abundances of different elements in the $z = 4.627$ absorber toward J1557+1018

Element	[X/H]
O	> -1.47
C	> -1.47
Si	> -1.0

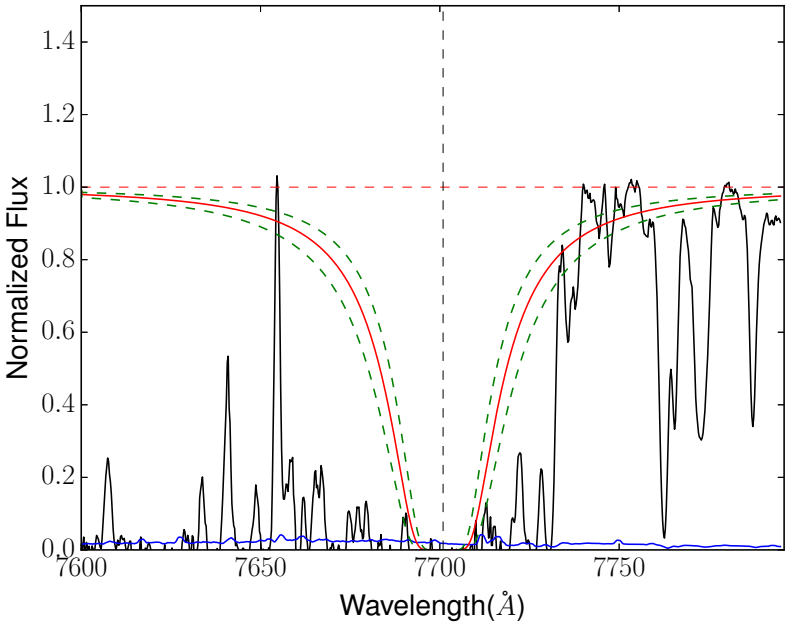

Figure 4.1 Voigt profile fitting for hydrogen Lyman$-\alpha$ for the $z = 5.335$ absorber toward J0231-0728. The observed normalized flux is shown in black and the fitted profile for log $N_{H\,I} = 20.10$ is shown in red. The green dashed lines above and below the fitted profile represent ± 0.15 dex uncertainty. The 1σ error in the normalized spectrum is shown in blue at the bottom. The vertical dashed line represents the centre of the profile and the horizontal dashed line in red shows the continuum level.

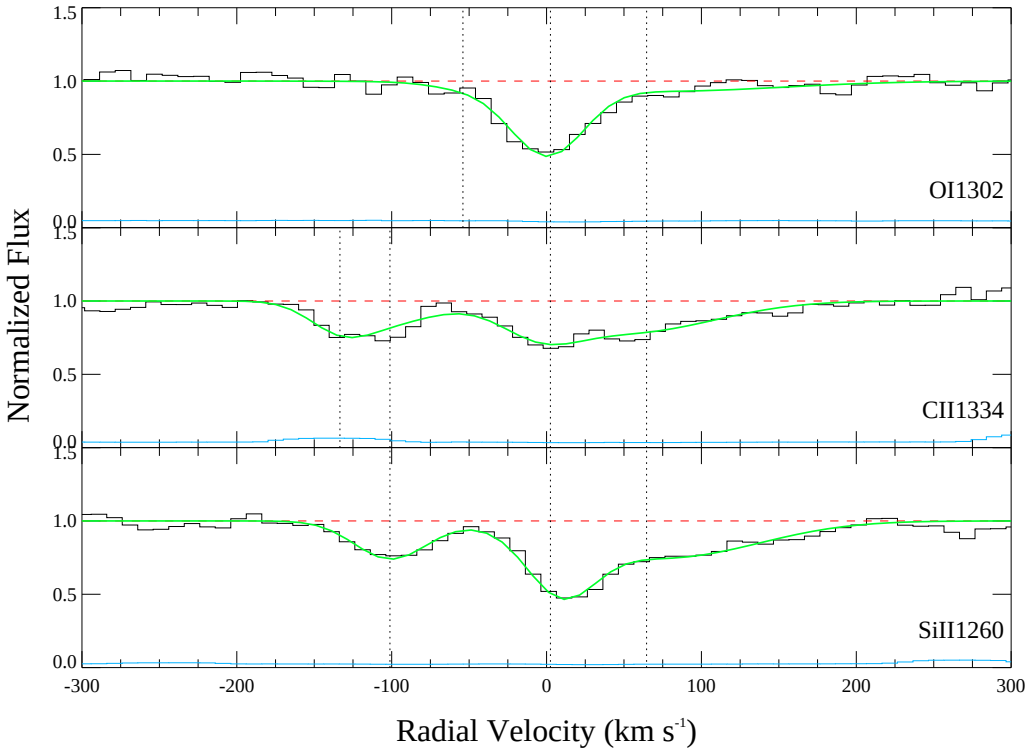

Figure 4.2 Velocity plots for metal lines in the $z = 5.335$ absorber toward J0231-0728. In each panel, the data are shown in black and the fitted profiles are shown in green. The blue line at the bottom show the 1σ error in the normalized flux and the horizontal line in red represents the continuum level. The vertical dotted lines show the different velocity components included in the profile fits.

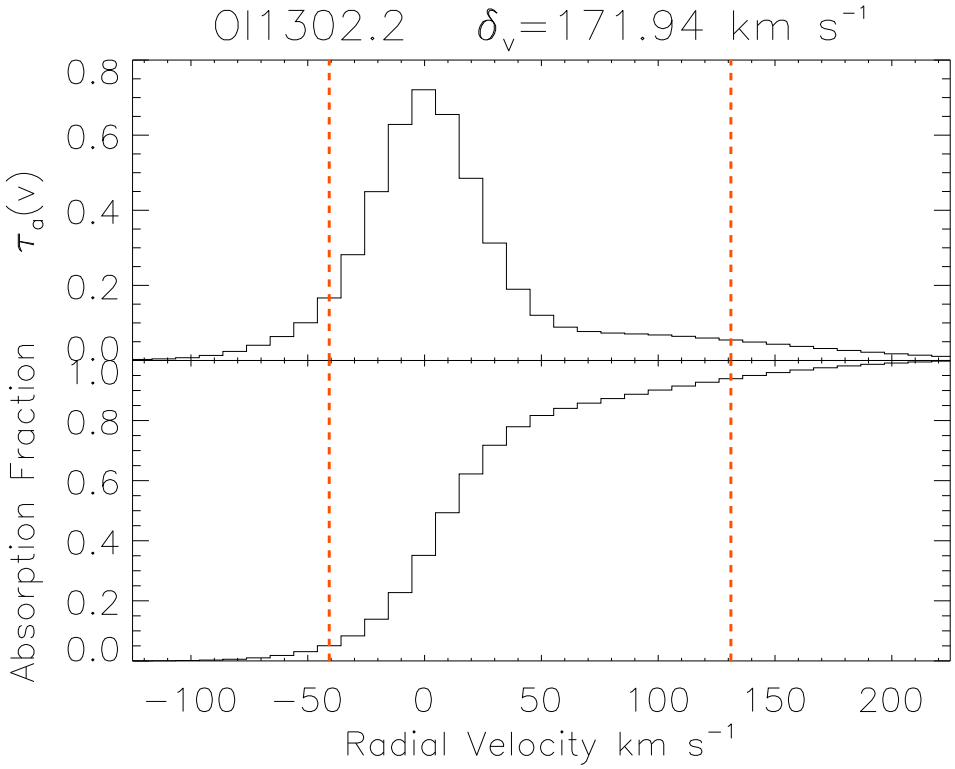

Figure 4.3 Velocity dispersion for O I λ1302 line in $z = 5.335$ absorber toward J0231-0728 based on our Voigt profile fits. The upper panel shows the optical depth profile and the lower panel shows the absorption fraction as a function of radial velocity. The 5 percent and 95 percent levels of the absorption are marked with two vertical dotted lines in red.

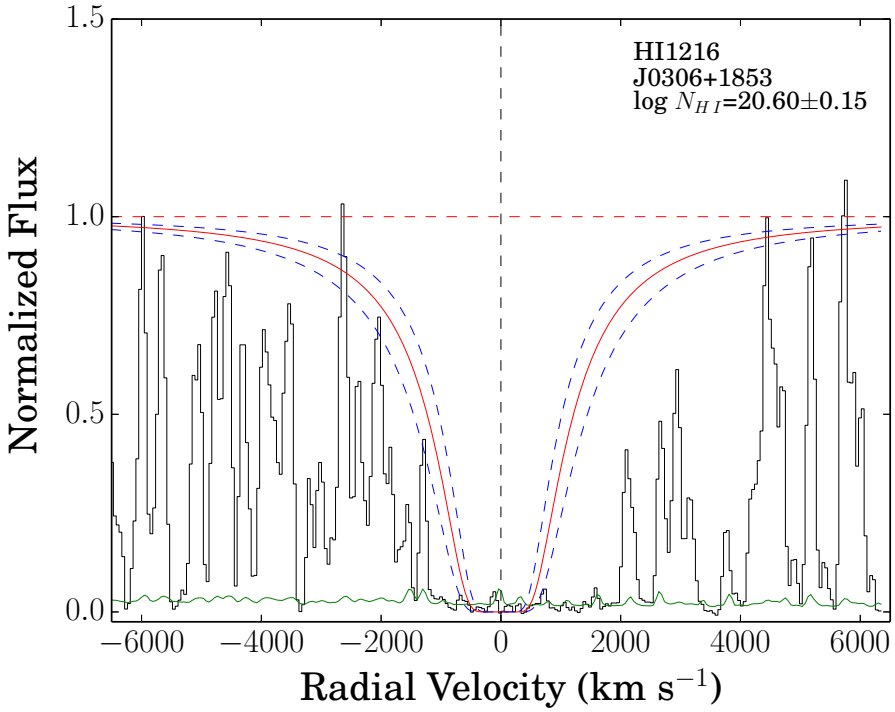

Figure 4.4 Voigt profile fitting for hydrogen Lyman$-\alpha$ for the $z = 4.987$ absorber toward J0306+1853. The observed normalized flux is shown in black and the fitted profile for log $N_{H\,I} = 20.60$ is shown in red. The green dashed lines above and below the fitted profile represent ± 0.15 dex uncertainty. The 1σ error in the normalized spectrum is shown in blue at the bottom. The vertical dashed line represents the centre of the profile and the horizontal dashed line in red shows the continuum level.

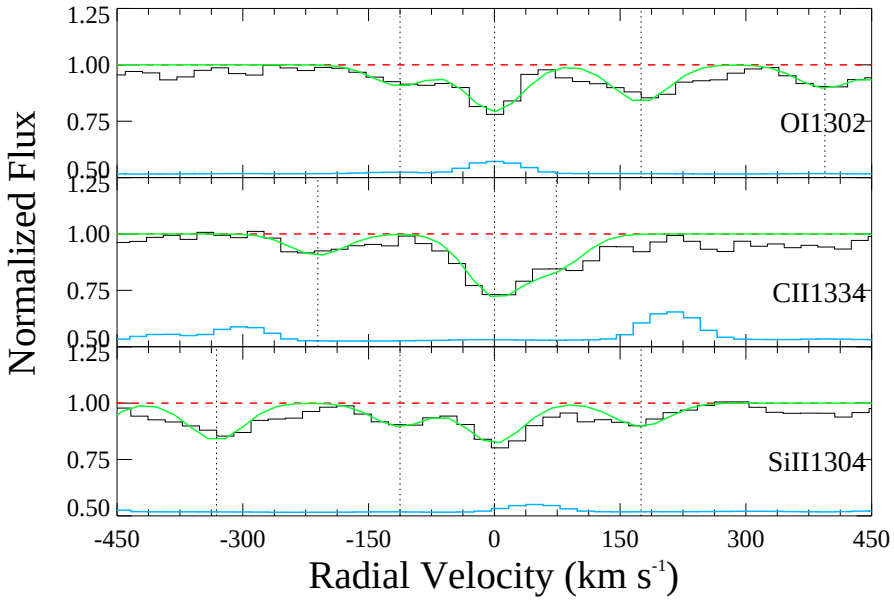

Figure 4.5 Velocity plots for metal lines for the absorber at $z = 4.987$ in the sight line to J0306+1853 from the MagE spectrograph. In each panel, the observed data are shown in black and the fitted profiles are shown in green. The blue line at the bottom of each panel shows the 1σ error in the normalized flux and is shifted by +0.5. The placement of continuum is shown by the horizontal dashed red line. The vertical dotted lines show the different velocity components included in the profile fits. It is to be noted that the rightmost vertical dotted line in O I λ1302 is attributed to Si II absorption and the leftmost vertical dotted line in Si II λ1304 is attributed to O I absorption.

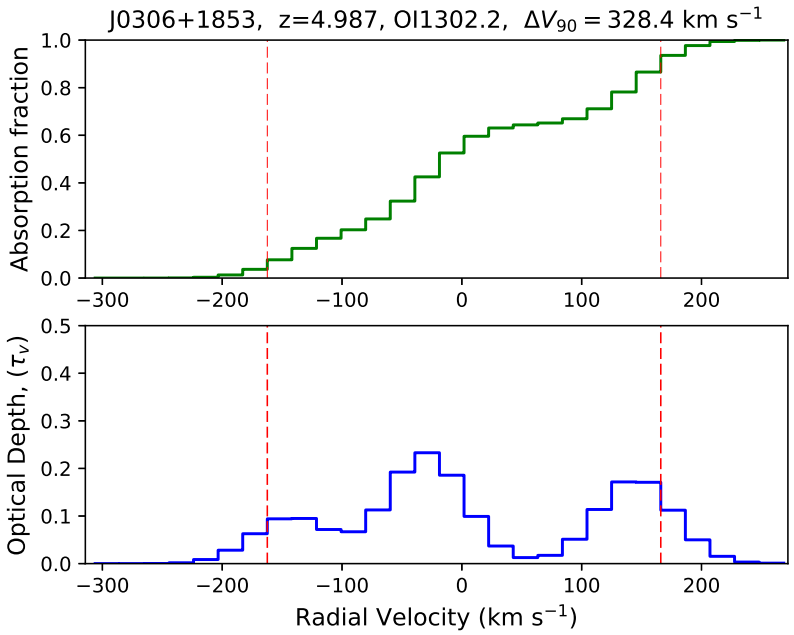

Figure 4.6 Same as Fig. 4.3 but for O I λ1302 line in $z = 4.987$ absorber toward J0306+1853 based on our Voigt profile fits.

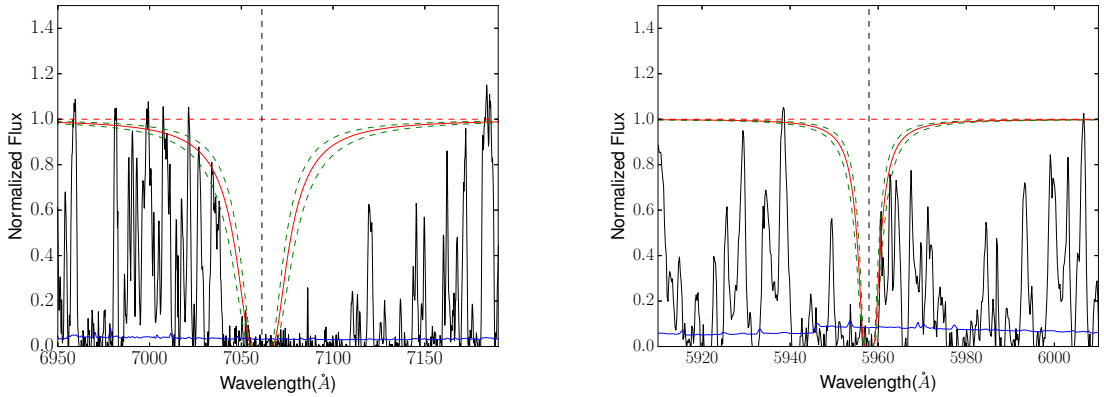

Figure 4.7 Voigt profile fitting for hydrogen Lyman$-\alpha$ (Left) and hydrogen Lyman$-\beta$ (Right) for the $z = 4.809$ absorber toward J0824+1302. Observed normalized flux is shown in black and the fitted profile for log $N_{H\,I} = 20.10$ is shown in red. Two green dashed lines above and below the fitted profile represent ± 0.15 dex uncertainty. The 1σ error in the normalized spectrum is shown in blue at the bottom. In each panel, the vertical dashed line represents the centre of the profile, and the horizontal dashed line in red shows the continuum level.

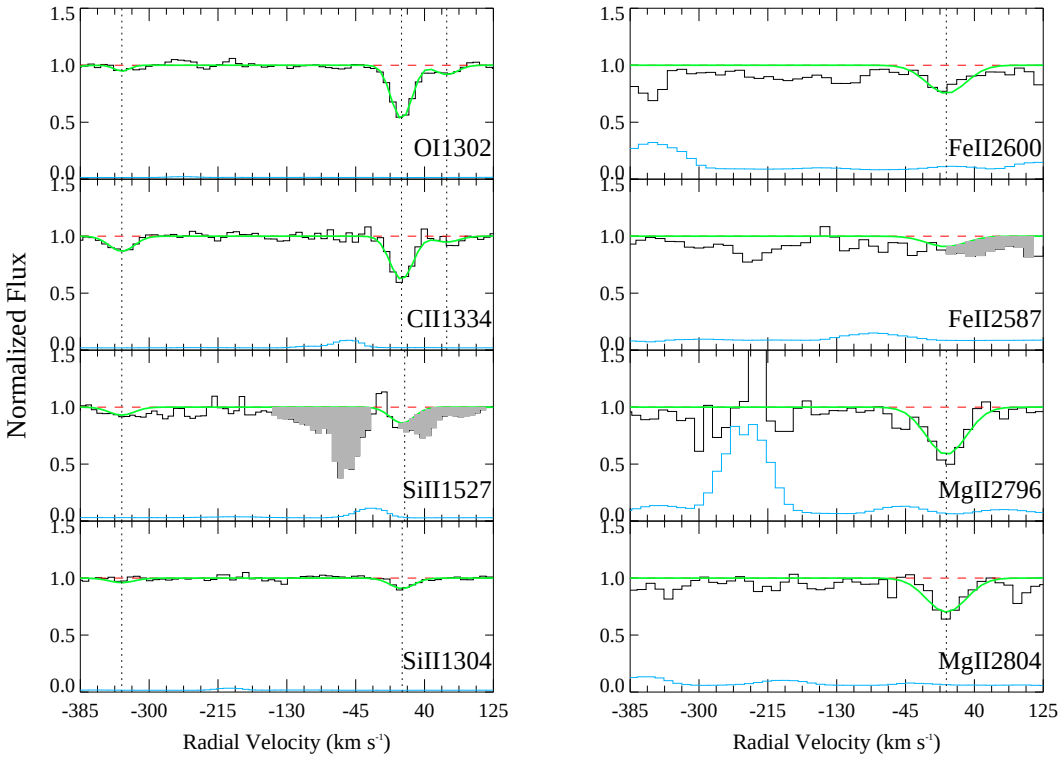

Figure 4.8 Velocity plots for metal lines for the absorber at $z = 4.809$ toward J0824+1302. In each panel, the data are shown in black and the fitted profiles are shown in green. The blue line at the bottom shows the 1σ error in normalized flux and the horizontal line in red represents the continuum level. Unrelated absorption features are shaded in grey. In each panel, the vertical dotted lines show the different velocity components included in the profile fits.

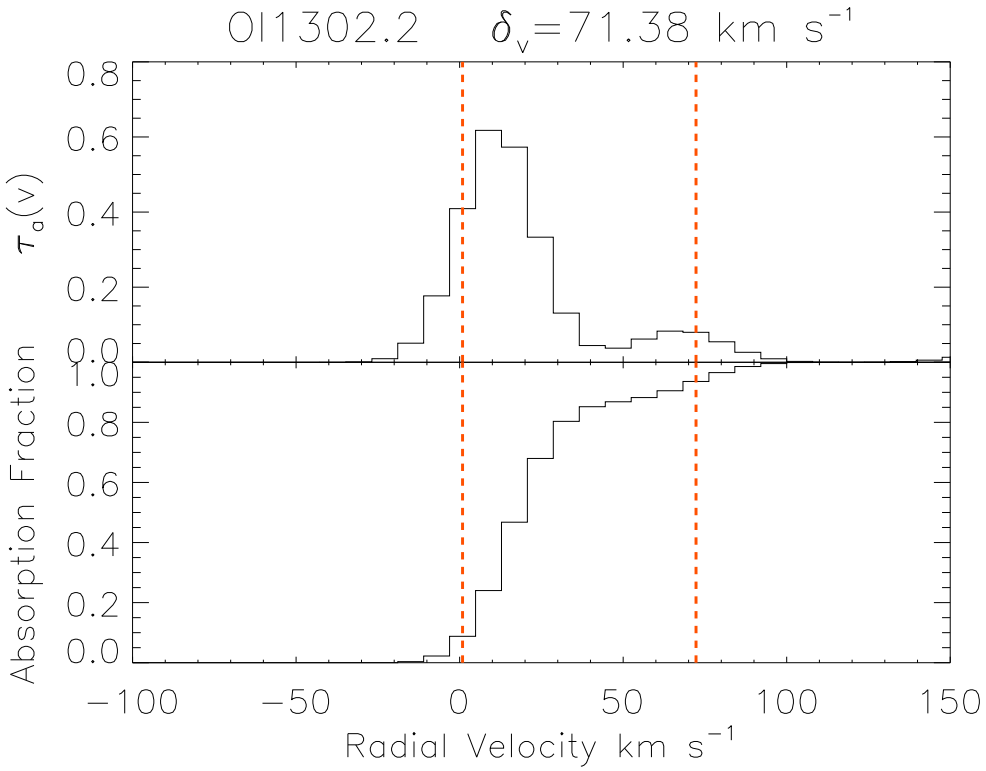

Figure 4.9 Same as Fig. 4.3 but for O I λ1302 line in $z = 4.809$ absorber toward J0824+1302 based on our Voigt profile fits.

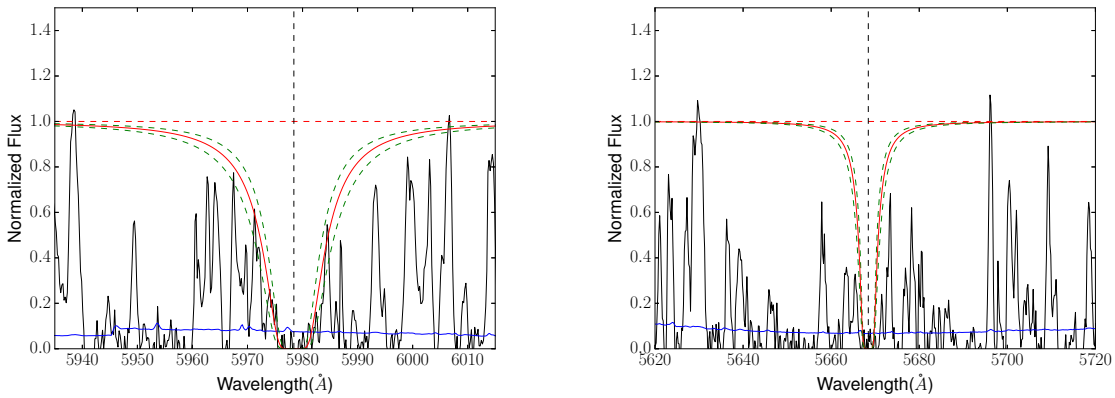

Figure 4.10 Voigt profile fitting for hydrogen Lyman$-\beta$ (Left) and hydrogen Lyman$-\gamma$ (Right) for the $z = 4.829$ absorber toward J0824+1302. Observed normalized flux is shown in black and the fitted profile for log $N_{HI} = 20.80$ is shown in red. Two green dashed lines above and below the fitted profile represent ± 0.15 dex uncertainty. The 1σ error in the normalized spectrum is shown in blue at the bottom. In each panel, the vertical dashed line represents the centre of the profile, and the horizontal dashed line in red shows the continuum level.

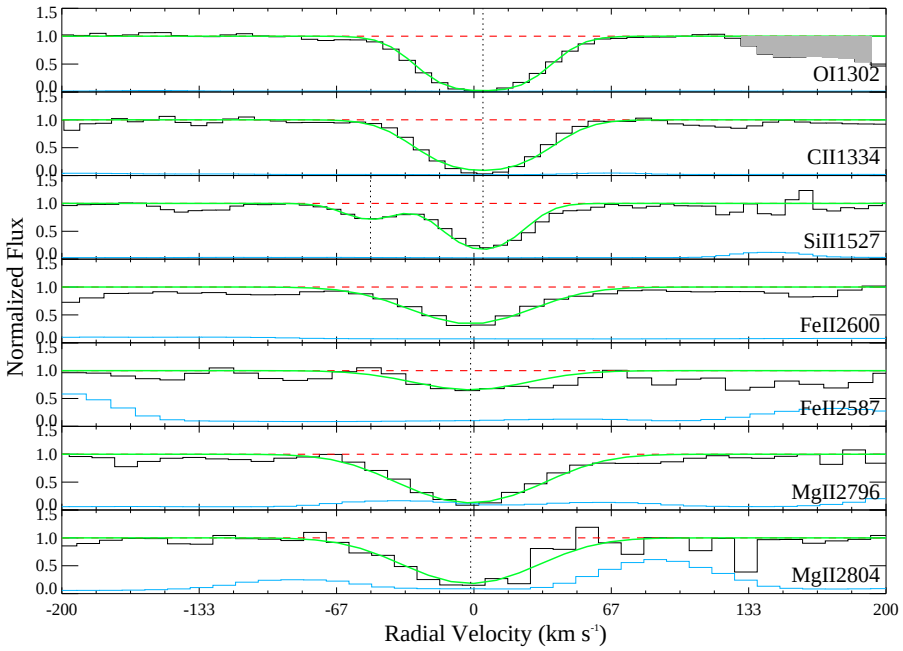

Figure 4.11 Velocity plots for metal lines for the absorber at $z = 4.829$ toward J0824+1302. In each panel, the data are shown in black and the fitted profiles are shown in green. The blue line at the bottom of each panel shows the 1σ error in the normalized flux and the horizontal line in red represents the continuum level. Unrelated absorption features are shaded in grey. The vertical dotted lines show the different velocity components included in the profile fits.

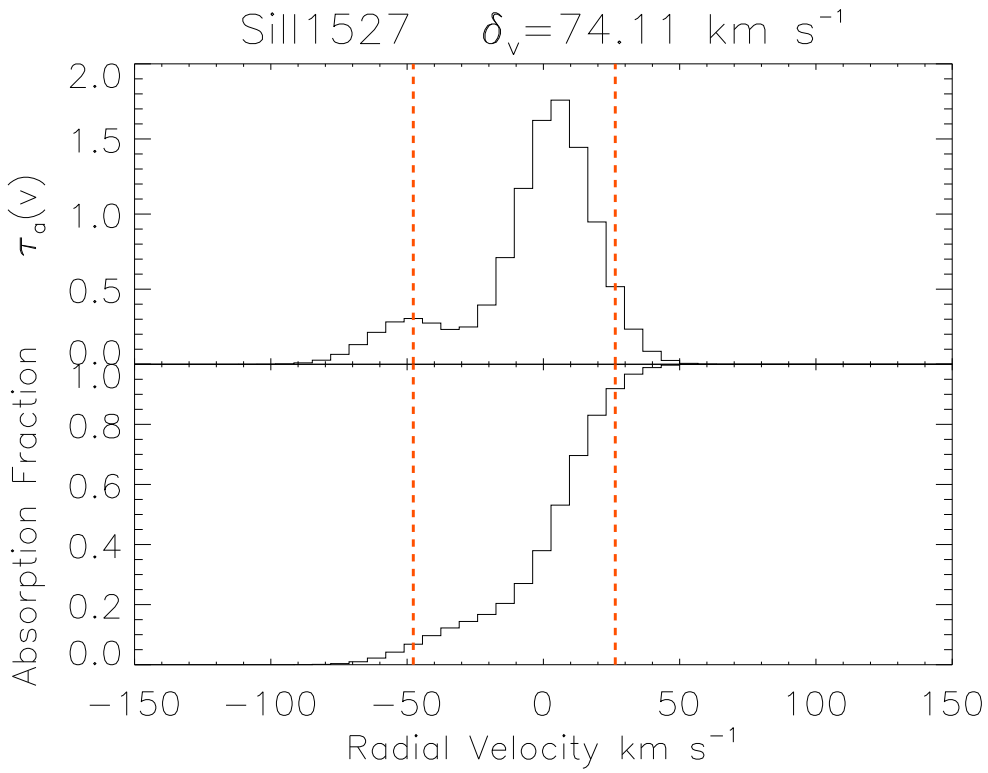

Figure 4.12 Same as Fig. 4.3 but for Si II λ1527 line in $z = 4.829$ absorber toward J0824+1302 based on our Voigt profile fits.

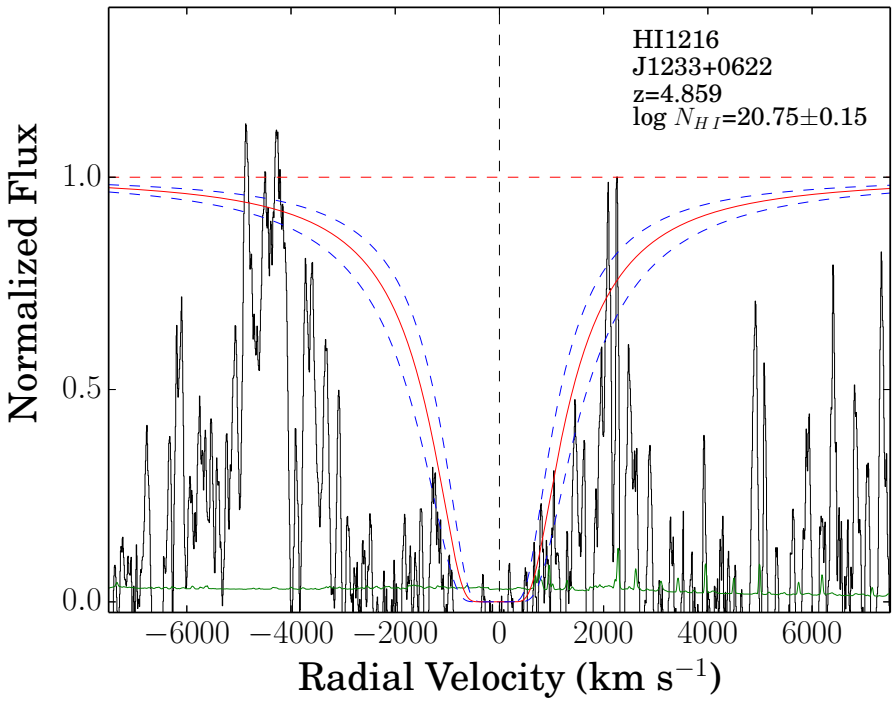

Figure 4.13 Voigt profile fitting for hydrogen Lyman$-\alpha$ for the $z = 4.859$ absorber toward J1233+0622. The observed normalized flux is shown in black and the fitted profile for log $N_{H\,I} = 20.75$ is shown in red. The green dashed lines above and below the fitted profile represent ± 0.15 dex uncertainty. The 1σ error in the normalized spectrum is shown in blue at the bottom. The vertical dashed line represents the centre of the profile and the horizontal dashed line in red shows the continuum level.

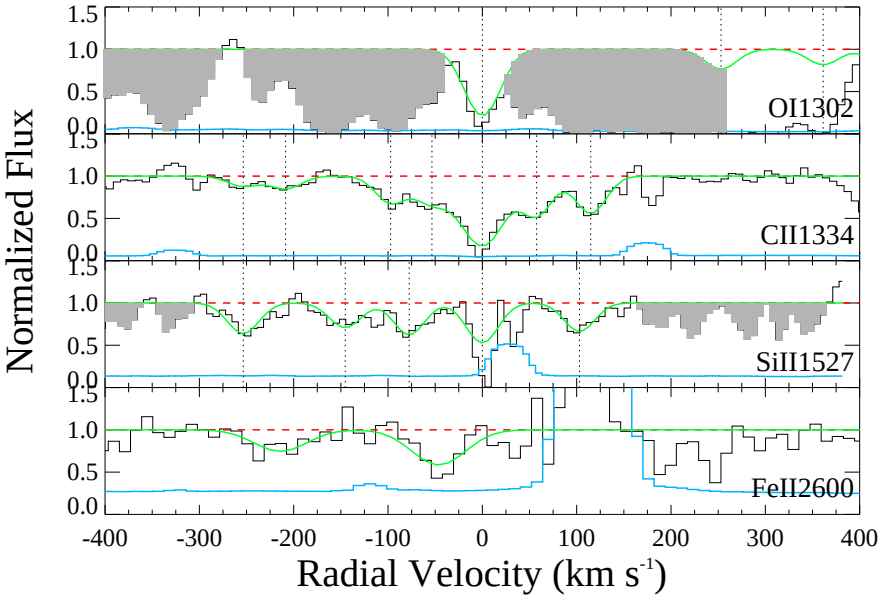

Figure 4.14 Velocity plots for metal lines for the absorber at $z = 4.859$ in the sight line to J1233+0622 from the X-Shooter spectrograph. In each panel, the observed data are shown in black and the fitted profiles are shown in green. The blue line at the bottom of each panel shows the 1σ error in the normalized flux and the placement of continuum is shown by the horizontal dashed red line. The vertical dotted lines show the different velocity components included in the profile fits. The shaded regions are the telluric and unrelated absorption features.

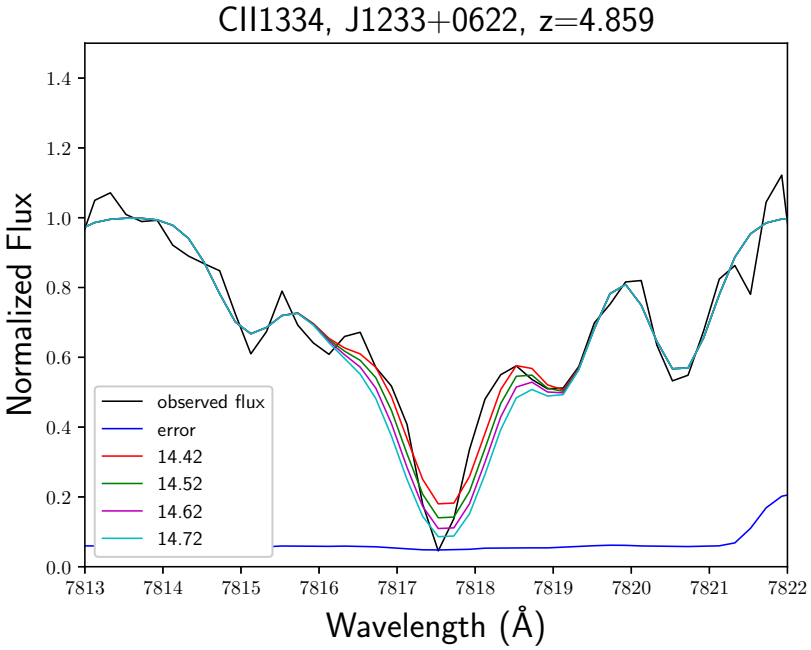

Figure 4.15 Overplotting of different column density profiles to estimate the extent of saturation. The observed continuum normalized flux is shown in black and the 1σ error in the normalized flux is shown in blue at the bottom. The metal line, sightline to the quasar, and redshift are given at the top of the figure. See the text for the details.

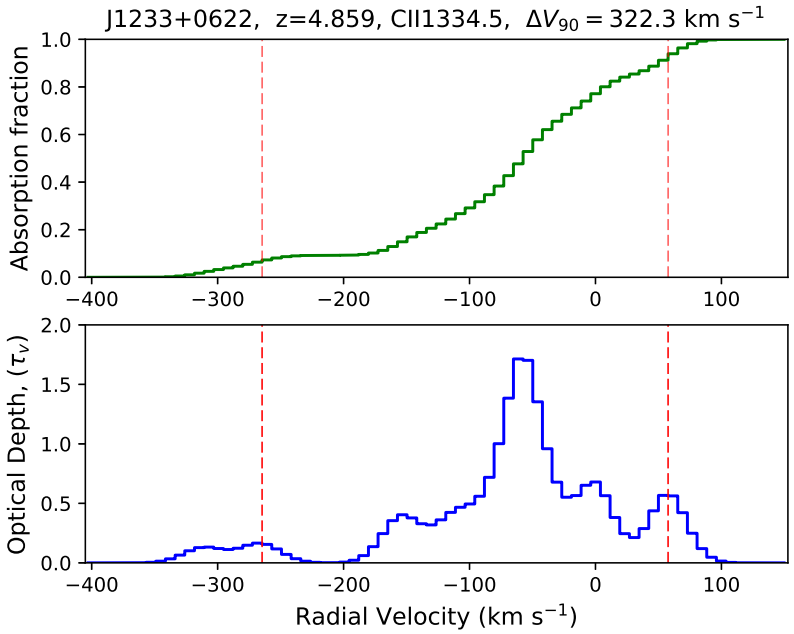

Figure 4.16 Same as Fig. 4.3 but for C II λ1334 line in $z = 4.859$ absorber toward J1233+0622 based on our Voigt profile fits.

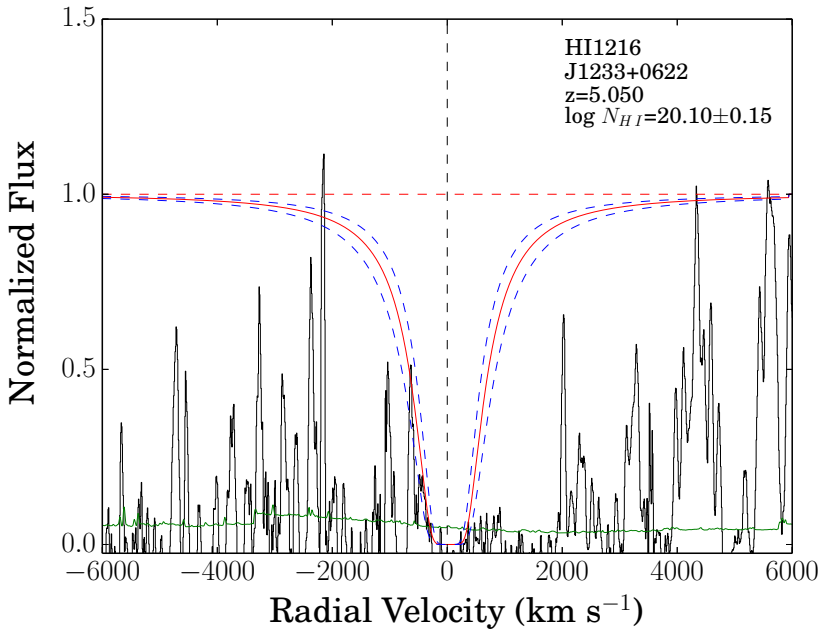

Figure 4.17 Voigt profile fitting for hydrogen Lyman$-\alpha$ for the $z = 5.050$ absorber toward J1233+0622. The observed normalized flux is shown in black and the fitted profile for log $N_{H\,I} = 20.10$ is shown in red. The green dashed lines above and below the fitted profile represent ± 0.15 dex uncertainty. The 1σ error in the normalized spectrum is shown in blue at the bottom. The vertical dashed line represents the centre of the profile and the horizontal dashed line in red shows the continuum level.

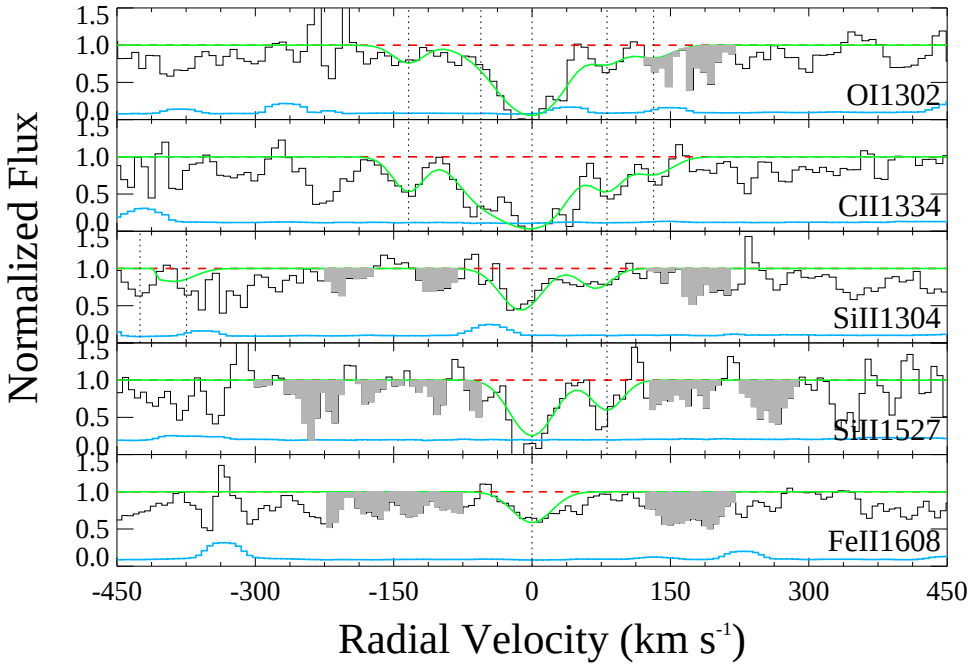

Figure 4.18 Same as Fig. 4.14 but for the absorber at $z = 5.050$ in the sight line to J1233+0622. Unrelated absorption features are shaded in grey.

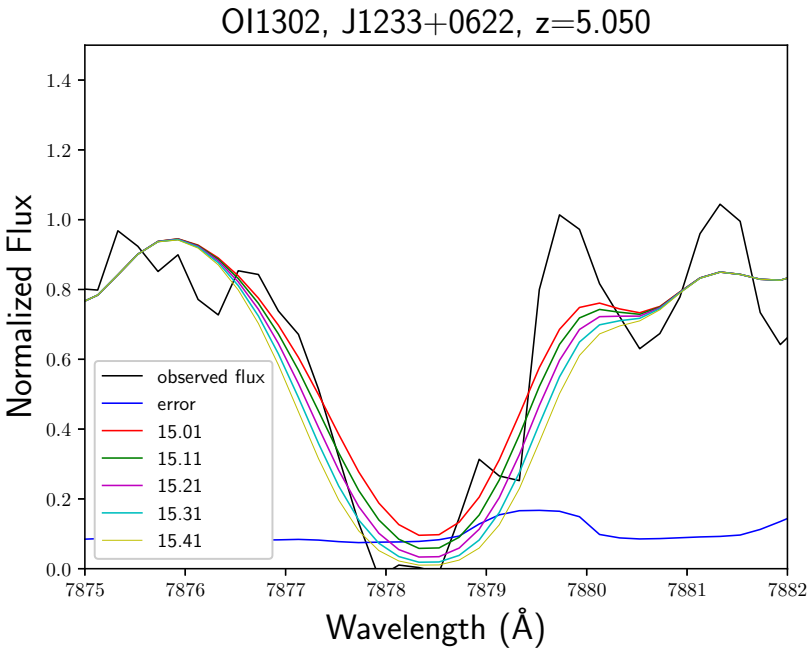

Figure 4.19 Same as Fig. 4.15.

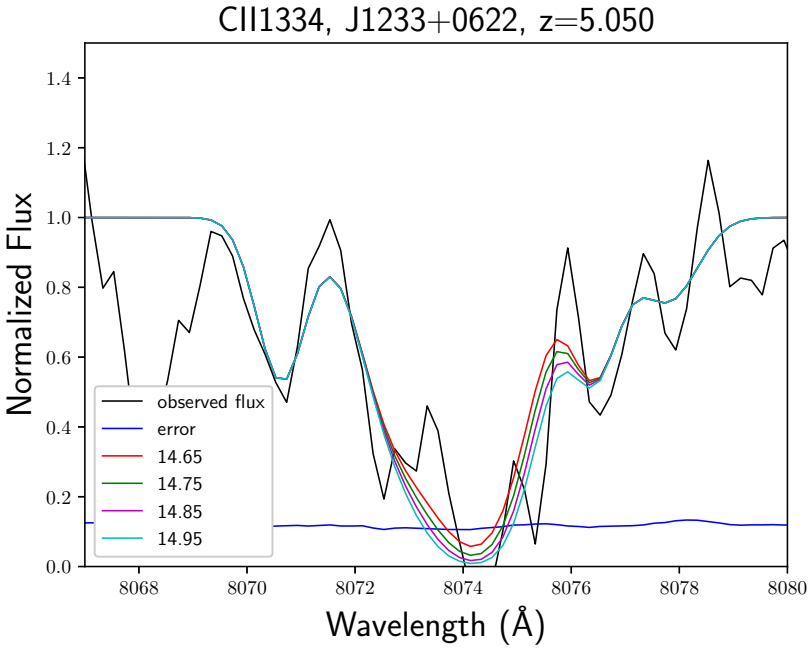

Figure 4.20 Same as Fig. 4.15.

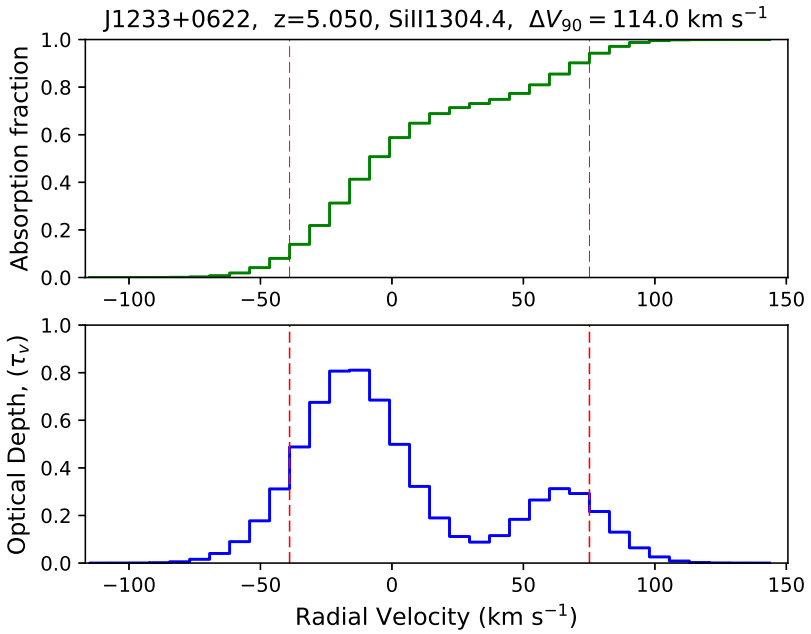

Figure 4.21 Same as Fig.4.3 but for Si II λ1304 line in $z = 5.050$ absorber toward J1233+0622 based on our Voigt profile fits.

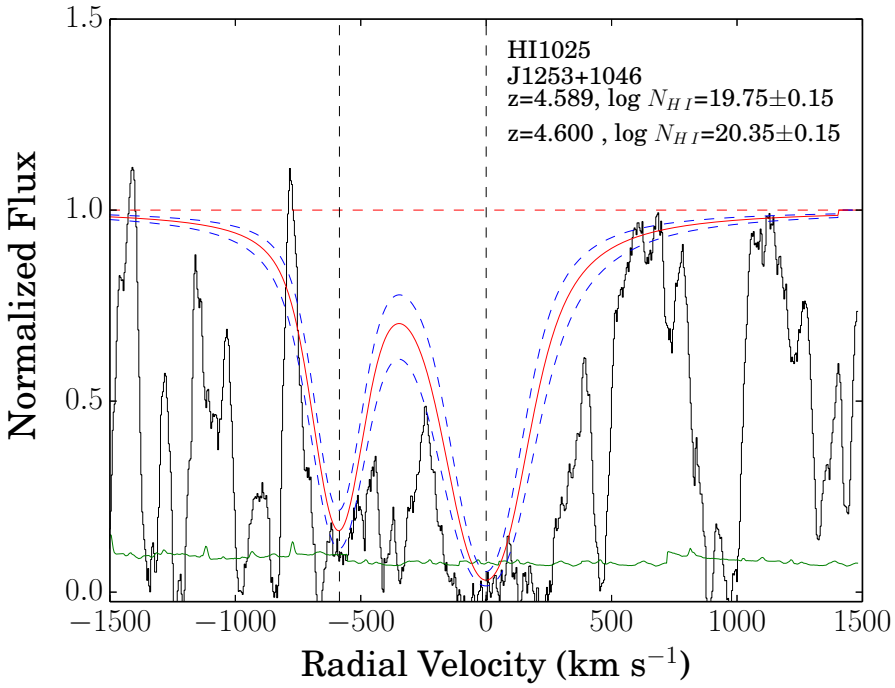

Figure 4.22 Voigt profile fitting for hydrogen Lyman$-\beta$ for the z=4.589, 4.600 absorbers toward J1253+1046. The observed normalized flux is shown in black and the fitted profiles for log $N_{H\,I} = 19.75, 20.35$ for the absorbers at z=4.589 and 4.600, respectively are shown in red. The green dashed lines above and below the fitted profile represent ±0.15 dex uncertainty. The 1σ error in the normalized spectrum is shown in blue at the bottom. The vertical dashed line represents the centre of the profile and the horizontal dashed line in red shows the continuum level.

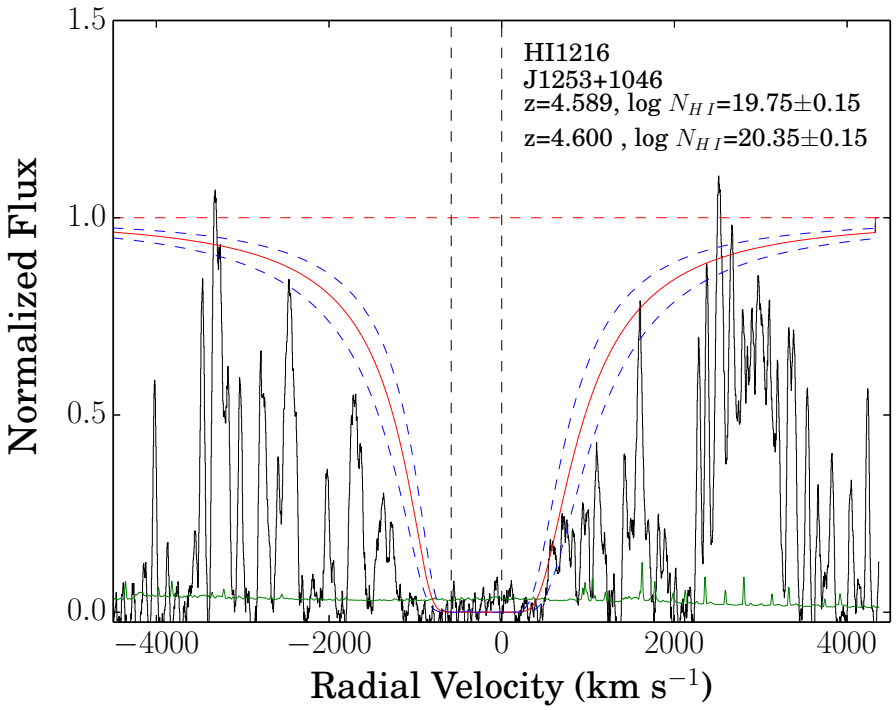

Figure 4.23 Voigt profile fitting for hydrogen Lyman$-\alpha$ for the z=4.589, 4.600 absorbers toward J1253+1046. The observed normalized flux is shown in black and the fitted profiles for log $N_{H\,I} = 19.75, 20.35$ for the absorbers at z=4.589 and 4.600, respectively are shown in red. The green dashed lines above and below the fitted profile represent ± 0.15 dex uncertainty. The 1σ error in the normalized spectrum is shown in blue at the bottom. The vertical dashed line represents the centre of the profile and the horizontal dashed line in red shows the continuum level.

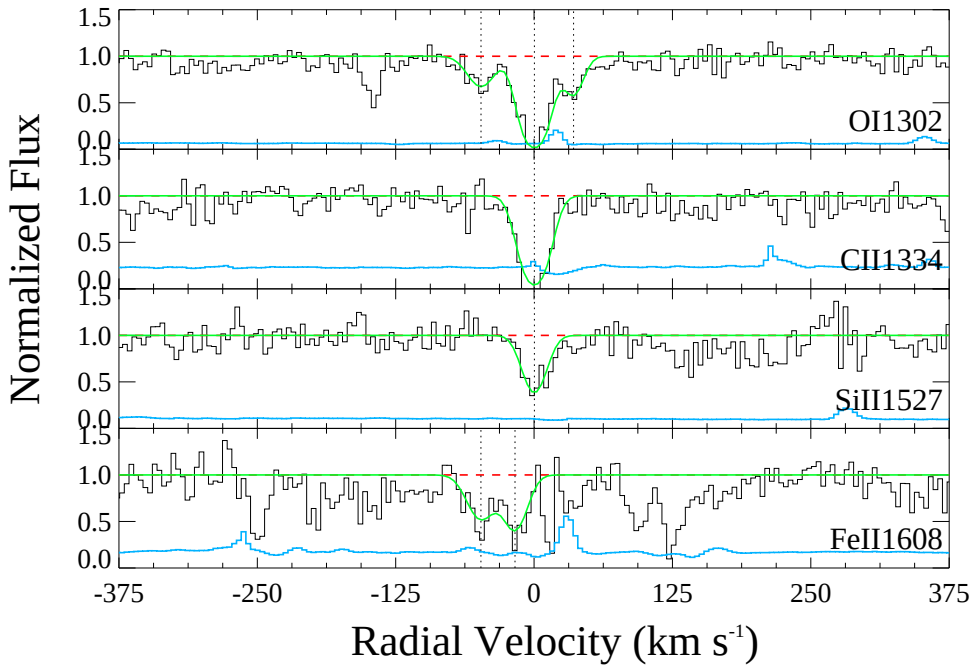

Figure 4.24 Velocity plots for metal lines for the absorber at $z = 4.589$ in the sight line to J1253+1046 from the MIKE spectrograph. In each panel, the observed data are shown in black and the fitted profiles are shown in green. The blue line at the bottom of each panel shows the 1σ error in the normalized flux and the placement of continuum is shown by the horizontal dashed red line. The vertical dotted lines show the different velocity components included in the profile fits.

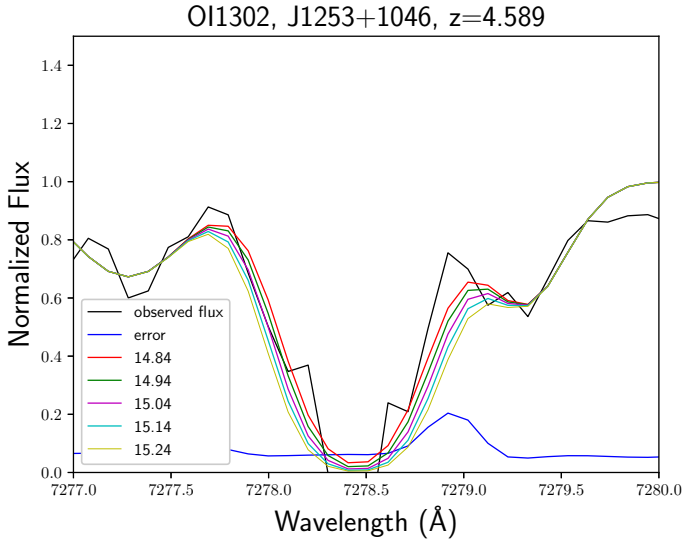

Figure 4.25 Same as Fig. 4.15.

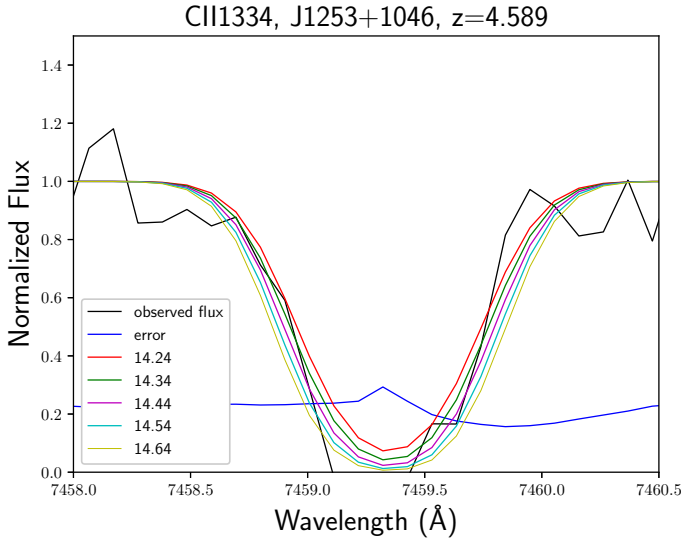

Figure 4.26 Same as Fig. 4.15.

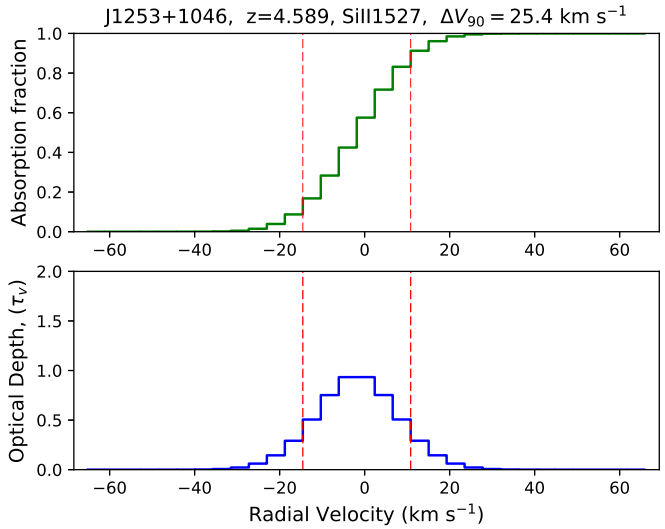

Figure 4.27 Same as Fig. 4.3 but for Si II λ1527 line in $z = 4.589$ absorber toward J1253+1046 based on our Voigt profile fits.

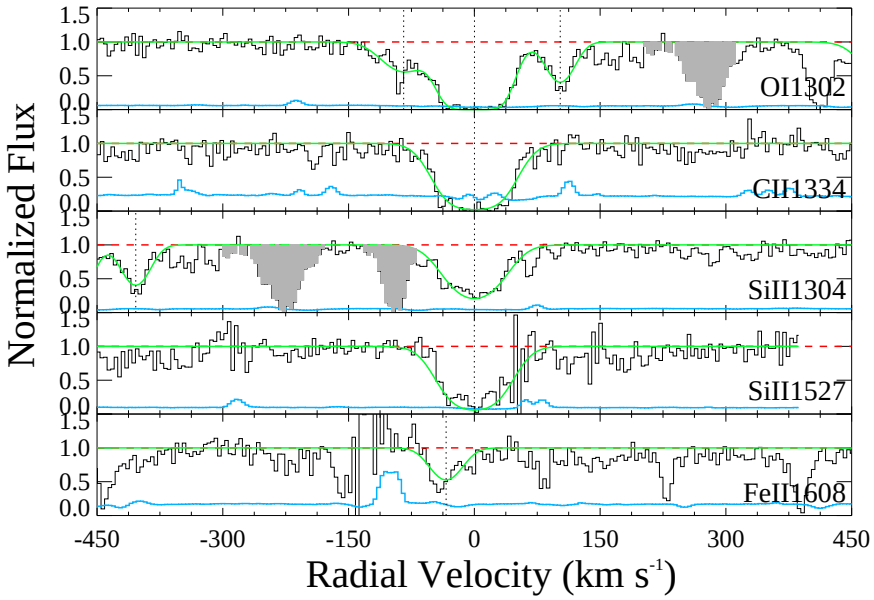

Figure 4.28 Same as Fig. 4.24 but for the absorber at $z = 4.600$ in the sight line to J1253+1046. The shaded regions are unrelated absorption features.

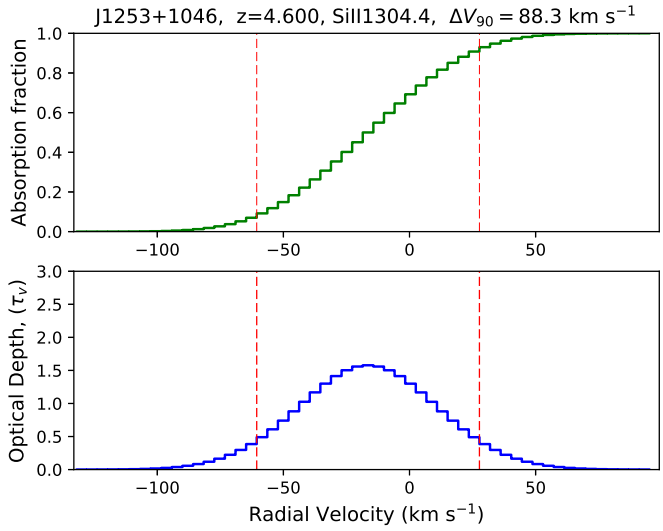

Figure 4.29 Same as Fig.4.3 but for Si II λ1304 line in $z = 4.600$ absorber toward J1253+1046 based on our Voigt profile fits.

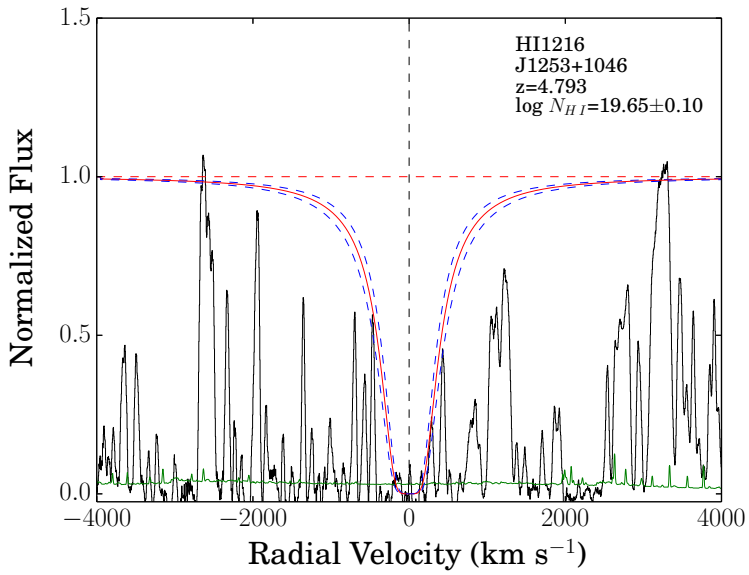

Figure 4.30 Voigt profile fitting for hydrogen Lyman$-\alpha$ for the z=4.793 absorber toward J1253+1046. The observed normalized flux is shown in black and the fitted profile for log $N_{H\,I} = 19.65$ is shown in red. The green dashed lines above and below the fitted profile represent ± 0.10 dex uncertainty. The 1σ error in the normalized spectrum is shown in blue at the bottom. The vertical dashed line represents the centre of the profile and the horizontal dashed line in red shows the continuum level.

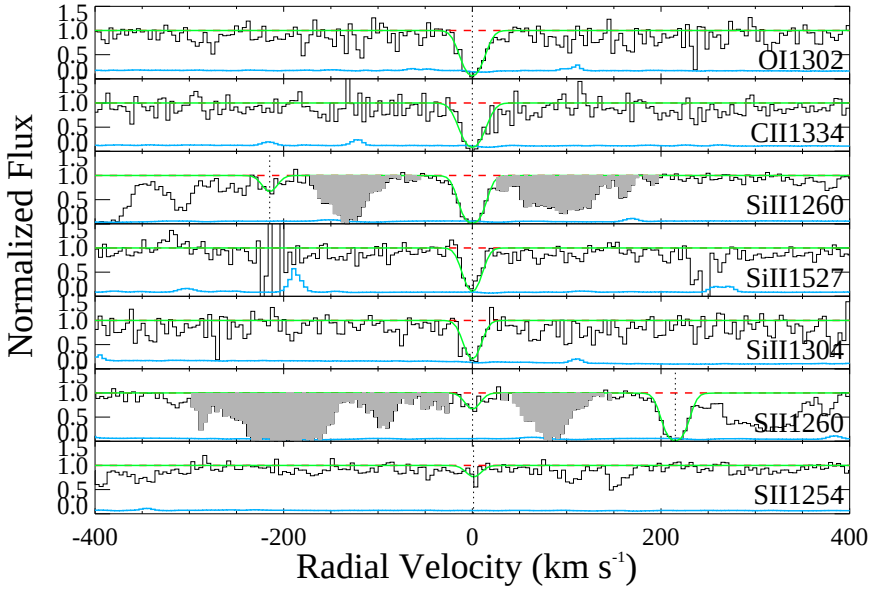

Figure 4.31 Same as Fig. 4.24 but for the absorber at $z = 4.793$ in the sight line to J1253+1046. The shaded regions are unrelated absorption features.

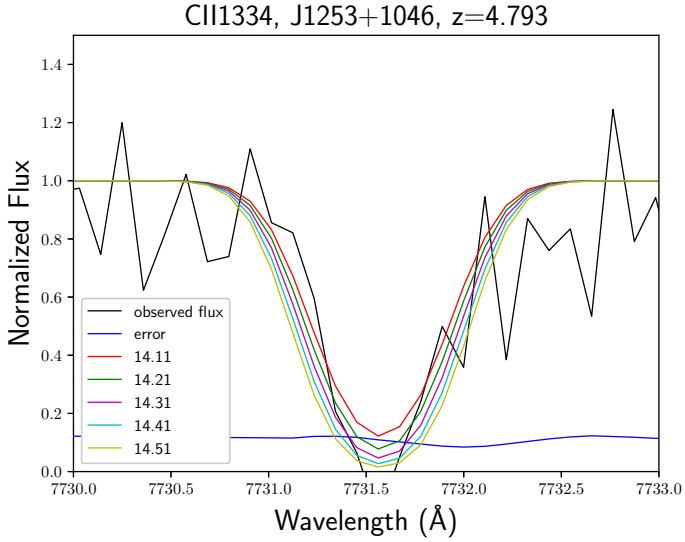

Figure 4.32 Same as Fig.4.15.

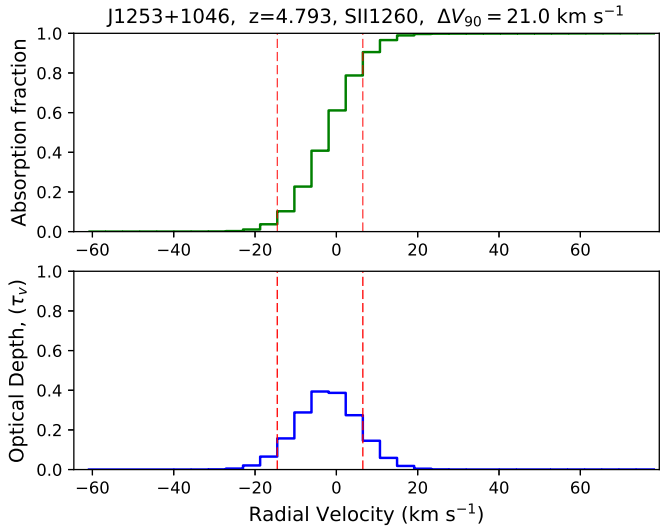

Figure 4.33 Same as Fig. 4.3 but for S II λ1260 line in $z = 4.793$ absorber toward J1253+1046 based on our Voigt profile fits.

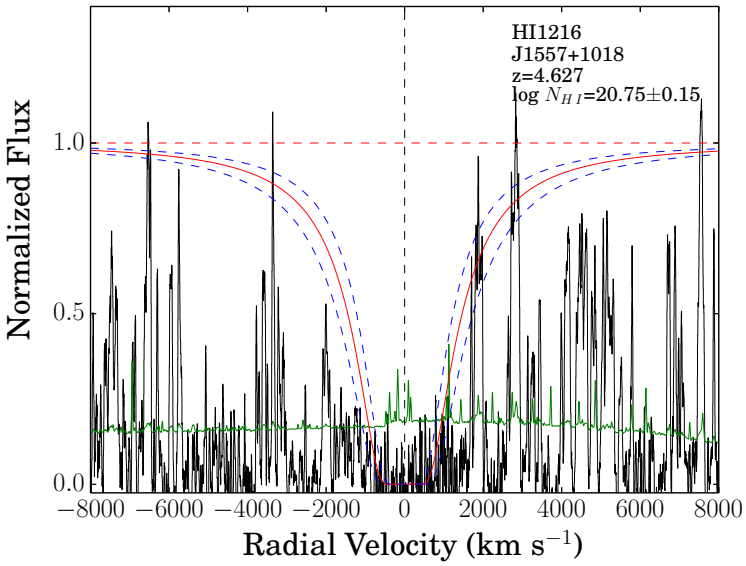

Figure 4.34 Voigt profile fitting for hydrogen Lyman$-\alpha$ for the z=4.627 absorber toward J1557+1018. The observed normalized flux is shown in black and the fitted profile for log $N_{H\,I} = 20.75$ is shown in red. The green dashed lines above and below the fitted profile represent ± 0.15 dex uncertainty. The 1σ error in the normalized spectrum is shown in blue at the bottom. The vertical dashed line represents the centre of the profile and the horizontal dashed line in red shows the continuum level.

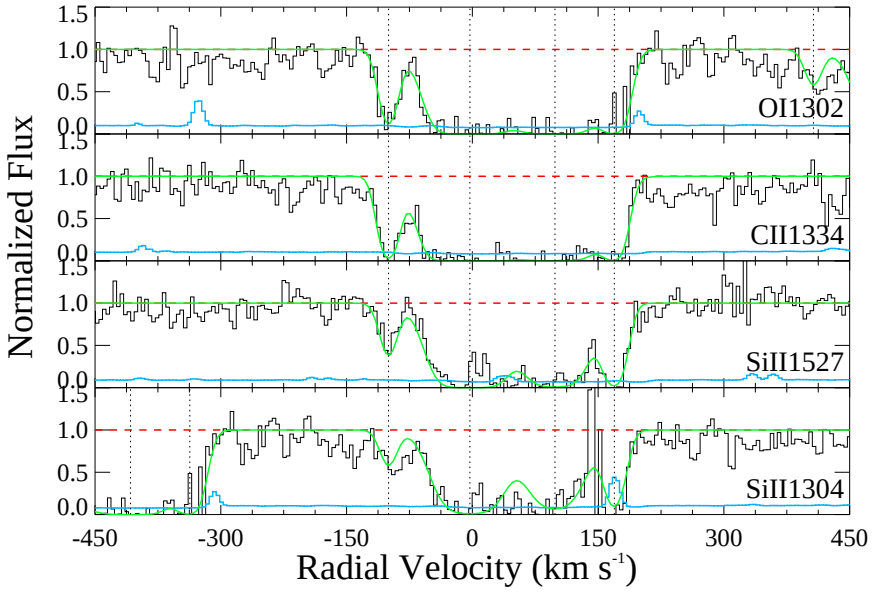

Figure 4.35 Same as Fig. 4.24 but for the absorber at $z = 4.627$ in the sight line to J1557+1018.

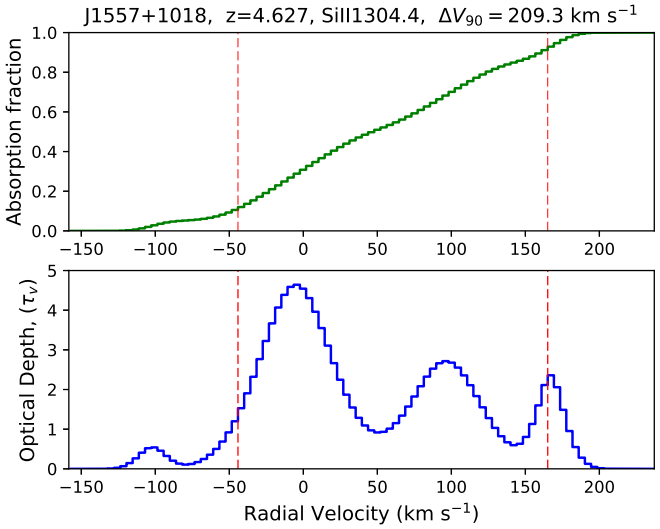

Figure 4.36 Same as Fig.4.3 but for Si II λ1304.4 line in $z = 4.627$ absorber toward J1557+1018 based on our Voigt profile fits.

Chapter 5

Discussions

Here, we combine the new measurements with those drawn from the literature and study the metallicity vs. velocity width relation, dust depletion, relative abundances and nucleosynthesis, and the metallicity evolution. We also compare our results at z$\sim$5 with the lower redshift absorbers.

5.1 Metallicity vs. Velocity Dispersion Relation

The gas kinematics of a galaxy can be understood from the measurement of velocity dispersion of its gas. One measure of the gas velocity dispersion is the quantity Δv_{90}, i.e., the velocity range that spans 90 percent of the total absorption determined from relatively weak and unsaturated metal lines (Wolfe et al. 1998). Chapter 4 lists the measurements of velocity dispersion for all the absorbers in this work. To estimate Δv_{90}, we measure the radial velocity width between 5 percent and 95 percent of the integrated optical depth using the fitted profiles as shown in Fig. 4.3. The value of the velocity dispersion may depend on the inflow or outflow of gases within the galaxy and also on the mass of the galaxy. If the velocity dispersion depends primarily on mass, and the role played by gas flows is small, then the velocity dispersion vs. metallicity relation can suggest a relationship between mass and metallicity (MZR) of absorber host galaxies. In lower redshift DLAs and sub-DLAs, a fairly tight correlation exists between the metallicity and the velocity dispersion of the gas (e.g. Péroux et al. 2003, Ledoux et al. 2006, Moller et al. 2013, Som et al. 2015, Quiret et al. 2016)(See Fig. 5.1). Quiret et al. (2016) derived an empirical relation between the velocity dispersion

vs. metallicity as $[X/H]_{DLA}$ = (1.52 ± 0.08) log V_{90} - (4.20 ± 0.16), suggesting a strong relationship between velocity dispersion and metallicity. However, this relation is still unknown for high-z absorbers. Fig. 5.1 shows the metallicity vs. velocity dispersion relation for all the absorbers presented in this work, and other sources from the literature. The velocity dispersion vs. metallicity relation is much flatter at $z > 4.5$ than for the $z < 4.5$ absorbers. Since we don't find the well established metallicity vs. velocity dispersion trend seen at lower redshifts, it is possible that the strength of the correlation decreases with increasing redshift.

As suggested by some simulations, the velocity width could be related to the gravitational potential well of the absorption system's host galaxy (e.g. Prochaska & Wolfe 1997b; Haehnelt, Steinmetz & Rauch 1998; Pontzen et al. 2008). Similarly, Ledoux et al. (2006) and Moller et al. (2013) interpreted the velocity width versus metallicity relation as an MZR by assuming a scaling of the galaxy luminosity with dark matter halo. Therefore, a much flatter metallicity vs. velocity dispersion relation at $z \sim 5$ compared to that at lower redshifts may suggest that the $z \sim 5$ absorbers are tracing the more massive galaxies that did not get as enriched chemically. This may suggest that they have a higher M/L ratio and thus a lower M_* and are dominated more by dark matter. We note, however, that the velocity dispersion could partly arise in gas flows within the circumgalactic medium, and thus may not necessarily be a measure of the mass of the galaxy; in this scenario, the $z \sim 5$ absorbers may trace galaxies with stronger inflows of less enriched material. Moreover, Bouché et al. (2012) show that the inclination of the galaxy has a direct impact on the absorption profile and therefore on the velocity width. Observations of more high-redshift absorbers are needed to establish whether these differences are unique to these particular absorbers or are a common phenomenon at these early epochs. In order to estimate the minimum sample size that is needed to test the possible evolution of the velocity dispersion vs. metallicity relation, we create an arbitrary number of

artificial data points that fall randomly within the observed ranges of values. Then we perform the Spearman rank-order correlation test to calculate correlation coefficient ρ_s and P(ρ_s) for the sample including these artificial data points, and find that $\sim$30 data points are needed to tell whether any correlation exists or not at the level of 3σ. Thus, observations of $\sim$19 more high-z absorbers are needed to complement the current sample of 11 absorbers to address this point more definitively.

5.2 Determination of Dust Depletion

Jenkins (2009) developed a technique for estimating the extent of dust depletion using observations of multiple elements. Based on observations of 17 chemical elements (C, N, O, Mg, Si, S, P, Cl, Ti, Cr, Mn, Fe, Ni, Cu, Zn, Ge, and Kr) along the sightlines to 243 stars in the Milky Way, he established that depletion of elements on dust grains can be well-characterized in terms of three parameters. One of these parameters, F_*, represents a generalized depletion strength for the particular sightline being analyzed. The scale of F_* is arbitrary, but it lies in the range of 0 to 1 for most sightlines in the Milky Way, although warm ionized gas in the Milky Way shows $F_* = -0.1$ (Draine 2011). The higher the value of F_*, the more severe is the depletion. The other two parameters A_x and B_x are unique constants for each element X and were derived empirically by Jenkins (2009). A_x is the propensity of the element X to have a higher depletion value as the line-of-sight depletion factor F_* increases. In terms of these parameters and a zero-point offset Z_x [added to make the measurement errors in A_x and B_x independent of each other, and also derived empirically by Jenkins (2009)], the gas-phase abundance of element X is described by the relation [X_{gas}/H] $= B_x + A_x(F_* - Z_x)$. Thus, the coefficients A_x and B_x denote the slope and the offset in the linear relationship of depletion vs. F_*. In an extension of this work, Jenkins & Wallerstein (2017) presented the values of A_x, B_x, and Z_x in the Small Magellanic Cloud (SMC) for 9 elements, and suggested that these values would be better suited

for studies of depletion patterns in the low-metallicity DLA and sub-DLA absorbers in the distant universe.

As further explained in Appendix A of Quiret et al. (2016), the observed abundance of element X relative to the solar level can be expressed as $[X/H]_{obs}$ - B_x + $A_x z_x = [X/H]_{intrinsic} + A_x F_*$. In other words, in a plot of the quantity $[X/H]_{obs}$ - B_x + $A_x Z_x$ vs. A_x, the slope is the line-of-sight depletion factor F_*, and the intercept is $[X/H]_{intrinsic}$, the intrinsic depletion-corrected metallicity derived from element X. In this work, we adopt the values of A_x, B_x and Z_x for O and C from Jenkins (2009) and for Si and Fe from Jenkins & Wallerstein (2017) to estimate the F_* value and the intrinsic metallicity for each absorber. Furthermore, we take the uncertainties in A_x and B_x into account, while estimating the uncertainties in F_* and $[X/H]_{intrinsic}$.

Fig. 5.2 to Fig. 5.8 show the plots of $[X/H]_{obs}$ - B_x + $A_x Z_x$ vs. A_x to calculate the intrinsic metallicities and F_* values for seven absorbers for which we have determinations of [O/H] and the associated uncertainties (not just lower limits). The F_* values that exhibit the extent of dust depletion are in the range of -0.27 ± 0.24 to -1.16 ± 0.28. These F_* values are much closer to the Milky Way's halo gas ($F_* = -0.28$) than to the Milky Way's cool disk gas, warm disk gas, or disk+halo gas ($F_* = 0.90, 0.12$, and -0.08, respectively). Overall, 5 of the 8 absorbers at $z > 4.5$ have F_* values equal to or greater than the typical value of -0.70 ± 0.06 found for lower-redshit DLAs by Quiret et al. (2016). Fig. 5.9 shows the comparison of $F^\star$ values from our systems with those of the MW halo, cool disk, warm disk, disk+halo, and the sample from Quiret et al. (2016). Thus, dust depletion appears to be significant in a substantial fraction of absorbers at $z > 4.5$. Finally, the dust-corrected (i.e., intrinsic) metallicities obtained for these absorbers from Jenkins' approach are consistent with the observed [O/H] values within the uncertainties.

Three absorbers show significantly subsolar [C/O] ratios. Two of our $z \sim 5$ absorbers show strong depletion of Fe relative to O. One absorber shows strong Si

depletion relative to O. Two other absorbers show mild Si depletion, with [Si/O] comparable to the typical value of -0.08 ± 0.10 for VMP DLAs (Cooke et al. 2011). Fig. 5.10(a) shows a plot of depletion of Si with respect to undepleted elements O or Zn or S vs. metallicity. A correlation between depletion and metallicity has been noted before for lower-redshift DLAs (Meiring et al. 2006, Meiring et al. 2009, Noterdaeme et al. 2008, Kulkarni et al. 2015). One of the $z \sim 5$ absorbers falls below this trend, while the others may be consistent with that trend. Fig. 5.10(b) shows a plot of depletion of Fe with respect to undepleted elements O or Zn or S vs. metallicity. Three of the $z \sim 5$ absorbers may be consistent with the correlation between depletion and metallicity for lower-redshift DLAs. Measurements of undepleted as well as depleted elements in a larger sample of high-z absorbers are needed to further clarify the nature of this trend at $z \gtrsim 5$. Again, we perform the Spearman rank-order correlation test to calculate the correlation coefficient ρ_s and $\mathrm{P}(\rho_s)$ for the existing sample including artificial data points that fall randomly within the observed ranges of values, and find that $\sim$50 total data points (i.e., $\sim$ 44 more data points beyond the existing 6 points) are needed to tell whether any correlation exists or not at the level of 3σ.

5.3 Relative Abundances and Nucleosynthesis

In principle, the initial mass function of the first stars in the universe can be inferred observationally from the chemical signatures of the elements that were made during the life cycle of a Population III star. Several recent studies have suggested that the abundance patterns of metal-poor stars in the Milky Way are successfully reproduced by models of Population III stellar nucleosynthesis (e.g., Heger & Woosley 2010; Cooke & Madau 2014; Tominaga, Iwamoto, & Nomoto 2014). Similar searches for chemical signatures of first stars have been undertaken in the most metal-poor DLAs (Erni et al. 2006; Pettini et al. 2008; Penprase et al. 2010; Cooke et al. 2011a,b;

Cooke, Pettini, & Murphy 2012). The most metal-poor DLAs are also considered to be the antecedents of the lowest mass galaxies (e.g., Cooke, Pettini, & Jorgenson 2015). Thus, metal-poor DLAs provide a promising environment to measure the chemical signatures of the earliest generation of stars at high-redshift.

Fig. 5.11 shows a plot of [C/O] vs. [O/H] for both the DLAs at z$\geqslant$4.5 and the metal-poor DLAs at lower redshifts from the literature. Although the $z > 4.5$ DLAs are not always metal-poor, their average [C/O] value of -0.19 ± 0.12 is consistent with that for the very metal-poor (VMP) DLAs, which have an average [C/O] of -0.28 ± 0.12 (e.g. Cooke et al. 2011, Cooke et al. 2017). By comparing the abundance pattern of the most metal-poor DLA to nucleosynthesis models, Cooke et al. (2017) found that the chemistry of the gas was consistent with the yields of a metal-free star that ended its life as a core-collapse supernova. However, Cooke et al. (2011) have suggested that metal-poor DLAs may have been enriched by metal-free progenitor stars, but they can not yet rule out an additional contribution from Population II stars. The similar [C/O] ratios between metal-poor DLAs and the $z \sim 5$ DLAs suggest that DLAs at $z \sim 5$ may also have been enriched by early stars, including perhaps a leftover signature of Population III stars and that the signatures of nucleosynthesis during those explosions are still seen in gas at $z \sim 5$ (i.e., the Population III stars formed and exploded well before z>5 and the gas was later enriched by their signatures at z$\sim$5). Thus, it seems reasonable to compare the chemistry of metal-poor DLAs with the $z \sim 5$ DLAs to constrain the nature of the progenitor stars, especially their Initial Mass Function (IMF).

To this end, we have selected three metal-poor $z \sim 5$ DLAs which have [O/H]$<$ -2.20 to compare with the nucleosynthesis models of massive metal-free stars from Heger & Woosley 2010. We compared [C/O] in these 3 DLAs with those predicted by Heger & Woosley (2010), because [C/O] is believed to put a strong constraint on the progenitor mass of Population III stars (e.g. Woosley & Weaver 1995, Heger

& Woosley 2010, Cooke et al. 2011, Cooke et al. 2017). The models of Heger & Woosley (2010) include 120 simulated stars spanning progenitor star masses in the range of 10-100 $M_{\odot}$, with a varying mass resolution of δM = 0.1 to 5.0 $M_{\odot}$. To consider the mixing between different stellar layers, these models use grids with 14 different mixing widths. Furthermore, the explosion energy of the supernova ranges from 0.3 to 10 $\times 10^{51}$ erg (i.e., 0.3B, 0.6B, 0.9B, 1.2B, 1.5B, 1.8B, 2.4B, 3.0B, 5.0B, and 10.0B, where 1B=10^{51} erg). Thus, this model comprises a total of 16800 (14 $\times$ 10 $\times$ 120) combinations of the three parameters: stellar mass, explosion energy, and mixing width. The position of the piston just before the explosion is just below the oxygen burning shell where the entropy per baryon is given by $S/k_B = 4$, where k_B is the Boltzmann constant. We compared the [C/O] and [Si/O] ratios predicted by these various models with the ratios observed for our DLAs of interest, in order to estimate the range of progenitor mass, explosion energy, and mixing width that may have enriched these DLAs. To accomplish this, we used the code developed by Cooke et al. (2017) that linearly interpolates this three-dimensional space (stellar mass, explosion energy, and mixing parameter) and ran a Markov Chain Monte Carlo analysis using the emcee software (Foreman-Mackey et al. 2013). We applied the Metropolis-Hastings algorithm comprising of 100 walkers and 500 burn-in steps. The one- and two-dimensional projections of the samples are plotted in Fig. 5.12, 5.13, and 5.14 for the DLAs towards J0231-0728, J0306+1853, and J0824+1302 respectively. We were able to put a strong constraint on the progenitor masses for all of these DLAs. The probability distributions of the progenitor masses were centered around 14.6, 12.2, and 17.1 $M_{\odot}$ for the $z = 5.335$, 4.987, and 4.809 DLAs towards J0231-0728, J0306+1853, and J0824+1302 respectively. The explosion energies were more or less constrained towards the upper end of the given range ($E_{exp} > 5 \times 10^{51}$ erg) for the DLAs towards J0306+1853 and J0824+1302 and 2-4 $\times 10^{51}$ erg for the DLA towards J0231-0728. However, the mixing parameters could not be constrained well for any

of our DLAs. The progenitor masses for two of our systems differ from that of Cooke et al. (2017) by $\sim$ 2 σ, who obtained a progenitor mass of 20.5 $M_{\odot}$ and explosion energy of 6-8 $\times 10^{51}$ erg for a VMP DLA at $z \approx 3.1$ with [O/H] of -3.05 (see Fig. 5.15).

The z>5 epoch may be more interesting as the metals observed in absorption at this epoch are only a few hundred million years old and the observations of more DLAs/sub-DLAs sample at z$\sim$5 and beyond with the help of future large facilities (e.g., GMT, JWST) will increase the opportunities for investigating extremely metal-poor absorbers in the high-redshift quasar sight lines, which can be compared with the models of Population III stellar nucleosynthesis.

5.4 Metallicity evolution

The cosmic mean metallicity of DLAs, also defined as the $N_{H\,I}$-weighted mean metallicity, $< Z >$ is the ratio of the mean comoving densities of metals and hydrogen, given by $< Z >$ = log (Ω_M/Ω_H) -log $(M/H)_{\odot}$ where, Ω_M is the comoving density of metals and Ω_H is the comoving density of neutral hydrogen (Lanzetta 1995, Kulkarni 2002). It is standard practice to use $< Z >$ to investigate the metallicity evolution of DLAs (e.g. Prochaska et al. 2003a, Kulkarni et al. 2005, Kulkarni et al. 2010, Rafelski et al. 2012, Rafelski et al. 2014, Som et al. 2015, Quiret et al. 2016, Poudel et al. 2018). In this section, we determine the cosmic mean metallicity of DLAs at redshift $z > 4.5$ and compare it with previous measurement at $z > 4.5$ as well as $z < 4.5$.

The metallicity of DLAs decreases by $\approx$0.2 dex per unit increase in redshift as we go from $z = 0$ to $z = 4.5$ (e.g. Prochaska et al. 2003a, Kulkarni et al. 2005, Kulkarni et al. 2007, Som et al. 2013, Rafelski et al. 2012, Jorgenson et al. 2013, Som et al. 2015, Quiret et al. 2016). At $z > 4.7$, a sudden decline of cosmic mean metallicity to a level of $< Z >$ = -2.03 (6σ below the prediction from lower-redshft

DLAs) has been claimed (e.g. Rafelski et al. 2012, Rafelski et al. 2014). However, this conclusion was based on $z > 4.7$ measurements of primarily Si and Fe, which are refractory elements. Several studies have noted that such refractory elements are more strongly depleted on interstellar dust grains compared to volatile elements such as S, O, and Zn in the Milky Way interstellar medium (ISM) (e.g. Savage & Sambach 1996, Jenkins 2009). Furthermore, a number of studies have noted the prevalence of dust depletion and the difference in depletions of refractory and volatile elements in DLAs (e.g. Pettini et al. 1997, Kulkarni 1997, Jenkins 2009, De Cia et al. 2016). Indeed, several recent studies have noted that dust depletion exists in some DLAs even at $z \sim 5$ (e.g. Morrison et al. 2016). Therefore, to make a robust comparison between the metallicities of the absorbers at $z > 4.5$ and $z < 4.5$, we use the elements O, S, and Zn, which have lower condensation temperatures and thus lower depletion levels. The metallicity of DLAs based on O, S, and Zn is shown in Fig. 5.16.

As seen in Fig. 5.16, for some of the absorbers in our sample, we could only place lower limits on the metallicity. We include both these limits as well as the definitive determinations while calculating the mean metallicity $< Z >$ using survival analysis. For this, we use the SURVIVAL package in IRAF which provides the maximum likelihood estimator of the censored data points (data that include only limits) and allows estimation of the mean value and the associated error for measurements consisting of a mixture of detections and limits (either upper limits or lower limits). Each bin at $z < 4.5$ included 16 or 17 DLAs and the high-redshift bin (spanning $4.589 < z < 5.335$, with a median redshift of 4.83) included 14 absorbers with measurements of either O or S. The $N_{H\,I}$-weighted mean metallicity $< Z >$ in the highest redshift bin (i.e. for $z > 4.5$) is -1.51 ± 0.18, and is shown in Fig. 5.16 as a red diamond. The binned $N_{H\,I}$-weighted mean metallicity of lower redshift systems is indicated as blue circles with blue error bars and the corresponding linear best fit is shown as a dashed blue line. The predicted metallicity from lower redshift data

is consistent with our value in the highest redshift bin. The difference between the predicted and observed values is $< 0.5\sigma$, even if the uncertainty in the predicted value is ignored.

A few of the absorbers in our $z > 4.5$ sample are sub-DLAs rather than DLAs. It is interesting to ask whether the inclusion of these sub-DLAs is the cause of our cosmic mean metallicity being higher, given that sub-DLAs are found to be more metal-rich than DLAs at $z < 3$ (e.g. Som et al. 2013, Som et al. 2015, Quiret et al. 2016). We therefore repeated our calculations of the cosmic mean metallicity at $z > 4.5$ for only the DLAs, and found very little difference. The $N_{H\,I}$-weighted mean metallicity at $z > 4.5$ after excluding the sub-DLAs is -1.50 ± 0.16. The negligible difference between the values obtained with and without the inclusion of sub-DLAs implies that either $< Z >$ at $z > 4.5$ is dominated by absorbers with higher H I column densities, or that there is much less difference between the metallicity evolution trends for DLAs and sub-DLAs at these high redshifts. To help discriminate between these possibilities, we calculate the $N_{H\,I}$-weighted mean metallicity for just the sub-DLAs at $z > 4.5$, and find to be -1.36±0.30. Thus, it appears that the difference between the mean metallicities for DLAs and sub-DLAs is much smaller at $z > 4.5$ than at $z < 3$ (sub-DLAs at $3 < z < 4.5$ are not well studied). This suggests that DLAs and sub-DLAs may have been associated with parts of the same continuum of gaseous halos during the second Gyr of cosmic history (i.e., sometime during $3 < z \lesssim 4.5$).

It thus appears that the cosmic mean metallicity at $4.6 < z < 5.3$ is consistent with the predictions based on the trend observed for DLAs at $z < 4.5$. This result differs from the conclusion of Rafelski et al. (2012), and Rafelski et al. (2014) that there is a sudden drop in metallicity at $z > 4.7$. The difference may arise from our use of only the volatile elements S and O which have a lower condensation temperature and level of depletion in the MW ISM. This point has also been made by Morrison et al. (2016), and De Cia et al. (2018). Our result confirms that the metallicity at

$z > 4.5$ shows a smooth decrease rather than a sudden decline. Indeed, a gradual decrease agrees better with expectations than a sudden decline, in the absence of any evidence of a sudden change in the cosmic star formation history at or shortly before $z \sim 5$.

Furthermore, we note that the $N_{H\,I}$-weighted mean metallicity agrees within $\sim 1\sigma$ with the results from the n512RT64 simulation by Finlator et al. (2018), which predicts a value of -1.72 dex for the DLAs at $z = 5$. This simulation models a spatially inhomogeneous extragalactic ultraviolet background with 24 frequency bins and resolves dark matter haloes down to 10^8 $M_\odot$ within $12h^{-1}$Mpc volumes. It then combines observations of the IGM, CGM, galaxies, and reionization into a single framework.

Moreover, the metallicities of some of the z$\sim$5 absorbers appear to be more consistent with the Maio & Tescari (2015) model, which does not include Population III stars. These observed metallicities of some of the $z \sim 5$ absorbers are substantially lower than those predicted by the Kulkarni et al. (2013) model which include Population III stars. But as pointed out by Kulkarni et al. (2014), the rate of metal enrichment depends on the delay in the chemical enrichment of the gas by supernovae. The difference between some of the z$\sim$5 DLAs and the Kulkarni et al. (2013) model could be a result of a longer delay in the supernova-driven enrichment than assumed in the model.

5.5 Sample selection

We emphasize that these absorbers used to estimate the metallicity evolution were selected from the $z > 4.5$ SDSS absorbers listed in Noterdaeme et al. (2012) after checking that their SDSS spectra showed at least 1 metal line (regardless of its strength) at the same redshift as the H I line. The metal lines detected in the SDSS spectra were basically the lines with the highest oscillator strengths for the the most

abundant elements, i.e., O I λ 1302 and C II λ 1334. A non-detection of any of these lines was conservatively taken as an indication of non-reality of the system, given that H I identifications based on SDSS data were unreliable in some cases (e.g. Crighton et al. 2015). We now assess the effect of the sample selection on the metallicity. To do this, we have determined the smallest metal column density that could be detected from the low-resolution and low-S/N SDSS data and the corresponding metal abundances for a typical $N_{H\,I}$ value for our absorbers. To this end, we have performed simulations of O I λ1302 and C II λ1334 lines and measured their equivalent widths after convolving with the SDSS instrumental resolution to find the smallest column density that could be detected in the noisy SDSS spectra typical of the objects that were excluded from our sample. The selected quasar, J0807+1328 (RA: 08:07:15, Dec: +13 28 05.2) has an emission redshift of z=4.876 and the SDSS i-band magnitude of m_i =19.39. The absorber redshift (z=4.687) was reported by Noterdaeme et al. (2012) based on its Lyman-alpha measurements. This quasar's spectrum reaches a S/N per pixel of $\sim$ 14 near the redshifted O I λ 1302 line and a S/N per pixel of $\sim$ 10 near the redshifted C II λ 1334 line. The S/N per pixel near O I λ 1302 and C II λ 1334 lines of our sample from the SDSS has an average value of $\sim$ 15. These simulations (see Fig. 5.17) show that the equivalent width of a hypothetical O I λ1302 line for log $N_{O\,I}$=14.30 would be 3 times the 1 σ measurement uncertainty estimated from the S/N in the SDSS spectrum, i.e., log $N_{O\,I}$=14.30 would have been detectable at a 3σ level. This limit of log $N_{O\,I}$ = 14.30 would correspond to a limiting metallicity of [O/H]=-3.14 dex and -2.79 dex, respectively, at the maximum and median H I column density values for our sample (log N_{HI} = 20.75 and 20.40, respectively). These limiting metallicity values are, respectively, $>$ 42 times ($>$ 9σ) and $>$ 19 times ($>$ 7σ) below the N_{HI}-weighted mean metallicity that we find for the systems that we do observe. Moreover, the limiting metallicity values of -3.14 and -2.79 dex are far below the N_{HI}-weighted mean of Rafelski et al. (2014; $-2.03^{+0.09}_{-0.11}$).

Furthermore, the limit of log N_{CII} = 14.10 which would be detected at 3 σ level, correspond to a limiting metallicity of [C/H]=-3.08 dex and -2.73 dex, respectively, at the maximum and median H I column density values for our sample. Thus, the high mean metallicity we find is not a sample selection effect. For the sake of comparison, we have added a plot (see Fig. 5.18) showing detection significance of O I λ 1302 and C II λ 1334 lines for various column densities.

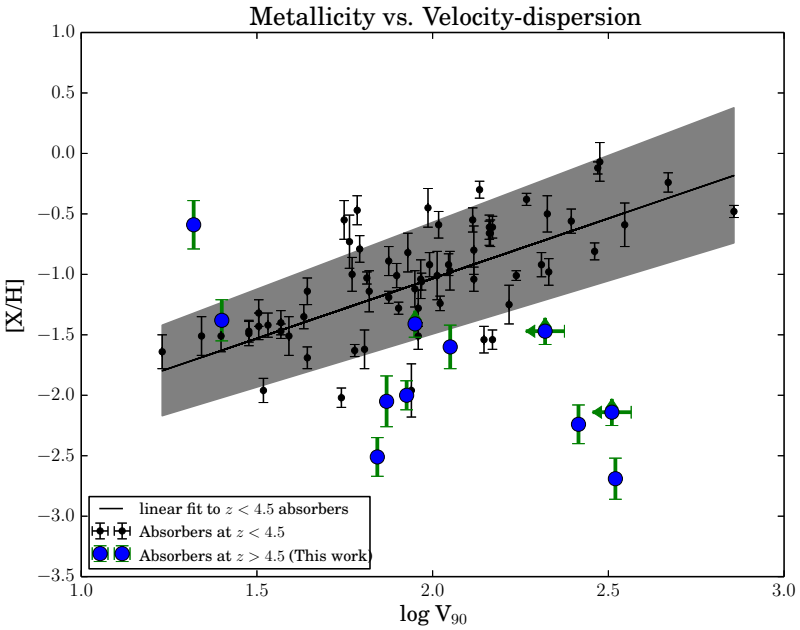

Figure 5.1 Plot showing metallicity vs. velocity-dispersion relation for volatile elements in DLAs, where X=O or S for $z \sim 5$ absorbers, and X=O, S or Zn for lower redshift DLAs. The black dots show the measurements for lower redshift DLAs from the literature. The blue dots with green error bars show the measurements for $z >$ 4.5 absorbers taken from this work. Lower and upper limits are represented by unidirectional arrows. The linear fit to the lower redshift absorbers is shown by the solid line in black and the shaded region shows the $\pm 1\sigma$ uncertainty in the fit.

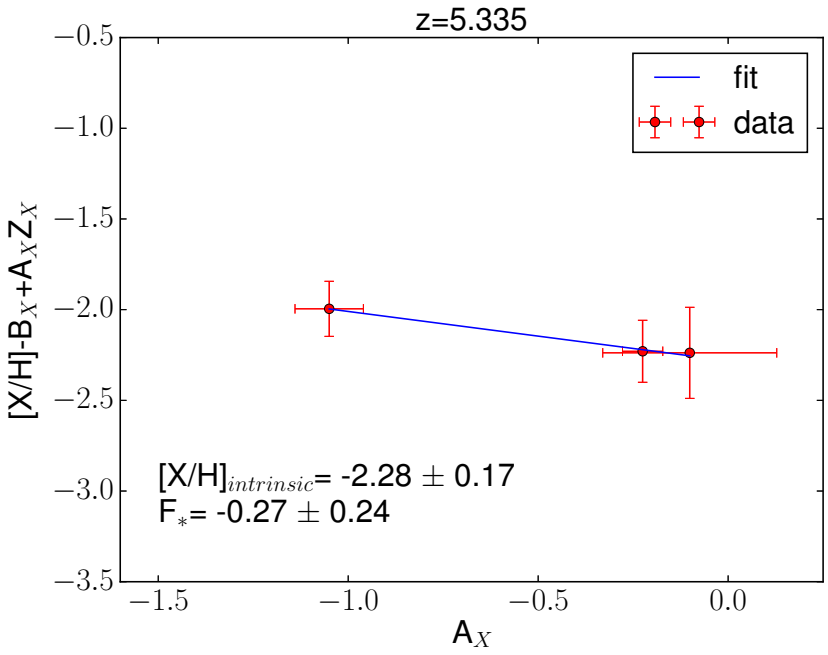

Figure 5.2 Plots showing $[X/H]_{obs}$ - B_x + A_xZ_x vs. A_x for the absorber at z=5.335. The F_* values and the depletion-corrected metallicity $[X/H]_{intrinsic}$ are shown in the bottom of the figure.

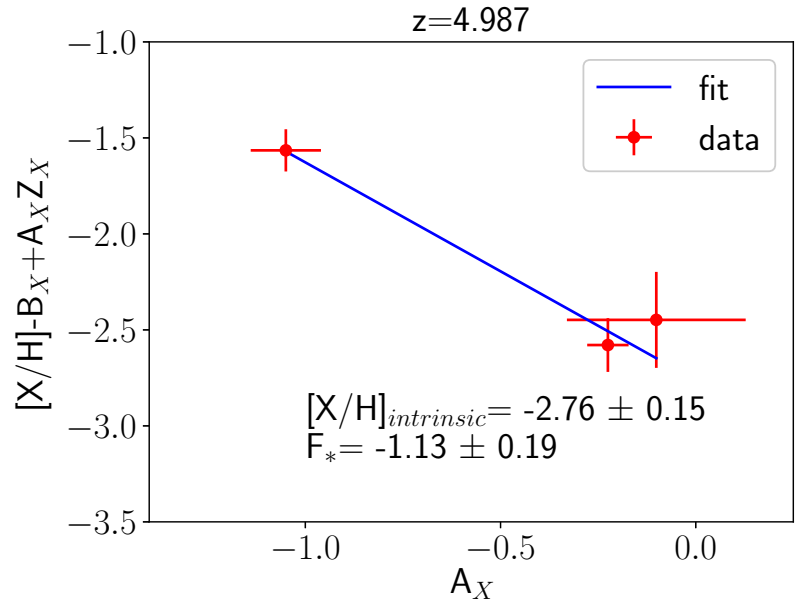

Figure 5.3 Same as Fig. 5.2 but for the absorber at z=4.987.

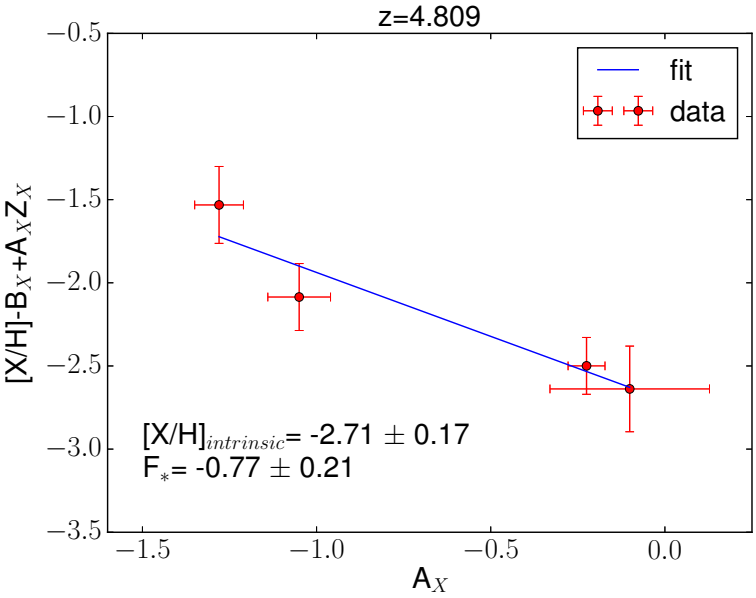

Figure 5.4 Same as Fig. 5.2 but for the absorber at z=4.809.

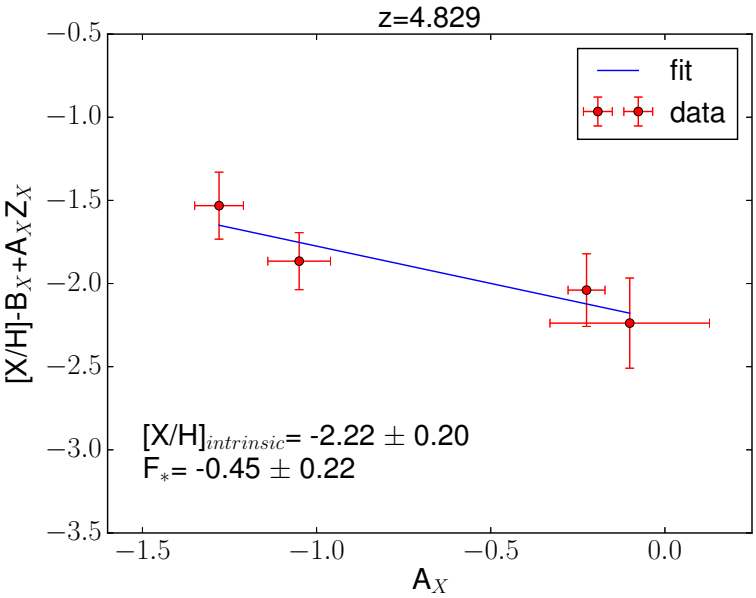

Figure 5.5 Same as Fig. 5.2 but for the absorber at z=4.829.

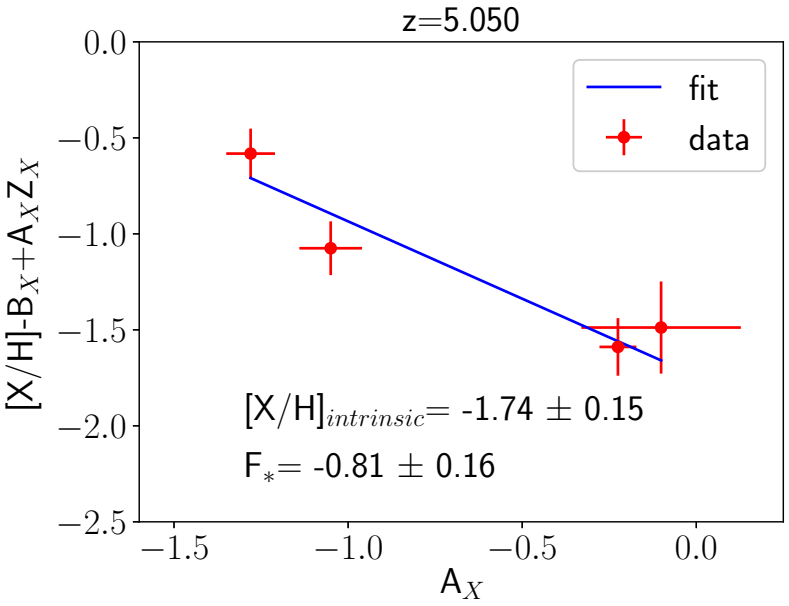

Figure 5.6 Same as Fig. 5.2 but for the absorber at z=5.050.

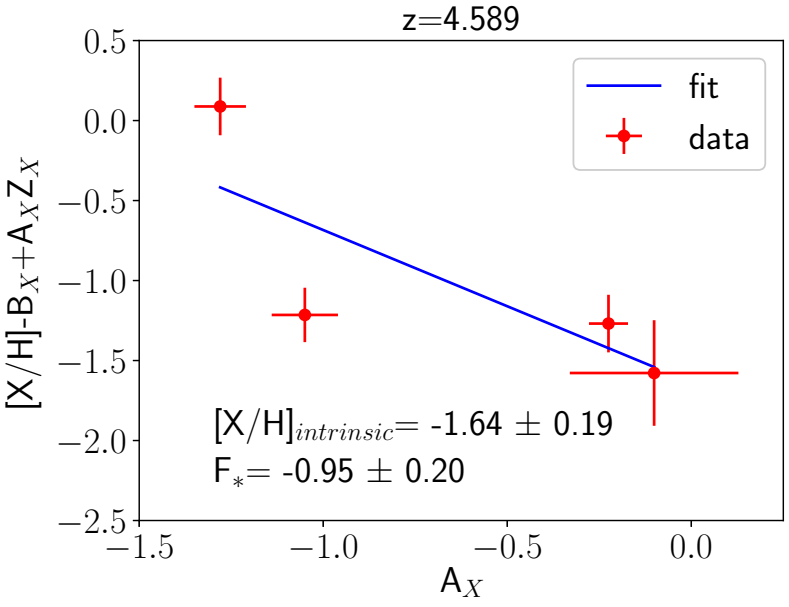

Figure 5.7 Same as Fig. 5.2 but for the absorber at z=4.589.

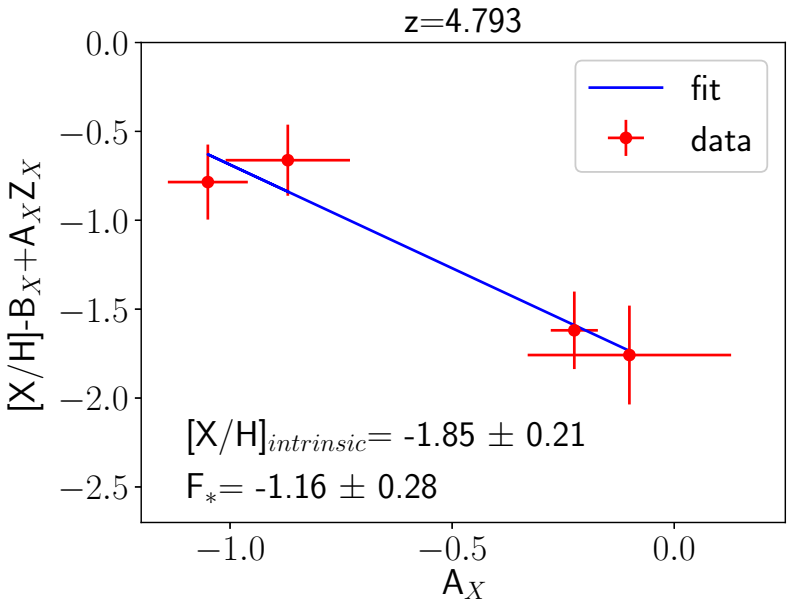

Figure 5.8 Same as Fig. 5.2 but for the absorber at z=4.793.

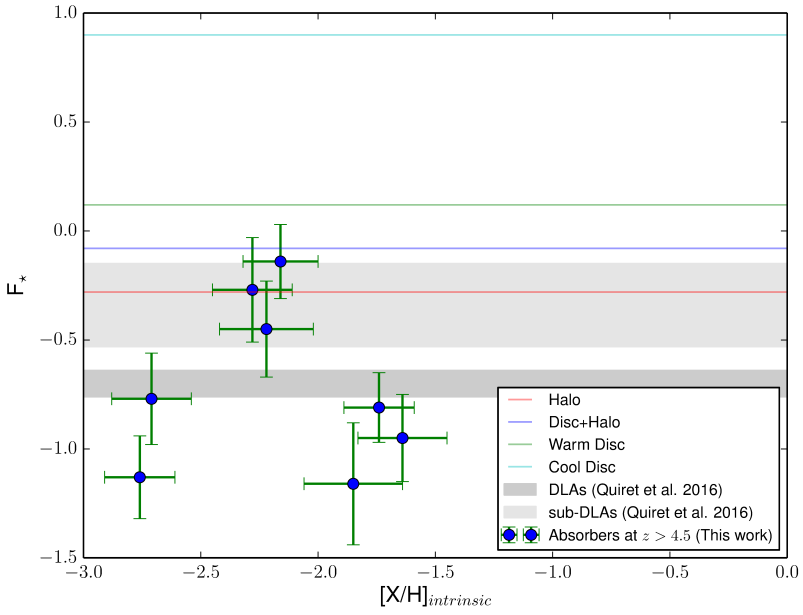

Figure 5.9 Plot showing the comparison of F⋆ values from our systems with average F⋆ values for those of the MW halo, cool disk, warm disk, disk+halo, and the sample from Quiret et al. (2016).

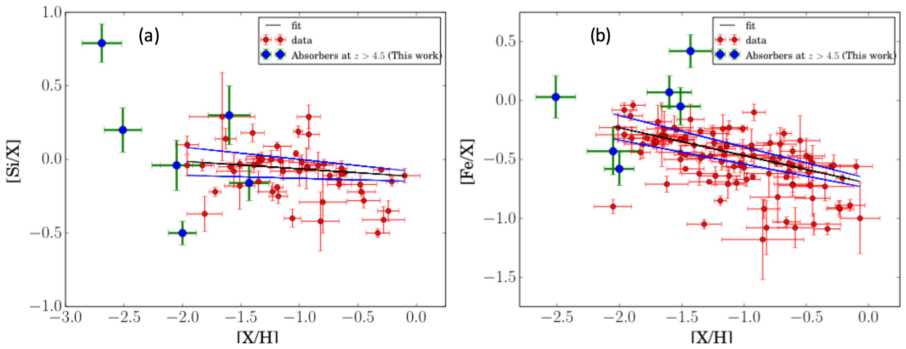

Figure 5.10 (a) Plot of [Si/X] vs. metallicity [X/H] for $z \sim 5$ absorbers (shown with blue dots) and lower-redshift DLAs from the literature (shown as red dots). (b) Plot of [Fe/X] vs. metallicity [X/H] for $z \sim 5$ absorbers (shown with blue dots) and lower-redshift DLAs from the literature (shown as red dots). In all panels, we use X=O for the $z \sim 5$ absorbers, and X=O, S, or Zn for the lower-redshift DLAs. In both cases, the lines of best fit for lower-redshift DLAs are shown by black solid lines and the $\pm 1\sigma$ uncertainty in the fits by two blue solid lines.

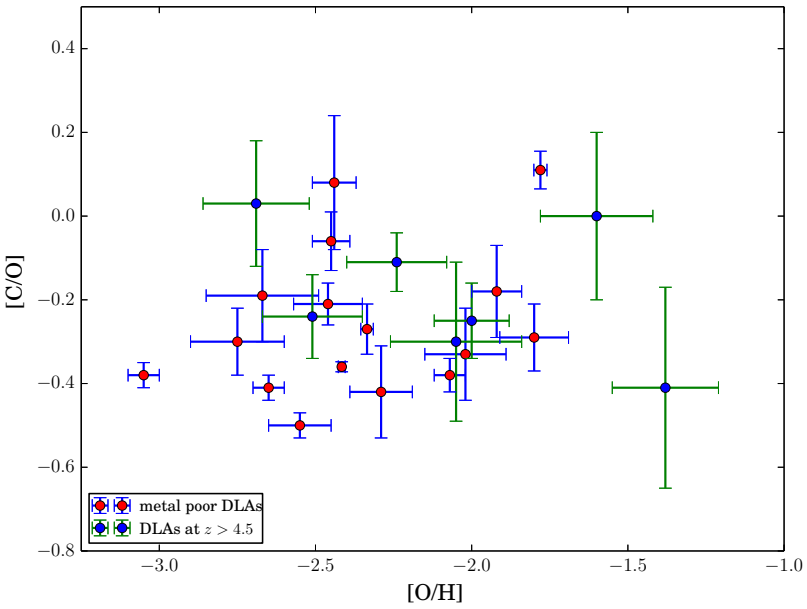

Figure 5.11 [C/O] vs. [O/H] for DLAs. The red dots with blue error bars show the measurements for metal-poor DLAs taken from Cooke et al. (2017). The blue dots with green error bars are the measurements for $z > 4.5$ absorbers which contain the measurements from Rafelski et al. (2012), Rafelski et al. (2014), Morrison et al. (2016), Poudel et al. (2018), and this work.

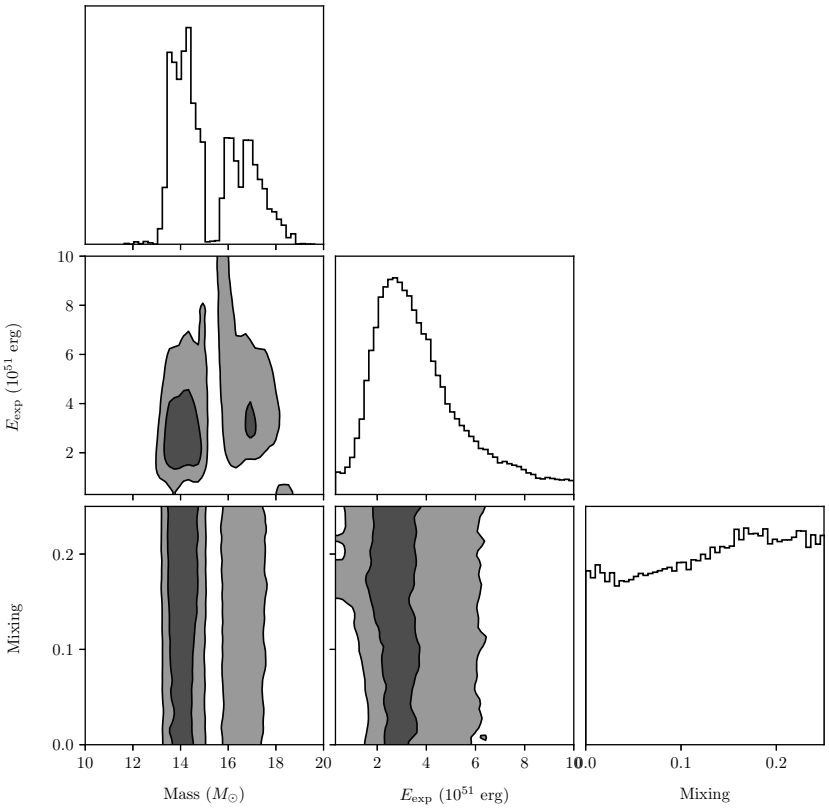

Figure 5.12 The one- and two-dimensional projections of the posterior probability distributions of progenitor mass, explosion energy, and the stellar mixing parameter of the star that might have enriched the DLA at $z = 5.335$ in the sight line to J0231-0728. We combined observed [C/O] and [Si/O] with the Heger & Woosley (2010) nucleosynthesis calculations, which comprised 16800 combinations of these three parameters. The marginalised probability of the model parameters on the x-axis are shown in the diagonal panel. The non-diagonal panels with dark and light shades are the two-dimensional projections of the parameters representing the 68 and 95 per cent confidence contours, respectively.

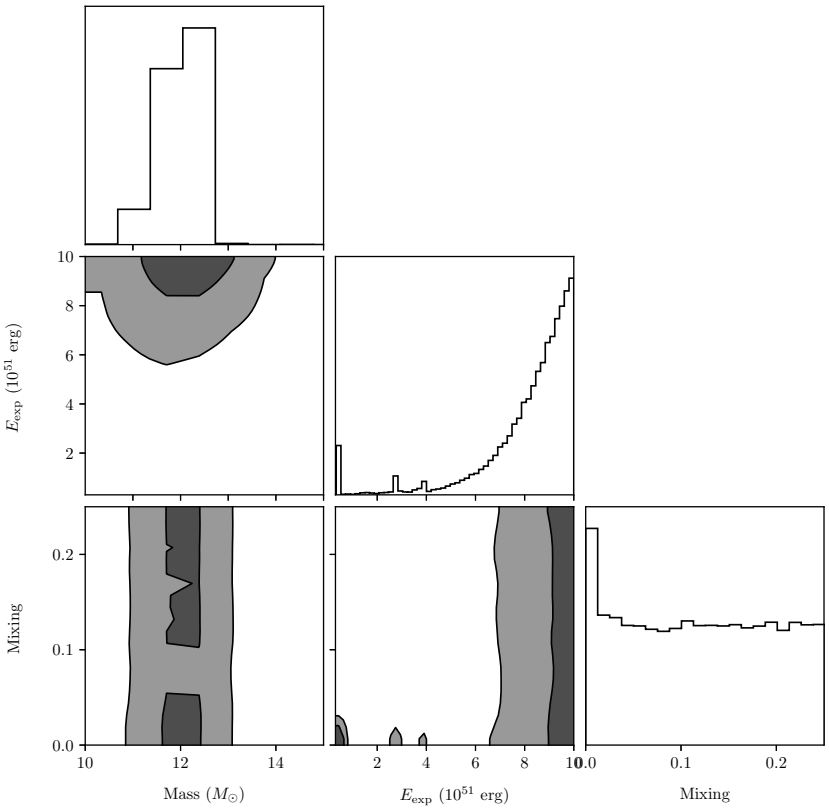

Figure 5.13 Same as Fig. 5.12 but for the DLA at z=4.987 in the sight line to J0306+1853.

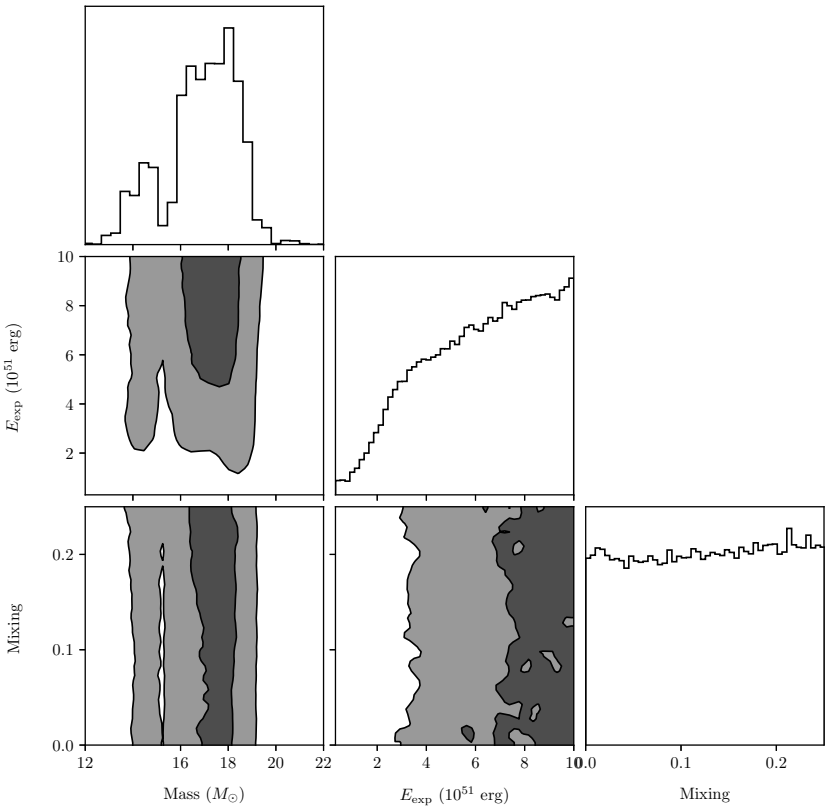

Figure 5.14 Same as Fig. 5.13 but for the DLA at z=4.809 in the sight line to J0824+1302.

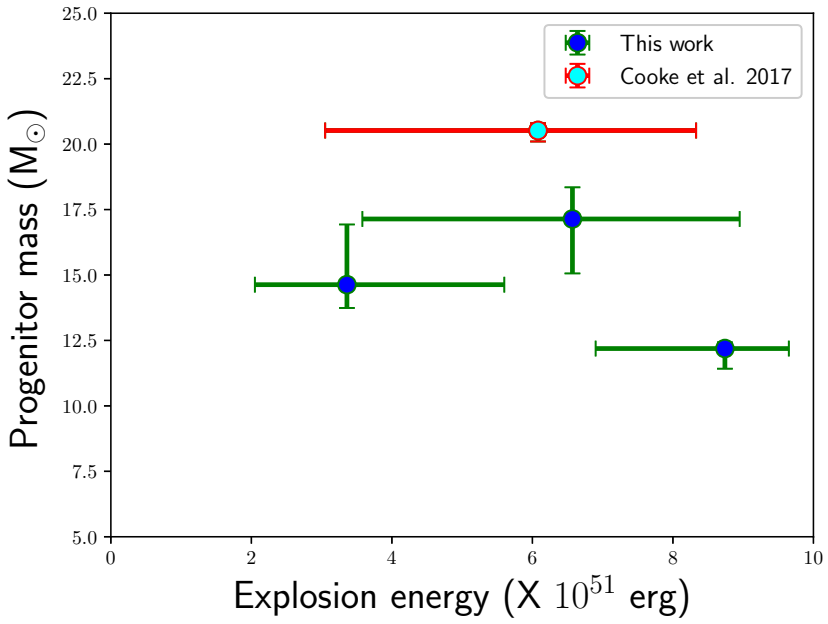

Figure 5.15 Plot of progenitor masses vs. explosion energies (in units of 10^{51} erg) for three systems from this work and one system from Cooke et al. (2017).

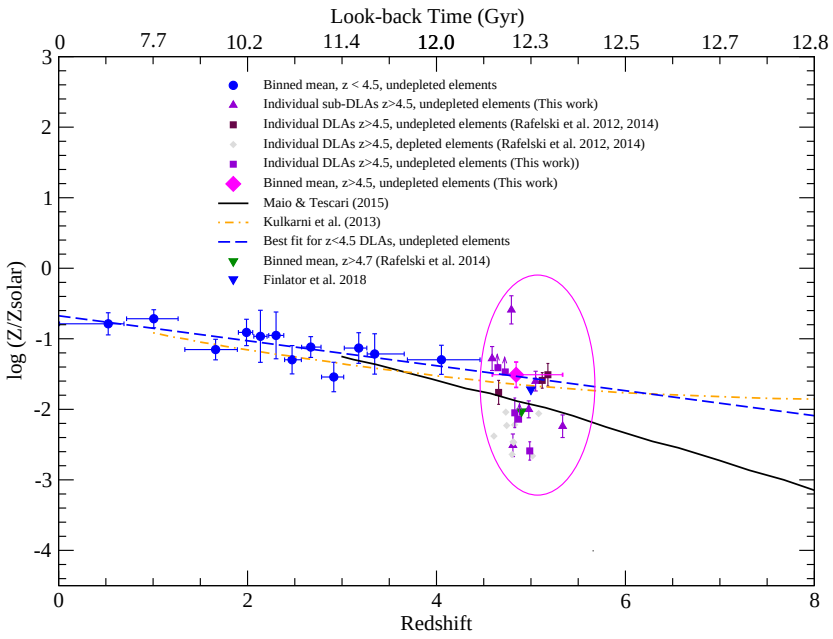

Figure 5.16 Metallicity evolution with redshift. The blue dots with blue error bars are the binned $N_{H\,I}$-weighted mean metallicities of DLAs at $z < 4.5$ using volatile elements from the literature, with each bin containing 16 or 17 DLAs and the dashed blue line showing the corresponding best fit. The upright triangles and squares inside the ellipse are the individual measurements for $z > 4.5$ absorbers also using volatile elements. Three of these measurements are taken from Rafelski et al. (2012), Rafelski et al. (2014), one from Morrison et al. (2016), and 10 from this work. The $N_{H\,I}$-weighted mean metallicity at a median redshift of $z = 4.83$ for all absorbers in the $z > 4.5$ bin is shown by a diamond in red. For comparison, the $N_{H\,I}$-weighted mean metallicity of DLAs at $z = 5$ for the n512RT64 simulation from Finlator et al. (2018) is shown by a triangle in blue. Solid curve shows the prediction for the mean gas metallicity from Maio & Tescari (2015). The dot-dashed curve in orange shows the prediction of the semi-analytic model of Kulkarni et al. (2013) including Population II and Population III stars.

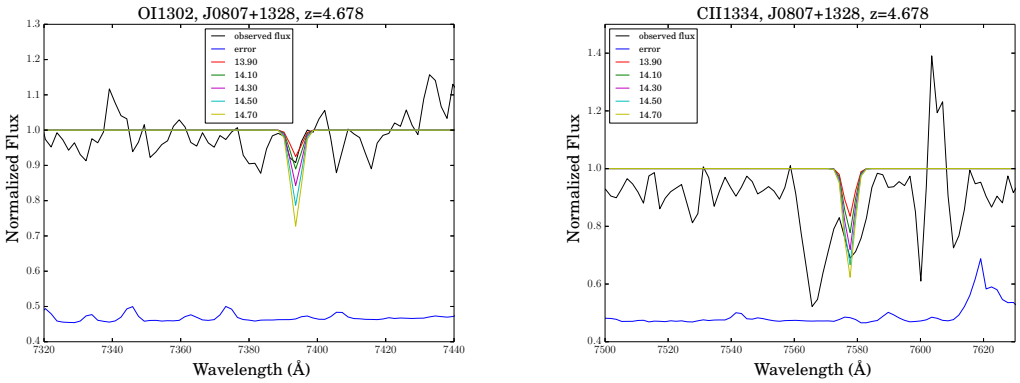

Figure 5.17 Overplotting of different column density (log N_{OI} and log N_{CII}) profiles convolved with SDSS resolution using typical SDSS spectra excluded from our sample to determine the SDSS metallicity floor. In each case, the observed continuum normalized flux is shown in black and the the 1σ error in the normalized flux is shown in blue at the bottom of each panel and is shifted by +0.4 for the purpose of displaying on the same scale. The metal line, sightline to the quasar, and redshift are given at the top of the figures in each panel.

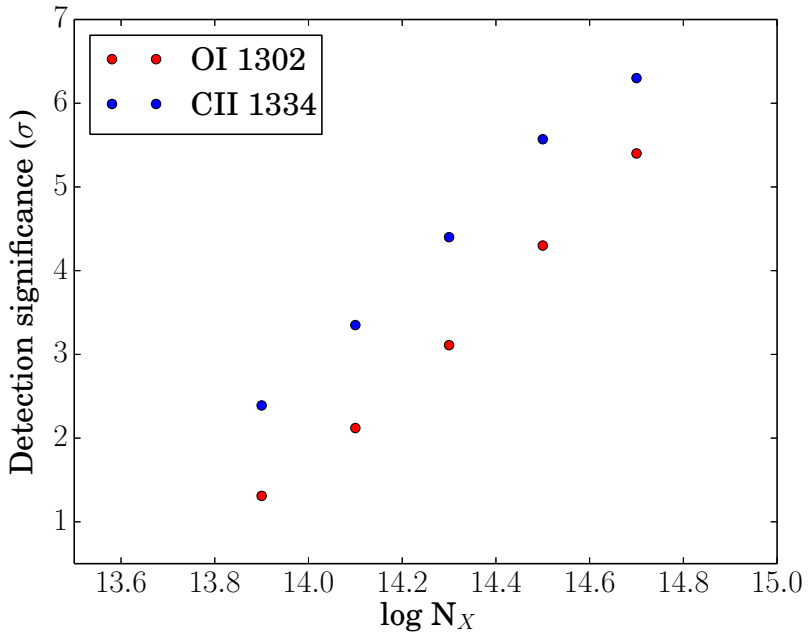

Figure 5.18 Plot showing detection significance for different column densities (log N_{OI} and log N_{CII}) for a hypothetical absorber at z=4.678 towards J0807+1328 using SDSS spectrum.

Chapter 6

Conclusions and future work

Here, we will summarize our conclusions and discuss the future works.

6.1 Conclusions

We have made ten new measurements of metal abundances at $z > 4.5$, increasing the existing sample for undepleted elements in gas-rich galaxies, and thus improving the constraints on the first ~ 1 billion years of cosmic metal evolution. Our main results are as follows.

1. We find a wide spread (factor of > 100) in the metallicities, which range from -2.69 dex to -0.59 dex. Our measurements include the highest metallicity observed in a sub-DLA at $z \sim 5$, with [S/H]=-0.59±0.20 for an absorber at $z = 4.793$ toward J1253+1046. In the same sight line, we also find a DLA at $z = 4.600$ with [O/H]>-1.46, which is the most metal-rich DLA known at $z \sim 5$.

2. Combining our sample with measurements from the literature, we examine the relative abundances in the $z \sim 5$ DLAs, and find their [C/O] ratios to be consistent with those of the VMP DLAs. Furthermore, we estimate the probability distributions of the progenitor masses to be centered around 12 $M_\odot$ to 17 $M_\odot$, using [C/O] and [Si/O] for three relatively metal-poor $z \sim 5$ DLAs.

3. In a substantial fraction of absorbers at $z > 4.5$, the extent of dust depletion, as judged by the parameter F_*, appears to be at least as significant as (and in some cases stronger than) the typical depletion found in lower-redshift absorbers.

4. The metallicity vs. velocity dispersion relation for $z \sim 5$ absorbers seems to

be different from that for lower redshift DLAs. The flatter trend observed for the $z \sim 5$ absorbers could be explained if these absorbers arise in galaxies with stronger inflows of chemically less enriched gas, or in more dark matter-dominated galaxies with smaller stellar masses.

5. We calculate the $N_{H\,I}$-weighted mean metallicity in the range $4.6 \gtrapprox z \gtrapprox 5.3$ and find it to be consistent with the prediction from lower redshifts DLAs, signifying a smooth decline in DLA metallicity rather than a sudden drop. Furthermore, we demonstrate that this high mean metallicity is not an artifact of sample selection.

6. The difference between the mean metallicities for DLAs and sub-DLAs at $z > 4.5$ is small, suggesting that DLAs and sub-DLAs may have been similar at this early epoch. The difference between the DLAs and sub-DLAs seen at $z < 3$ may have thus arisen sometime during $3 < z < 4.5$.

6.2 Future work

Our results demonstrate the value of obtaining high spectral resolution measurements of volatile elements such as O in absorbers at $z \sim 5$. Clearly, observations of more DLAs and sub-DLAs at $z \sim 5$ are essential to understand how robust the trends seen in the small existing samples are, and thus place more constraints on chemical enrichment of the gas in and around galaxies by early stars.

Although metallicity data for DLAs exist over $0<z\lesssim5$, there are only a handful of sub-DLAs that have been explored beyond z>3. Therefore, it is necessary to expand the redshift baseline for sub-DLA data much beyond z∼3 to examine the difference in metallicity between DLAs and sub-DLAs at z>3 and therefore to understand their connections to galaxies at different epochs of cosmic evolution.

One of the main priorities for our continuing study of quasar absorption line systems is to expand the redshift baseline for DLAs data much beyond z∼5. However, DLAs observations much beyond z∼5 is difficult, partly due to the inadequacy of

observations of high redshift quasars and partly due to the difficulty in estimating the hydrogen column density. As the forest lines increase significantly with redshift, the damping wings of hydrogen Lyman-alpha lines get blended severely, making the Voigt profile fitting extremely difficult. Therefore, it is necessary to develop alternative methods to identify the DLAs at those high redshifts. One of the ideas may be comparing the magnesium absorption systems with DLAs to find a connection between the magnesium column density and hydrogen column density.

With the future large telescopes like the Thirty Meter Telescope (TMT), the European Extremely Large Telescope (EELT), the Giant Magellan Telescope (GMT), and the James Webb Space Telescope (JWST), the observational capability will reach unprecedented levels and it will be possible to observe quasar absorption line systems at z>5 and towards fainter quasars. Detecting host galaxies in emission provide important clues to reveal the galaxy-absorber relationship. Of course, the detection of host galaxies in emission is easier at lower redshifts as the galaxies are relatively brighter. While the follow-up imaging and Integral Field Spectroscopy of gas-rich galaxies have been done to some extent in recent years (e.g., Péroux et al. 2011, 2014, 2019), it is difficult for the faint galaxies at higher redshifts. Such studies can be extended to higher redshifts with the help of these future facilities. Moreover, computing power is likely to improve simultaneously enabling more sophisticated cosmological simulations on smaller space-time scales. Similarly, future large astronomical surveys will provide unprecedented number of quasars sight lines at high redshifts which can be analyzed using machine-learning techniques to identify the absorbers (especially those at $z > 5$) and measure their properties. All of these aspects will help to solve various open issues, to yield a robust understanding of the epoch of reionization, galaxy-absorber relationship at higher redshifts, and the missing baryon problem.

More specifically, the unprecedented sensitivity in the near/mid-IR and high angular resolution of the JWST will help to detect nebular emission lines suitable for pro-

viding metallicity diagnostics in high-redshift galaxies. Near/mid-IR spectrographs on the JWST will also help to trace the metallicity evolution back to the first generation of stars (Population III stars) formed out of pristine gas. Moreover, the observations of a larger sample of DLAs/sub-DLAs at z$\sim$5 and beyond will increase the opportunities for investigating extremely metal-poor absorbers, whose abundance patterns can be compared with models of Population III stellar nucleosynthesis. Finally, the huge light-collecting areas of the TMT, GMT, and EELT will make it possible to obtain very high signal-to-noise spectra of high-redshift quasars, enabling major advances in the characterization of metallicities and relative abundances.

Bibliography

Abel T., Bryan G. L., Norman M. L., 2002, Sci, 295, 93

Asplund M., Grevesse N., Sauval A. J. et al. 2009, ARA&A, 47, 481

Aguirre A. et al. 2008, ApJ, 689, 851

Bahcall J. N., Salpeter E. E. 1965, ApJ, 142, 1677

Becker G. D., Bolton J. S., Lidz A. 2015, PASA, 32, 45

Beers T. C., Christlieb N. 2005, ARA&A, 43, 531

Berg T. A. M. et al. 2019, MNRAS, 488, 3

Bouché N., Hohensee W., Vargas R. et al. 2012, MNRAS, 426, 801

Bromm V., Coppi P. S., Larson R. B., 1999, ApJ, 527, L5

Casey C. M., Narayanan D., Cooray A. 2014, PhR, 541, 45

Cashman F. H., Kulkarni V. P., Kisielius R. et al. 2017, APJ, 230, 8

Cen R. 2012, ApJ, 748, 121

Clark P. C., Glover S. C. O., Klessen R. S., Bromm V. 2011, ApJ, 727, 110

Cooke R. J., Madau P., 2014, ApJ, 791, 116

Cooke R. J., Pettini M., Jorgenson R. A., 2015, ApJ, 800, 12

Cooke R., Pettini M., Murphy M. T., 2012, MNRAS, 425, 347

Cooke R., Pettini M., Steidel C. C. et al. 2011, MNRAS, 417, 1534

Cooke R., Pettini M., Steidel C. C. 2017, MNRAS, 467, 802

Crighton N. H. M. et al. 2015, MNRAS, 452, 217

Davé R., Oppenheimer B. D., Finlator K. 2011, MNRAS, 415, 11

De Cia A., Ledoux C., Mattsson L., Petitjean P. et al. 2016 A&A, 596, 46

De Cia, 2018, A&A, 613L, 2

Dessauges-Zavadsky M., Peroux C., Kim T. S. et al. 2003, MNRAS, 345, 447

Draine B. T. 2011, EAS, 46, 29

Erb D. K., Shapely A. E., Pettini M. et al. 2006, ApJ, 644, 813

Erni, P., Richter, P., Ledoux, C., & Petitjean, P. 2006, A&A, 451, 19

Finlator K., Keating L., Oppenheimer B. D. et al. 2018, MNRAS, 480, 2628

Foreman-Mackey D., Hogg D. W., Lang D. et al. 2013, PASP, 125, 306

Frebel A., Norris J. E. 2015, 2015, ARA&A, 53, 631

Fumagalli M., Prochaska J. X., Kasen D. et al. 2011, MNRAS, 418, 1796

Gonzalez V. et al. 2011, ApJ, 735L, 34

Gunn J. E., Peterson B. A. 1965, ApJ, 142, 1633

Haehnelt M. G., Steinmetz M., Rauch M., 1998, ApJ, 495, 647

Heger A. & Woosley S. E. 2010, ApJ, 724, 341

Henry A. et al. 2013, ApJ, 776, L27

Hirano S., Hosokawa T., Yoshida N., Umeda H. et al. 2014, ApJ, 781, 60

Jenkins E. B. & Wallerstein G. 2017, ApJ, 838, 19

Jenkins E. B. 2009, ApJ, 700, 1299

Jorgenson R. A., Murphy M. T., Thompson R. 2013, MNRAS, 435, 482

Keller S. C., et al., 2014, Natur, 506, 463

Kulkarni G., Rollinde E., Hennawi, Joseph F. et al. 2013, ApJ, 772, 93

Kulkarni G., Hennawi J. F., Rollinde E., Vangioni E. 2014, ApJ, 787, 64

Kulkarni V. P. & Fall S. M. 2002, ApJ, 580, 732

Kulkarni V. P., Fall S. M., Lauroesch J. T. et al. 2005, ApJ, 618, 68

Kulkarni V. P., Khare P., Péroux C. et al. 2007, ApJ, 661, 88

Kulkarni V. P., Khare P., Som D., Meiring J. et al. 2010, NewA, 15, 735

Kulkarni V. P., Som D., Morrison S., Péroux C. et al. 2015, APJ, 815, 24

Lanzetta K. M., Wolfe A. M., Turnshek D. A. 1995, ApJ, 440, 435

Ledoux C., Petitjean P., Moller P., Fynbo J. et al. 2006, A&A, 457, 71

Lehner N., 2013, ApJ, 770, 138

Storrie-Lombardi, L. J., Wolfe A. M. 2000, ApJ, 543, 552

Madau P. & Dickinson M. 2014, ARA&A, 52, 415

Maio U. & Tescari E. 2015, MNRAS, 453, 3798

Meiring J. D., Kulkarni V. P., Khare P., et al. 2006, MNRAS, 370, 43

Meiring J. D., Lauroesch J. T. et al. 2007, MNRAS, 376, 557

Meiring J. D., Lauroesch J. T. et al. 2009, MNRAS, 397, 2037

Moller P., Fynbo J. P. U., Ledoux C. et al. 2013, MNRAS, 430, 2680

Momjian E., Carilli C. L., Walter F., Venemans B. 2014, AJ, 147, 6

Morrison S., Kulkarni V. P., Som D. et al. 2016, ApJ, 830,13

Morton D. C., 2004, ApJS, 151, 403

Nagamine, K., Springel, V., Hernquist, L. 2004, MNRAS, 348, 421

Nagamine, K.; Springel, V.; Hernquist, L. 2004, MNRAS, 348, 385

Nakamura F. & Umemura M., 2001, ApJ, 548, 19

Neeleman M., Wolfe A. M., Prochaska J. X. et al. 2013, APJ, 769, 54

Noterdaeme P., Ledoux C., Petitjean P., Srianand R. 2008, A&A, 481, 327

Noterdaeme P. et al. 2012, A&A, 547, L1

Pei Y. C., Fall S. M., Hauser M. G., 1999, ApJ, 522, 604

Penprase B. E., Prochaska J. X., Sargent L. W. et al. 2010, ApJ, 721, 1

Petitjean P., Webb J.K., Rauch M. et al. 1993, MNRAS, 262, 499

Pettini M., Zych B. J., Steidel C. C. et al. 2008, MNRAS, 385, 2011

Pettini M., King D. L., Smith L. J., Hunstead R. W. 1997, ApJ, 478, 536

Péroux C. et al. 2019, MNRAS, 485, 1595

Péroux C., Kulkarni V. P., & York D. G. 2014, MNRAS, 437, 3144

Péroux C., Bouché N., Kulkarni V. P. et al. 2011, MNRAS, 410, 2237

Péroux C., Dessauges-Zavadsky M. et al. 2003, MNRAS, 345, 480

Pontzen A. et al., 2008, MNRAS, 390, 1349

Popping G., Somerville R. S., Trager, S. C. 2014, MNRAS, 442, 2398

Poudel S., Kulkarni V. P., Morrison S. et al. 2018, MNRAS, 473, 3559

Poudel S., Kulkarni V. P., Cashman F. H. et al. 2019, MNRAS, 491, 1008

Prochaska J. X., Gawiser E., Wolfe A. M. et al. 2003a, ApJ, 595, L9

Prochaska J. X., Gawiser E., Wolfe A. M et al. 2003b, ApJ, 147, 227

Quiret S. et al. 2016, MNRAS, 458, 4074

Rafelski M., Wolfe A. M., Prochaska J. X. et al. 2012, ApJ, 755, 89

Rafelski M., Neeleman M., Fumagalli M. et al. 2014, ApJ, 782, L29

Rahmani H. et al. 2016, MNRAS, 463, 980

Savage B. D., & Sembach K. R. 1996, ARAA, 34, 279

Savage B. D., & Sembach K. R. 1991, ApJ, 379, 245

Savaglio S., Glazebrook K., le Borgne D., et al. 2005, ApJ, 635, 260

Schmidt M. 1965, ApJ, 141, 129

Shapley A. E., Steidel C. C., Adelberger K. L. et al. 2004, ASSL, 301, 35

Som D., Kulkarni V. P., Meiring J. et al. 2013, MNRAS, 435, 1469

Som D. et al. 2015, ApJ, 806, 25

Somerville R. S., Primack J. R., Faber S. M. 2001, MNRAS, 320, 504

Stacy A. & Bromm V., 2013, MNRAS, 433, 1094

Stacy A., Bromm V., Lee A. T., 2016, MNRAS, 462, 1307

Tominaga N., Iwamoto N., Nomoto K., 2014, ApJ, 785, 98

Tremonti C. A. et al. 2004, ApJ, 613, 898

Troncoso P. et al. 2014, *A&A*, 563, 58

Walter F., Decarli R., Carilli C., et al. 2012, Nature, 486, 233

Wang F. et al. 2015, ApJ, 807L, 9

Wolfe A. M., Gawiser E., Prochaska J. X., 2005, ARA&A, 43, 861

Wolfe A. M., Chen H. 2006, ApJ, 652, 981

Wolfe A. M., Prochaska J. X., 1998, ApJ, 494, 15

Wolfe A. M. 1986, RSPTA, 320, 503

Woosley S. E. & Weaver T. A. 1995, ApJS, 101, 181

York D.G., Adelman J., Anderson J. E., et al. 2000, AJ, 120, 1579

Zafar T., Péroux C., Popping A., Milliard B. et al. 2013, A&A, 556, 141